Microfluidic disturbances on synthetic patterned surfaces and their impact on microorganisms in relation to biofouling control

A thesis submitted in fulfilment of the requirements for the degree of Doctor of Philosophy

by

Partha Halder

School of Civil, Environmental and Chemical Engineering
RMIT University
August 2014

Declaration

I certify that, except where due acknowledgement has been made, the work is that of the author alone; the work has not been submitted previously, in whole or in part, to qualify for another academic award. The content of the thesis is the result of work which has been carried out since the official commencement date of the approved research program at the School of Civil, Environmental and Chemical Engineering, RMIT University, Melbourne, Australia.

Partha Halder

Acknowledgement

Foremost, I would like to express my sincere gratitude to my advisor Dr Muhammed Ali Bhuiyan for the continuous support of my PhD study and research, for his patience, motivation, enthusiasm, and knowledge. His guidance helped me in all the time of research and writing of this thesis.

I also would like to thank my co-supervisors Dr Niranjali Jayasuriya, Professor Arnan Mitchell and consultants Professor Satinath Bhattacharya, Professor Margaret Deighton and Dr Jeff Shimeta for offering me the opportunity to work on an exciting project, and for being a great source of knowledge, inspiration and motivation during this research. I thank Dr Francisco Javier Tovar Lopez and Dr Mahyar Nasabi for their encouragement, motivation, insightful comments and paving the way on doing microfluidics at RMIT.

I wish also to express my heartiest gratitude to all my friends and relatives who have been patient and understanding and who despite distance have always been there.

Finally I would like to dedicate this thesis to Susmita for her unconditional love and patience during this challenging step in our lives in Australia.

Abstract

Biofouling, the unwanted growth of sessile microorganisms on submerged surfaces, presents a serious problem for underwater structures, water vessels and medical devices. It is a hierarchical process triggered by organic conditioning of underwater surfaces. Subsequently the attachment and growth of sessile microorganisms leads to biofouling. Biofouling is ubiquitous in nature and readily develops on any unprotected surfaces in both the marine and physiological environments. Conventionally the underwater structures (eg seawater intake heads, piping support structures, loading platforms and approach jetties) and water vessels (eg ship hulls, pleasure boats and yachts) are being protected against biofouling by metal based antifouling paints. The use of antifouling paints, in particular those containing Copper and Tributyltin (TBT), have been extremely successful for the hulls of ships by killing the majority of fouling species. Similarly, antibacterial medical coatings containing silver or antibiotics are being used frequently. These coatings have many detrimental effects including the mutation of bacteria which enables antibiotic-resistant biofilm development, failure of medical devices such as hip and knee implants, cause of catheter-associated urinary tract infection (CAUTI) and other hospital-acquired infections. The use of biocide-based metallic paints in the ocean and the silver-based antibacterial medical coating are posing more ecological and toxicity concerns and thus led to a mounting interest in developing non-toxic and no-kill alternatives for these systems.

One of the non-toxic approaches to control biofouling is to modify the settlement surface. This usually entails altering the surface topography and roughness, and developing a surface with a microstructured pattern. Studies showed that patterned surfaces inhibit the initial settlement of microorganisms and prolong the subsequent biofilm formation process. It is hypothesized that patterned surfaces can function simply as a physical deterrent against the settlement of fouling organisms and/or can develop effective microfluidic environment to inhibit the initial bacterial settlement process. Though it is well documented that biofouling can be controlled to various degrees with different microstructure-based patterned surfaces, the understanding of the underlying mechanism is still imprecise. The present study considered that microtopographies might influence near-surface microfluidic conditions, thus microhydrodynamically preventing the settlement of microorganisms. It is therefore aimed to characterize the microfluidic environment developed on patterned surfaces and its relation with the antifouling behaviour of those surfaces. In this study, patterned surfaces with microwell arrays were assessed experimentally with a real-time biofilm development monitoring system using a novel microchannel-based flow cell reactor. The dynamic interaction of a motile bacterium (*Escherichia coli*) with microtopographies was investigated by observing and assessing the trajectories of individual cells across an array of microwells using a time-lapse imaging module and image processing software. The effects of the solid boundaries on the dynamic stability of *E. coli* cells were assessed numerically using computational fluid dynamics (CFD) simulations. From this study, it is evident that patterned surfaces develop fluctuating stress-strain rates around microorganisms, alter their swimming depths, make them dynamically unstable and thus exhibit antifouling characteristics in a submerged condition. It is also stated that microstructures, capable of developing high wall shear bounded zones, keeping microorganisms away from the base surface, and giving no shelter against fluctuating microfluidic forces, could be considered effective in biofouling control. Finally, this study suggested a few optimized design patterns of microstructure-based antifouling surfaces, to develop effective microfluidic conditions capable of inhibiting the initial settlement of microorganisms.

List of Publications

Journal papers

Halder P, Nasabi M, Lopez FJT, Jayasuriya N, Bhattacharya S, Deighton M, Mitchell A, and Bhuiyan MA. 2013. A novel approach to determine the efficacy of patterned surfaces for biofouling control in relation to its microfluidic environment. Biofouling. 29: 697-713.

Halder, P. Nasabi, M. Jayasuriya, N. Shimeta, J. Deighton, M. Bhattacharya, S. Mitchell, A. and Bhuiyan, MA. 2014. An assessment of dynamic stability of microorganisms on patterned surfaces in relation to biofouling control. Biofouling. 30: 695-707.

Conference proceedings

Halder, P. Bhuiyan, MA. and Jayasuriya, N. 2012, 'Biofouling control: A microfluidic assessment of patterned surfaces', in Proceedings of the 2nd International Conference on Sustainable Built Environment (ICSBE 2012), Dissanayake R, Jayasinghe MTR, Mendis PA, Fernando S, Ruwanpura JY(ed.), University of Peradeniya, Sri Lanka, pp. 180-190 (ICSBE 2012).

Halder, P. Bhuiyan, MA. and Jayasuriya, N. 2012, ‘A microfluidic assessment of seawater intake system in the context of marine life protection’, in Proceedings of the International Conference on Life Science and Biological Engineering (LSBE 2013), Osaka, Japan, pp. 708-713.

Contents

List of Figures

List of Tables

Chapter 1

1 Introduction

1.1 Motivation

The interest on new multi-disciplinary areas of research, like biomechanics or biomicrofluidics, where physicist and engineers partner with biologist to explore different biological phenomena, is outgrowing with time. This is the area where engineering mechanics along with numerous biological activities are to be investigated. Modern technologies have provided new insights, perspective and scientific tools to better understand the complex bio-physical processes important for natural evolution and in broad the natural environment. One such complex bio-physical process is the biofilm formation by microorganisms which is a key phenomenon for the evolution of life cycle. This process is also involved in a well-known ‘sticky’ problem called ‘biofouling’. Biofouling is the unwanted growth of sessile microorganisms on submerged surfaces which presents a serious problem for the underwater structures and water vessels. The variables regulating the biofilm formation include different biological and chemical cues, and also some physical/mechanical parameters such as the ambient microfluidic environment around microorganisms. The former two variables (ie different cues) have been studied intensively while the later one have started gaining attention very recently, especially in relation to biofouling control mechanism. The analysis of microfluidic environment and its relation with biofouling could be an interesting area of research for present days.

It is well-established that biofouling can be controlled to various degrees with different synthetic microstructure-based patterned surfaces. In most of the cases, these patterned surfaces are artificially fabricated surfaces with micro-scale roughness on it. The idea of fabricating microstructure-based patterned surfaces came from a number of natural biological surfaces showing antifouling (AF) characteristics with microtopographical arrangements (eg shark skin, lotus leaves, the body surfaces of different benthic invertebrates such as, blue mussels, edible crabs, the egg-cases of the lesser-spotted dogfish, brittle stars). For example, the Sharklet^{TM} surface pattern has been developed synthetically being inspired by the actual impression of shark skin. The shark skin has dermal denticles on its surface which are analogous to tiny riblets with distinct diamond pattern. The Sharklet^{TM} pattern was developed following the arrangement of dermal denticles of shark skin. Some commercially available glasses (eg BalcoNano^{TM}) have been developed inspired by the natural water repellence of lotus leaves. While these biomimetic patterned surfaces are on the verge of substantial field-level applications, the understanding of the underlying mechanism of their transitory AF characteristics is still imprecise. Researchers have long speculated that microtopographies might influence the near-surface microfluidic conditions, thus microhydrodynamically preventing the settlement of microorganisms. It is therefore very important to identify the microfluidic environment developed on patterned surfaces and its relation with the antifouling behaviour of those surfaces. The role of microhydrodynamics on the settlement of microorganisms can be studied from a robust perspective by implementing sophisticated engineering tools and novel scientific frameworks such as computational simulations, microtechnologies and relevant lab experiments. A better understanding on the settlement of microorganisms and associated low Reynolds numbers (*Re*) swimming environment will not only facilitate the design of an optimized AF surface, but can also contribute novel solutions and knowledge to this emerging AF technology.

1.2 Objective

This dissertation aims to gain a deeper insight in the microhydrodynamics regulating the settlement of microorganisms over plain and patterned surfaces by conducting novel experiments with a microchannel-based flow cell reactor system on rod-shaped bacterium *Escherichia coli*. Using the insight of a microfluidics platform, the present study intended to investigate the hydro-mechanical effects on bacterial settlement suppressing the biological processes in some cases. This dissertation presents a detailed account of the design, computation and experimental validation of a microfluidic platform to probe bacterial dynamics in response to plain/microtopographic boundary surfaces. The newly developed approach has been instrumental in elucidating bacterial settlement process and the associated microfluidic environment over patterned surfaces which clarifies the underlying mechanism of the AF efficacy shown by those surfaces. Full details of the design and set-up of the microbiological experiments and the numerical simulations that demonstrate the basic microhydrodynamics parameters for inhibiting the bacterial settlement have been presented in the following chapters.

1.3 Research Questions

- What is the underlying mechanism of AF behaviour exhibited by patterned surfaces?
- How the microfluidic conditions change around a swimming microorganism near a solid surface?
- Is there any relation between the fluctuating microfluidic conditions and the initial settlement/biofilm formation of microorganisms on patterned surfaces?
- How does the presence of solid boundaries affect the dynamics and trajectories of the swimming microorganisms near to the surface?
- Is the change in swimming behaviour of a near-surface microorganism more related to biological, fluid mechanical, or other physical laws?
- How to optimize the microstructure-based surface design for better AF capabilities?

1.4 Contributions

The research presented in this dissertation has resulted from multidisciplinary works involving several schools of RMIT. Therefore, the author’s contributions need to be specified for the purpose of intellectual property.

Chapters 2 and 3

These chapters are mainly related to literature review and the theoretical background of the applied numerical approach. A detail description of the overall biofouling problem (eg its origin and development processes), current protection strategies and related hydrodynamic researches have been presented in Chapter 2 based on existing literature and a number of technical reports. To prepare and demonstrate the numerical processes presented in Chapter 3, the CFX documentations were followed released by ANSYS Inc., USA in 2011, as well as some relevant text books/ journal papers (eg Barth and Jesperson 1989; Darwish and Moukalled 2003; Versteeg and Malalasekera 2007). Here to be noted that, commercially available computational fluid dynamics (CFD) software was used ANSYS CFX to carry out all the numerical simulations presented in this study. In Chapter 3, the basic CFD technique was demonstrated based on existing theoretical background and adapted from some of the frequently used CFD methods for fluid flow analysis.

Chapter 4

This chapter will focus on the materials and methods of microfabrication applied in this study using conventional photolithography technique. Patterned surfaces and microchannels, as used in two separate microbiological experiments, were fabricated in the Microelectronic and Materials Technology Centre (MMTC) at RMIT University. The photolithography technique presented in Chapter 4 is based on the standard procedures followed in the MMTC lab.

Chapter 5

Use of microstructure-based microfluidic channel was proposed for the experimental set-up and CFD simulations were performed accordingly to characterize the flow fields inside the channel. A set of microbiological experiments was conducted to develop biofilms on microwell-based patterned surfaces in a controlled environment inside the microchannel. All the surfaces were evaluated by an environmental scanning electron microscopic (ESEM; FEI Quanta 200, FEI Company, Hillsboro, OR, USA) which was facilitated by RMIT Microscopy and Microanalysis Facility (RMMF) located at RMIT University.

Chapter 6

The second microbiological experiment was conducted to identify individual bacterial motility by using time-lapse imaging technique. A commercially available time-lapse imaging module (LAS MultiTime® module) has been used in this study for the video microscopy and image processing. The experimental set-up was re-designed from the first set of experiments, which included a single array of microwells instead of a series of microwell arrays on the microchannel bed and an integrated time-lapse imaging system. CFD simulations also performed to characterize individual bacterial trajectories over plain and microwell-based patterned surfaces.

Chapter 7

The idea of optimized AF surface pattern based on microfluidic analysis has been demonstrated in this chapter. Some patterns were also suggested to go through further investigated in future in relation to biofouling control.

1.5 Thesis outline

The thesis will be structured as follows:

Chapter 2 begins with an overview of biofouling and its control for underwater surfaces. The description would include the biofilm development process, its consequences and world-wide protection strategies.

Chapter 3 illuminates on general description of CFD technique and the immersed solid solution method applied in this research.

Chapter 4 focuses on the materials and methods of microfabrication based on photolithography technique.

Chapter 5 begins with the idea of patterned surfaces, the first set of microbiological experiments with different sizes and spacing of microwell arrays, relevant CFD analysis and discussions.

Chapter 6 presents another re-designed microbiological experiment with single array of microwells, relevant CFD analysis and discussions.

Chapter 7 presents the outcome of this thesis, conclusions and future works.

Chapter 2

2 Literature review

2.1 Overview of biofouling and its control

Biofouling, the unwanted growth of microorganisms on submerged surfaces, is a well-known problem for hydraulic structures, water vessels, heat exchangers, oceanographic sensors and aquaculture systems (Azis et al. 2001; Railkin 2004; Rosehahn et al. 2010; Callow and Callow 2011). Biofouling is a hierarchical process triggered by organic conditioning of underwater surfaces. The attachment and growth of sessile microorganisms leads to biofouling. The process starts at a very small scale in the nm–μm range, or even at the molecular level (Railkin 2004; Rosehahn et al. 2010; Callow and Callow 2011). Organic molecules and matter from the aquatic environment rapidly condition any ‘clean’ surface underwater. The formation of a biofilm, composed of bacteria and soft fouling unicellular algae, starts within hours. More complex organisms, such as barnacles, mussels and tubeworms populate the surface at a later stage. These processes can continue over years and are difficult to control as they can withstand very harsh environments. Biofouling is a classic example of evolution being optimized by nature for millions of years (Rosehahn et al. 2010).

Conventionally the underwater structures are being protected against biofouling by metal based antifouling coatings. The use of antifouling coatings, in particular those containing Copper and Tributyltin (TBT), are posing more ecological concern due to harmful effects and thus led to a mounting interest in developing non-toxic alternatives. TBT was first banned on vessels <25 m in length in most industrialized countries and has subsequently spurred a worldwide ban (Swain 1998). As per the International Maritime Organization

(IMO) treaty on biocides in 2008, the use of TBT is restricted (Champ 2003, Schultz et al. 2011) for all vessels.

One of the non-toxic approaches to control biofouling is to modify the settlement surface. This usually entails altering the surface topography and roughness, and developing a surface with a microstructured pattern (Flemming and Ridgway 2009; Vladkova 2009; Callow and Callow 2011; Scardino and de Nys 2011). Studies showed that patterned surfaces inhibit the initial settlement of microorganisms to various degrees based on the nature of the surface and associated flow conditions (Flemming and Ridgway 2009; Scardino and de Nys 2011; Halder et al. 2013). However, the antifouling effects of microtopographies are still weak, specific and transitory, and need further investigation before application to real-world scenarios.

Considering the benefits of using a non-toxic, self-cleaning surfaces over ecologically sensitive tributyltin-based coatings, it is very important to identify the antifouling mechanism of different patterned surfaces and thus to optimize their design parameters. While a number of studies have investigated the influence of surface structural features (eg height, inclination, orientation, roughness density and shape geometry) on the settlement of microorganisms and accumulation of biofouling (Callow et al. 2002; Scardino et al. 2006, 2008; Long et al. 2010a, 2010b), only a few studies (Petronis et al. 2000; Bers and Wahl 2004; Koehl 2007) have addressed the importance of studying the microhydrodynamics of patterned surfaces. It is essential to investigate the microfluidic environment in detail as it will influence the mechanotransduction process of a settling microorganism. Mechanotransduction refers to converting mechanical forces into biochemical signals and integrating these signals into the cellular responses. Microorganisms experience a range of mechanical (hydrodynamic) forces that can have significant effects on cellular function and signaling (Huang et al. 2004). Microorganisms may experience differential strain rates (shear rates) in microstructured areas, shear forces at or near surface microtopographies, extensional forces as a result of velocity fluctuations (acceleration) at sites of abrupt level changes (periodic protrusion/depression), tensile and compressive forces upon cell bodies due to impact with microtopographies and advective transport phenomenon within regions of flow recirculation or turbulence. Schumacher et al. (2008) considered this mechanotransduction on settling microorganisms in their study and developed the Engineered Roughness Index in relation to structural features of patterned surfaces, instead of considering near-surface microhydrodynamics. In contrast, Petronis et al. (2000) and Bers and Wahl (2004) assumed that patterned surfaces might influence near-surface fluid dynamics and thus microhydrodynamically prevent the settlement of microrganisms. Koehl (2007) stated that the local flow patterns around individual roughness elements on a surface are probably the most important features of the boundary layer to determine the larval (eg barnacle) settlement. Microfluidic analysis, however, was not performed in these investigations. Microhydrodynamics on microtopographies has been studied intensively for drag reduction and superhydrophobicity (Goldstein and Tuan 1998; Bechert 2000a; Friedmann 2010a, 2010b; Carlborg and Wijngaart 2011), but received little attention in relation to the control of biofouling.

From this discussion, it can be stated that a clear research gap exists in the sector of AF research, and that is the investigation of microhydrodynamics on microtopographies and how it affects the biofilm development process. The investigation of microhydrodynamics is important because this biofilm development processes have also considerable impacts on the later stage fouling (Mieszkin et al. 2013). A general overview on all fouling types, including biofouling, has been demonstrated in the following sections.

2.2 Fouling categories

In general, fouling is the undesired deposition of materials on surfaces. The word ‘fouling’ carries a negative connotation which implies that this accumulation is detrimental (Schumacher 2007c). Fouling can be categorized into three different types:

- Inorganic fouling: deposition of inorganic material precipitating on surface
- Organic fouling: deposition of organic substances on surfaces
- Biofouling: adhesion of microorganisms to surfaces and subsequent biofilm development

2.2.1 Inorganic fouling

Inorganic fouling includes a variety of micro-scale fouling, such as scaling or precipitation fouling, particulate or mineral fouling, sediment fouling and corrosion fouling. Scaling or precipitation fouling involves the crystallization of inorganic salts, oxides and hydroxides such as $CaCO_3$, $Ca(OH)_2$, $NaSO_4$, $MgSiO_3$, and Li_2SO_4 (Epstein 1981). This type of fouling occurs frequently on superheated surfaces like heat transfer equipment (Somerscales 1981), but can also occur in hard water or aqueous solutions under moderate heating (Epstein 1981). Particulate fouling involves the accumulation of colloidal particles on surfaces. In sediment fouling, silica, clay and other inorganic sediment particles deposit on submerged surfaces. Corrosion fouling is the in-situ growth of corrosion deposits, such as magnetite on carbon steel surface.

2.2.2 Organic fouling

Organic fouling, also known as biochemical conditioning, is the deposition or adsorption of bulk organic matter (OM) on surfaces which includes different macromolecules, such as natural organic matter (NOM) from humic substances, algal organic matter (AOM) consisting of extracellular and intracellular macromolecules and cellular debris, soluble microbial products (SMPs) derived from biological wastewater consisting of proteins and polysaccharides (Gary 2007). Macromolecules in seawater are mostly glycoproteins, proteoglucans and polysaccharides (Wahl 1989). Organic fouling begins on the material surface within seconds after immersion of the surface and a dynamic equilibrium is reached within few hours. This accumulation of organic matter leads to the development of a biochemically conditioned surface (Wahl 1989). The process of conditioning alters the physicochemical properties of the surface such as surface free energy (gamma-values) and wettability (ie hydrophobicity). By the process of organic conditioning, physical and chemical surface properties converge so that low-energy (hydrophobic) surfaces experience an increase and high-energy (hydrophilic) surfaces a decrease of their gamma values. The centre of this convergence seems to be a gamma-range between 20 and 30 dyne cm^{-1} (Baier 1981). The chemical composition of the adsorbing film is independent of the initial surface free energy of the substratum and firmly attached at very high or very low surface energy substratum. On the other hand, the adsorbing film shows a flocculent, loosely bound aspect on substrata with medium range of surface free energy (~20–30 dyne cm^{-1}) (Baier 1981). Thus, the organic conditioning changes the surface properties and prepares the surface for the later stage attachment of biological organisms.

2.2.3 Biofouling

Biofouling, as a process means biological fouling, is distinct from other forms of fouling described above. It is the undesirable settlement, attachment, or growth of living organisms and cells on surfaces in the water medium. It can be further categorized into two branches: microfouling and macrofouling.

Microfouling is the biofilm formation and bacterial adhesion while macrofouling is the attachment of larger organisms. Macrofouling includes hard and soft foulers. Hard foulers are, for example, barnacles, bryozoans, mollusks, polychaete, tubeworms, zebra mussels, etc. Soft foulers are non-calcareous fouling organisms like seaweeds, hydroids, algae and biofilm ‘slime’. A biofilm consists of millions of bacteria, encased in extracellular polymeric substances (EPS), which are secreted by microorganisms. Biofouling is a hierarchical process in length and time scales (Characklis 1981; Railkin 2004; Callow and Callow 2011). Figure 2.1 shows a schematic diagram of the hierarchical accumulation/colonization of different species involved in biofouling. The common processes that underlie biofouling of any natural and artificial hard surfaces by any organisms are: transport, settlement, attachment, development and growth. These elementary processes replace each other sequentially during surface colonization by micro- and macrofoulers (Railkin 2004).

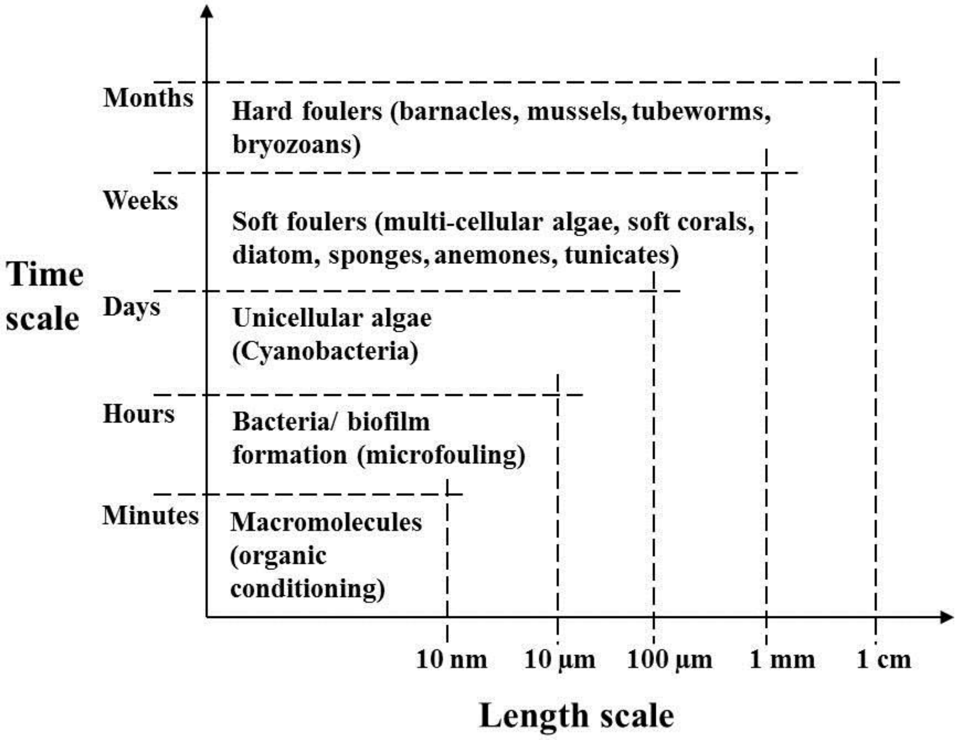

Figure 2.1: A schematic diagram of biofouling showing the hierarchical accumulation/ colonization of different species at different length and time scales.

This diagram (Figure 2.1) is a linear ‘successional’ model of settlement. However, some authors (Clare et al. 1992; Rittschof 2010) considered that this ‘classical’ model is an oversimplification, leading to unwarranted assumptions about causality (Mieszkin et al. 2013). In reality, bacterial biofilms have a variety of positive, negative or neutral interactions with higher fouling organisms such as algal spores and larvae of invertebrates (Dobretsov et al. 2006, 2013; Qian et al. 2007; Hadfield 2011; Mieszkin et al. 2013).

Here, it should be noted that the present study investigated only one single category of the fouling (ie biofouling) and at a scale of individual swimming cells (cell body size ~ 2–5 µm). The overall fouling on surfaces in submerged conditions (marine/ freshwater) is an immense field of study which is mostly out of scope of this current research.

2.3 Biofilm development processes

The attachment of microorganisms in complex, slime-encased communities is called biofilms. Biofilms are ubiquitous in nature. There they are most often seen as layers of slime on rocks or other objects in water. Biofilms can form on virtually any surface, once it has been conditioned by proteins and other molecules present in the environment (biochemical conditioning). Microorganisms reversibly attach to the conditioned surface and eventually begin releasing polysaccharides, proteins, and DNA. These polymers allow the microbes to stick more stably to the surface. As the biofilm thickens and matures, the encased organisms reproduce and secrete additional polymers. The end result is a complex, dynamic community of microorganisms (Willey et al. 2008). The key processes involved in the biofilm development are cell deposition and adsorption, cell-to-cell signalling (quorum sensing), replication and growth, secretion of the polysaccharide matrix and finally detachment, erosion and sloughing (Figure 2.2). Once the biofilm is formed on any submerged surface, it is very difficult to control later stage biofouling. While in the biofilm, microorganisms are protected from numerous harmful agents such as UV light, antibiotics, and other antimicrobial agents (Stoodley 2004; Willey et al. 2008). Charaklis (1981) comprehensively detailed the development of biofilm and related process. Railkin (2004) also described the steps involved in the bacterial colonization in a simplified manner, referring to Charaklis (1981), as: transport of organic molecules and bacteria towards a submerged surface, adsorption of organic molecules, attachment of bacteria to the conditioned surface, metabolism of attached microorganisms, growth of bacteria, and finally the detachment of part of the bacterial film.

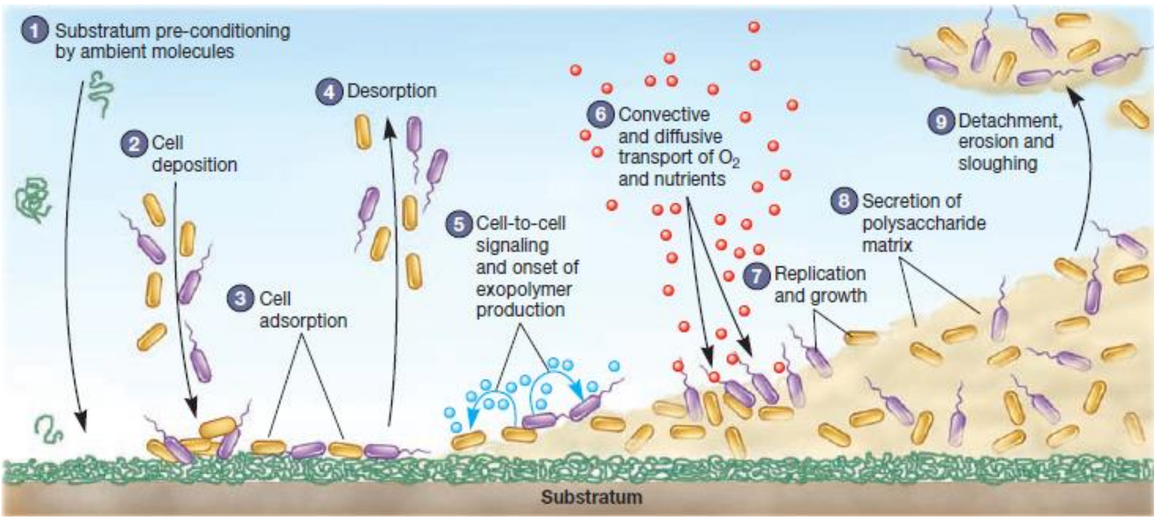

Figure 2.2: The key processes involved in the biofilm development: (1) organic conditioning (2) cell deposition (3) cell adsorption (4) desorption (5) quorum sensing (6) nutrients transport (7) replication and growth (8) secretion of EPS (9) detachment, erosion and sloughing (source: Willey et al. 2008).

Microorganisms living in biofilms are mostly bacteria, fungi, protozoa, algae and invertebrates. Wahl (1989, 1997), like many other authors, distinguishes bacterial colonization from other form of fouling such as, biochemical conditioning, colonization by unicellular eukaryonts and colonization by multi-cellular eukaryonts. Biofilms growing in fast-moving water (eg drainage run-off, rivers and water transport pipelines) tend to form filamentous streamers, while in quiescent waters biofilms tend to form mushroom or mound-like structures. In situ observation of biofilm structure using confocal laser microscopy showed sessile bacteria growing in heterogeneous matrix-enclosed microcolonies interspersed with open water channels. These channels are facilitating the nutrients uptake by infusing fluid from the bulk phase into the biofilms. Thus biofilms are complex and differentiated, rather than simple and uniform, and fully functional in nutrients and waste-product exchange (Stoodley et al. 2004).

2.4 Effects of biofouling

Most of the fouling mechanisms (eg corrosion, crystallization, chemical reactions, suspension of particles and detritus, organic deposition and accumulation) are passive while biofouling is an active process with live cells and organisms. In passive fouling processes (inorganic/organic fouling), the increase of fouling layer depends simply on material transport and abiotic accumulation coming directly from water. So these kinds of fouling can be controlled externally by reducing foulant transport through water to the system. The most common pre-treatments involved in controlling inorganic/organic fouling are direct mechanical removals or filtering processes. But for biofouling problem, even if 99.99% of all bacteria are eliminated by pre-treatments (eg micro-filtration, biocide application), a few surviving cells may enter into the system to adhere to the surfaces and multiply at the expense of biodegradable substances dissolved in water. Initial biofilm formation creates the surface for a variety of other micro- and macroorganisms. In the coastal water of the Arabian Gulf, it has been found that the biofouling community is composed of 31 groups of organisms which exhibit a widely varying pattern of incidence, abundance and succession (Azis et al. 2001). Though the effects of biofouling are global and in most cases detrimental, the degree of intensity differs highly case to case. The most common cases in seawater environment are vessels and their water conduits, navigational equipment, stationary structures, industrial pipelines, fixed submerged surfaces, and flotsam (Reznichenko 1978). Characklis (1981) gave a detail description of biofouling effects, involved processes and subsequent losses, and concern bodies (industry/ organization). According to him, biofilm formation/ biofouling is a tremendous problem for many industries like shipping, power, chemical process, water treatment, and pulp and paper industry and also for other sectors like public health, dental health, solar energy systems and municipal utilities. Major fouling areas and their economic impacts are described in the following sections.

2.4.1 Ship Hull Fouling

Biofouling on ships increases the surface roughness of the hull which, in turn, causes increased frictional resistance and fuel consumption and decreased top speed and range (Schultz et al. 2011). It incurs large functional and monetary costs by increasing drag and biocorrosion. Marine biofouling of ship hulls depends on the region of operation, the time ratio of anchorage and sailing, speed regime, the method of hull coating, and docking frequency (Railkin 2004). Fouling of ship hulls has long been noted and much of the early works is reviewed by Redfield and Ketchum (1952). The surface condition of the hull is of primary importance in the performance of marine vehicles. Frictional drag on some hull types can account for as much as 90% of the total drag even when the hull is free of fouling (Kempf 1937). For this reason, understanding and predicting frictional drag has been an active area of research for many years. Several studies have investigated the effect of surface roughness on the frictional drag of unfouled AF coatings, including the work of Townsin et al. (1981), Granville (1987), Medhurst (1989) and Grigson (1992). Subsequent hydrodynamic research has included laboratory studies of the effects of biofilms (Watanabe et al. 1969; Picologlou et al. 1980; Schultz and Swain 1999), filamentous algae (Schultz and Swain 2000), and calcareous macrofouling (Leer-Andersen and Larsson 2003; Schultz 2004) on the frictional drag and ship cruising. Full-scale ship testing to document the effect of fouling on the drag of copper-based coatings has also been conducted (Lewthwaite et al. 1985; Haslbeck and Bohlander 1992). The results of all these studies indicate that frictional resistance due to micro- and macrofouling increase the drag, result in loss of speed (40% or more) and increase operational costs. More recently, Schultz (2007) reviewed the effects of coating roughness and biofouling on ship resistance and powering. He analysed the effects of antifouling coating systems with a range of roughness and fouling conditions on a mid-sized naval surface combatant at cruising speed (7.7 ms^{-1} or 15 knots) and near maximum speed (15.4 ms^{-1} or 30 knots). He made a few predictions on ship resistance and powering from scale model testing of the ship. From his analysis, it is evident that slime films can lead to significant increases in resistance and powering, and heavy calcareous fouling results in powering penalties up to 86% at cruising speed. Schultz et al. (2011), in their recent study, reported the cumulative costs per ship over fifteen years for hull roughness conditions. These included an ideal hydraulically-smooth paint (Case 1), a newly applied Navy-qualified ablative AF coating with no fouling (Case 2), a typical hull roughness given the US Navy’s present practices including qualified ablative AF coatings and regular interim and full hull cleanings (Case 3), and a scenario featuring an upper bound for hull fouling (Case 4). They showed that for hydraulically-smooth hull scenario the fuel cost is $11.1 million (M) per ship per year, which was considered the baseline cost for a propulsive vessel and applicable to all other cases. It was also considered that there is no additional fuel cost resulting from hull paint roughness or fouling in the case of an ideal hydraulically-smooth ship hull (hypothetical). The cumulative costs over 15 years, over and above the fuel cost (baseline cost), are entirely due to surface preparation and painting and amount to approximately $0.45 M per ship. The Navy’s qualified ablative AF hull coatings generate additional hull roughness even when unfouled (Case 2). In this case, the 15 year cumulative cost (over the baseline cost) is approximately $3.33 M per ship. Despite the vessel remaining free of fouling, the typical paint roughness of as-applied AF coatings leads to an increase in fuel consumption of 1.4% per year, or about $0.15 M per ship per year. For Case 3 and 4, The 15 year cumulative cost (over baseline) for operations under current Navy hull maintenance practices is approximately $22.7M per ship. For the worst-case scenario (Case 4), representing a ship operating with a mixed community of relatively small hard fouling organisms, the cumulative cost over 15 years from coating roughness and fouling is approximately $43.8M per ship. The economic analysis on a mid-sized naval surface ship (Arleigh Burkeclass destroyer DDG-51) showed that the overall economic impact of hull fouling is estimated to be $56M per year for the entire DDG-51 class or $1billion over 15 years.

In Russia, according to technical standards, the hull roughness cannot exceed 0.12 to 0.15 mm at the time of building. The increase in hull roughness by only 0.025 mm raises its friction by 2.5% and results in extra fuel consumption (Railkin 2004). In some cases, fouling of the propeller blades is a more important cause of fuel waste than fouling of the ship’s hull (Railkin 2004). The US Navy and the Office of Naval Research (ONR) have been pursuing the development of non-biocidal, antifouling and foul-release marine coatings for over ten years. There has yet to be an effective solution that complies with the current and anticipated federal and international regulations regarding marine coatings (Yebra 2004). The overall hull fouling cost associated with US Navy fleet is approximately between $180 and $260 M per annum (Callow and Callow 2011). There are other consequences of ship hull fouling. For example, the dense layer of macroorganisms (eg bryozoans, barnacles) may screen the release of toxic substances from antifouling coating and thus reduce its effectiveness. Barnacles also damage paint coating by growing into it (Railkin 2004). Biocorrosion, resulting from the biochemical activities of organisms on submerged surfaces, is also a frequent cause of destruction of different ship systems. Figure 2.3 shows barnacle fouling on ship hull and algal fouling on submarine.

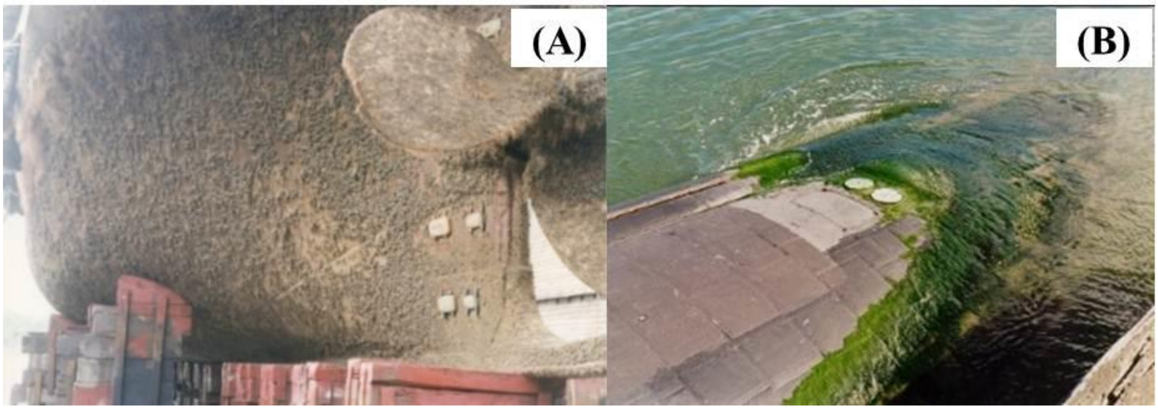

Figure 2.3: Marine vessels fouling: (A) ship hull fouling by barnacles (source: Rosehahn et al. 2010), (B) green algal (seaweed) fouling on submarine hull (source: Callow and Callow 2011).

2.4.2 Heat exchangers fouling

Mostly responsible for fouling on the water side of a heat exchanger are scaling, corrosion and often also microorganism causing biofouling. The scale is formed mostly by salts solved or solids carried in the water. The corrosion is caused by aggressive water and the biofouling is caused by algae or bacteria in the water which are forming a biofilm at the surfaces of the heat exchanger. The development of bacteria on the inner walls of heat exchangers stimulates settlement of the larvae of invertebrates and accelerates the process of biofouling (Railkin 2004). The layer of micro- and macrofoulers, together with sediments and corrosion products, serves as a buffer between service water (ie water inside the cooling tubes) and the water pumped in from the sea. This biological heat insulating layer reduces the effectiveness of heat exchangers, which results in energy losses and premature deterioration of different machines and mechanisms. Biofouling also accelerates corrosion of the metal walls of heat exchangers. The presence of a biofilm on transfer surfaces of heat exchangers cooled by seawater reduces the heat transfer rate by 20 to 50% and incurs a global expenditure of over $15 billion per annum to control the problem (Azis et al. 2001). Figure 2.4 shows heat exchanger fouling with scaling and corrosion.

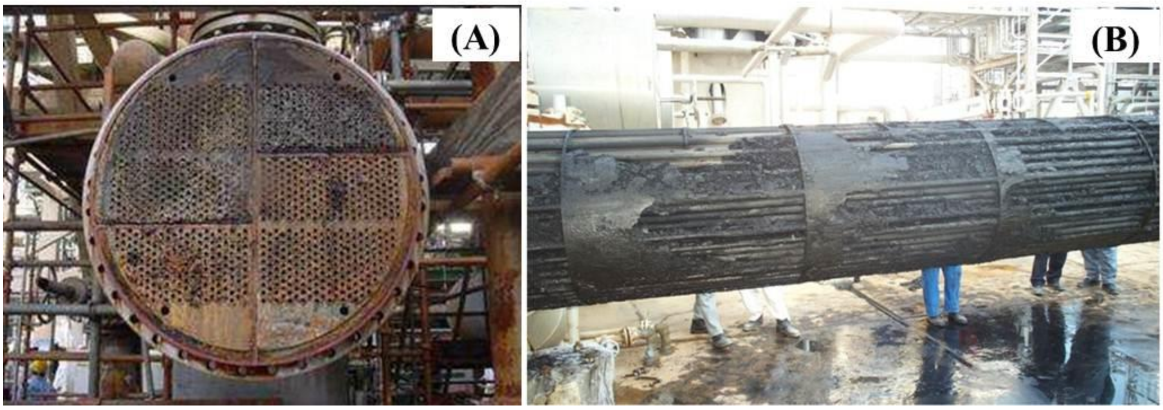

Figure 2.4: Heat exchanger fouling (sources: (A) MERUS - The water conditioner company (www.merusonline.com) and (B) Ibrahim 2012).

2.4.3 Seawater intake fouling

Biofouling is a major problem for seawater intake structure, screens and intake piping system. There are different kinds of seawater intake system for desalination plants. Broadly, they are categorized into surface (open), subsurface, shared existing and converted existing intakes. According to a recent study by the Water Research Foundation (2011), open/surface intakes located above the seafloor are the most common type of intake for large plants (eg production >10^6 gallons per day). Open intakes are also the most vulnerable type of intake in a marine environment. Total water conveyance system and intake heads are habitat of marine life and different organisms. Intake grills are subjected to heavy fouling and frequent clogging. The biomass of hydroids, barnacles, and bryozoans can develop heavy fouling on grates, in some cases up to 16 kgm^{-2} (Starostin and Permitin 1963). Figure 2.5 shows that the seawater intake head installed at Perth desalination plant, Australia is under heavy fouling within 1.5 years of its operation.

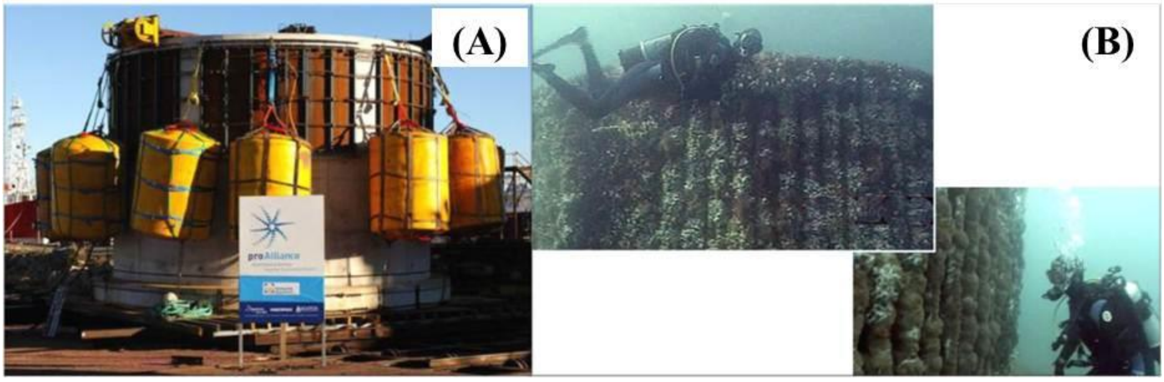

Figure 2.5: Seawater intake head installation (left) and biofouling in the intake head grills after 1.5 years of operation (right). (Source: Pankratz 2008).

2.4.4 Navigational equipment fouling

Biofouling of navigational buoys in the coastal waters of even such a temperate sea as the Baltic Sea may reach masses of several kilograms per square meter, whereas in subtropical seas, it may be up to 70 kgm^{-2} (Yan et al. 1994). Biofouling hampers the operational characteristics of buoys and beacons, optical sensing instruments (OCN) and other oceanographic equipment (Figure 2.6). Heavy fouling may even cause buoys and beacons to sink (Railkin 2004).

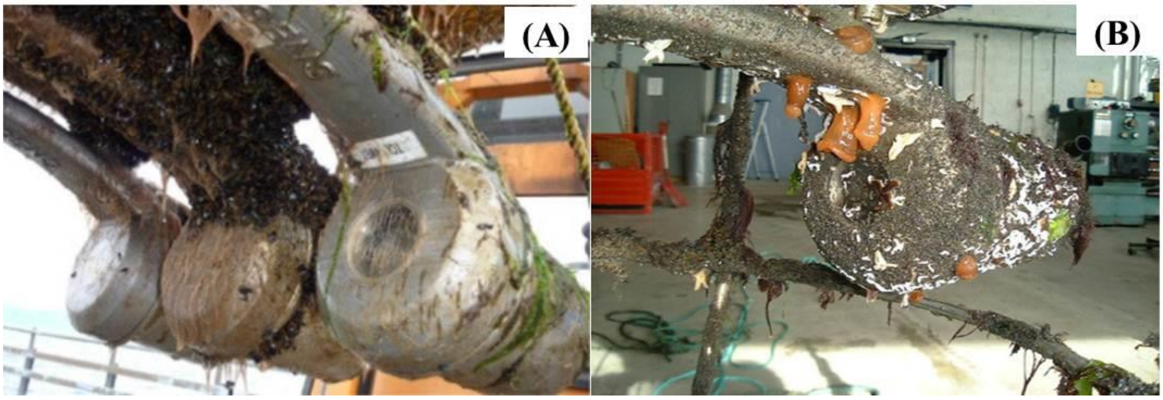

Figure 2.6: Fouling on: (A) oceanographic optical sensing instruments (OCN) and (B) turbidity sensor instrument (source: AMBIO 2010).

2.4.5 Membrane fouling

In the area of membrane technology, microfiltration and ultrafiltration membranes are used for drinking water production and wastewater treatment. The primary limitation to the more widespread adoption of membrane filtration is fouling with microorganisms and organic molecules (Figure 2.7) which leads to a significant decline of the permeate flux, higher energy consumption, and eventually, failure to meet the regulatory standards. Frequent cleaning of the membranes is costly and may damage the membrane material/barrier layers.

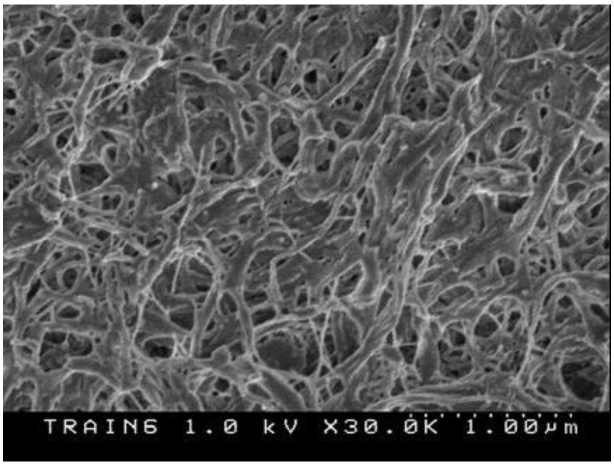

Figure 2.7: Membrane fouling (source: the final activity report, AMBIO 2010).

2.4.6 Human health related fouling

Biofilm formation on teeth causes dental plaque and caries. Micro-scale fouling (bacterial infection) is very common in lungs, intestinal and urinary tracks (Charaklis 1981). Many nosocomial infections (ie hospital-acquired infection) are directly related to bacterial biofilm formation. For example, catheter-associated urinary tract infection (CAUTI), the most common nosocomial infection, is due to colonization and infection of the urinary tract with the antibiotic-resistant bacteria (Reddy et al. 2011). Figure 2.8 shows the Scanning Electron Microscopy (SEM) images of bacterial settlement on the urinary catheter surfaces.

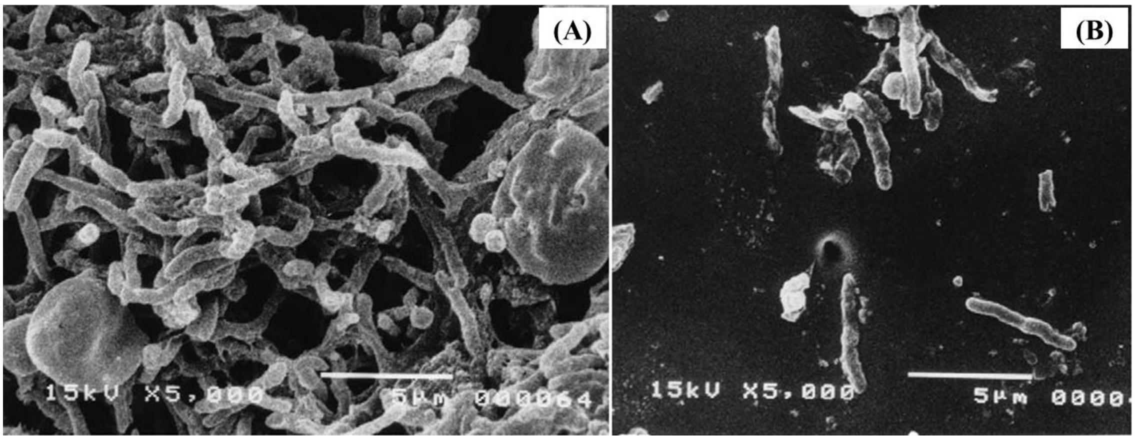

Figure 2.8: Scanning electron micrographs of fouling on the catheter surfaces from patients catheterised for 7 days with (A) a silicone urinary catheter and (B) a nitrofurazone-coated catheter. (Source: Lee et al. 2004).

2.4.7 Fouling of fish farming structures

Biofouling is a major problem throughout the global aquaculture industries (Figure 2.9). Biofouling on farm infrastructure greatly reduces the efficiency of materials and equipment. Problem areas include immersed offshore-structures such as cages, netting and pontoons, on-shore equipment and structures such as pipelines, pumps, filters and holding tanks.

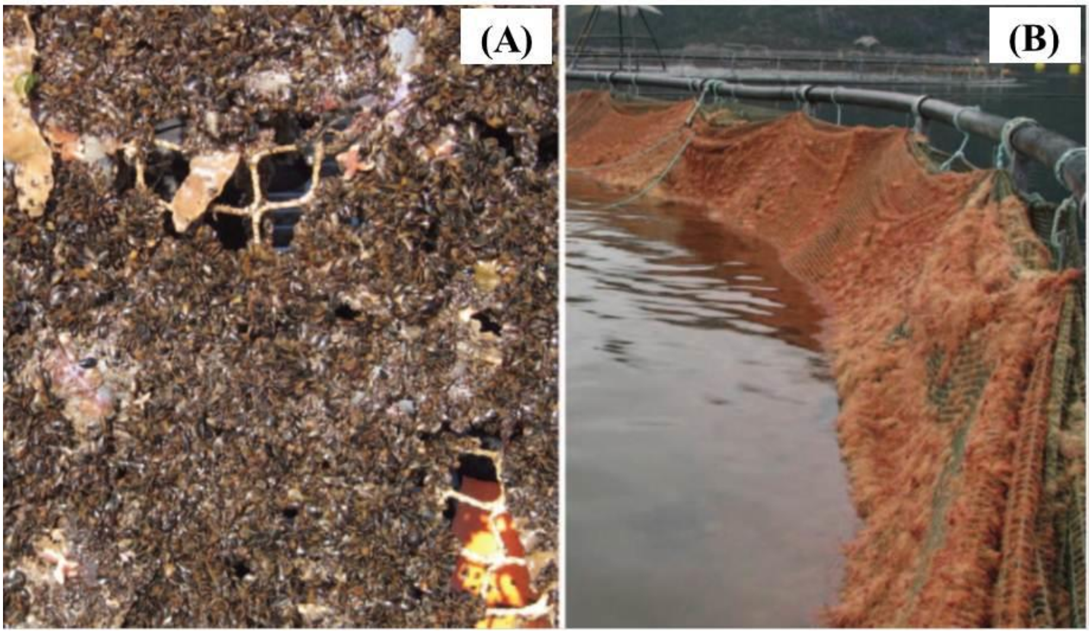

Figure 2.9: Common fouling organisms associated with aquaculture operations: (A) *Mytilus edulis* (blue mussel); (B) *Ectopleura larynx* (ringed tubularia). (Source: Fitridge et al. 2012).

2.5 Current biofouling protection strategies

Three main approaches are commonly being practised to control biofouling:

- **Mechanical detachment:** using wipers, brushes, hydrodynamic shear force (ie pressurized water jet). Most of the mechanical detachments are through manual cleaning and operations.
- **Biocide application:** total killing approach adapted using antibiotics, biocides, and cleaning chemicals.
- **Surface modification:** usually alters the surface chemical composition and morphology, the hydrophobic/hydrophilic balance, surface energy and polarity by applying antifouling paint coatings. Another recent approach of surface modification is changing the surface topography and roughness by developing microstructure-based pattern surfaces. This approach is the main interest of the current research.

Mechanical approach has been proved very costly and a temporary solution for the biofouling problem. Moreover, the periodic manual cleaning and mechanical detachment make the surface more rough and easy growing environment for fouling organisms. Jannet et al. (1981) showed that the brush cleaning procedure ready the surface developing denser biofilm and heavy macrofouling on later stages. Also the use of biocide and AF coatings employing copper and/or co-biocides are posing serious threat against the environment. The incorporation of biocides into coatings makes them toxic to marine organisms and impact non-target species. Because of this total killing approach of biocides copper and co-biocides, an increased environmental scrutiny becomes necessary and it develops a mounting interest for non-toxic coating and alternatives.

The surface modification approach utilizes the application of prefabricated microtopography to inhibit the initial settlement of microorganisms on the submerged surfaces. This approach is based on the assumption that a defined and periodic surface structure will make the surface appear unfavourable for the settlement of microorganisms. While some of these microtopographic surfaces showed transitory AF efficacy, the real cause of their AF mechanism is still unclear. The current research is considering that the microtopographies might influence near-surface microfluidic conditions, and thus microhydrodynamically preventing the settlement of microorganisms.

2.6 Current state of research

In one of the largest research projects on antifouling paints, named: Advanced Nanostructured Surfaces for the Control of Biofouling (AMBIO), 31 organizations and research institutions across Europe, aimed to develop new types of nanostructured fouling prevention polymeric surface coatings that mimic natural non-fouling surfaces (AMBIO 2010). Recent publications from this project, reviewed many environmentally friendly fouling-resistant marine coatings like bioinspired engineered topographies, amphiphilic nanostructured coatings, phase-segregating siloxane-polyurethane copolymers, superhydrophilic zwitterionic polymers, inorganic-organic nano-hybrids, nano-composites and superhydrophobic surfaces (Callow and Callow 2011). However, many of the physicochemical factors influencing bioadhesion and biofouling are still unclear, such as surface free energy and related parameters, water contact angle and contact angle hysteresis, elastic modulus, surface chemistry, surface roughness and topography with biological responses, creation of very low surface energy ‘theta-surface’ and underwater superhydrophobicity (ie lotus effect). To understand the evolutionary mechanism of biofouling and to develop environmentally benign non-fouling surface, a multi-disciplinary knowledge and systematic approach are required. The biofouling problem is ubiquitous and attended interest from many fields of science and technology, such as marine biology, microbiology, surface science, material science, environmental science and micro/nanotechnology. The biofouling related research is so diversified that it is very difficult to follow a single stream of progress. Table 2.1 shows a glimpse of these studies.

Table 2.1: Research on biofilms, AF surfaces and related hydrodynamics

Research stream	**Research theme**	**References**
Biofilms - Physical properties of biofilms	- Biofilm material properties (eg elasticity, shear modulus) and geometrical characteristics - Biofilm development and substrate utilization	Picioreanu et al. (2001, 2009); Stoodley et al. (1998,1999, 2001ab, 2002)
- Biofilms under hydrodynamic conditions	- drag and oscillatory behaviour of single biofilm streamer under different flow conditions - critical shear stress development to detach biofilms	Horn et al. (2003); Bol et al. (2008); Taherzadeh et al. (2010)
Microstructure-based surfaces - Transitory AF characteristics	- Synthetic microstructure-based AF surfaces	Andersson et al. (1999); Petronis et al. (2000); Bers and Wahl (2004); Patankar (2004); Schumacher et al. (2007a, 2007b, 2008); Bhushan and Jung (2011)
- Underwater superhydrophobicity (UWSH) and air entrapment inside grooves	- Air entrapment inside the grooves of microstructure-based surfaces - Lotus effect/ self-cleaning surfaces - Less area/ contact points for settling organisms	Marmur (2006a, 2006b), Ou et al. (2004); Ou and Rothstein (2005); Derek et al. (2004); Hwang and Song (2008); Troung et al. (2012); Wu et al. (2013)
- Drag reduction	- Reduction of surface drag by streaming the longitudinal and cross flows - Reduction of wall shear stress	Goldstein and Tuan (1998); Bechert et al. (2000a, 2000b); Friedmann (2010a, 2010b); Carlborg and Wijngaart (2011)
Fluid dynamics on surfaces - Macrohydrodynamics	- Pipe flow/ open water flow - High flow velocity to washout accumulated fouling	Köhler et al. (1999); Qian et al. (1999); Schultz et al. (2000); Horn et al. (2003); Granhag et al. (2004); Crimaldi et al. (2007)
- Microhydrodynamics	- unbounded flow - Flow around artificial microswimmers	Purcell (1977); Shapere and Wilczek (1989); Ramia et al. (1993); Najafi and Golestanian (2004); Avron et al. (2005); Lauga (2007)
	- bounded flow - Controlled hydrodynamics around microorganisms - dynamic stability of microorganisms/ artificial microswimmers	Vigeant et al. (2002); Cosson et al. (2003); Lauga et al. (2006); Hill et al. (2007); Berke et al. (2008); Zilman et al. (2008); Drescher et al. (2009); Evans and Lauga (2010); Or et al. (2011); Halder et al. (2013, 2014)

2.6.1 Biofilms under different hydrodynamic conditions

One major stream is investigating biofilms, the core element of biofouling and the ambient fluid flow conditions. It includes the investigation of biofilm material properties, geometric characteristics and the development processes on any submersed surface/ membranes. The physical properties of biofilms give idea of how to reduce their growth and detachment. Thus the biofilms related researches were also aimed to investigate the potential of using hydrodynamic forces (ie the development of critical shear stress) to detach biofilms and thus to control biofouling.

Picioreanu et al. (2001) studied the influence of biofilms geometrical characteristics (eg roughness, compactness, or area enlargement) on substrate (growth-limiting nutrients) mass transfer and conversion rates. They used a spatially two-dimensional model to compute laminar fluid flow, substrate mass transport, and conversion in irregularly shaped biofilms. This study was important to understand the biofilm development and substrate utilization rate from hydrodynamic point of view. The research works by Stoodley et al. (1998, 1999, 2001b and 2002) and Taherzadeh et al. (2010) on biofilm streamer showed special characteristics of biofilm in the context of drag reduction. According to them, the oscillation property of the micro-streamer is a key process for biofilms to survive in a fast flow environment and to grow up depending on substrate supply. Horn et al. (2003) studied the influence of hydrodynamic conditions on growth and detachment of biofilms using a Plexiglass (PMMA) made tube reactor. One major finding of their study was that the amount of detached biomass depends mainly on the biofilm thickness and the applied shear rates before the detachment event. Bol et al. (2009) used three-dimensional (3D) finite element model to simulate biofilm detachment. They reconstructed 3D biofilm geometries from stacks of 2D confocal laser scanning microscopy (CLSM) images. They also used a staggered fluid–structure interaction (FSI) approach to realize the interaction between the 3D biofilm structure and the ambient fluid. They found that the biomass detachment in real biofilm systems may solely be explicable by physical (ie mechanical) mechanism. They also mentioned that their detachment model was strongly dependent on physical/mechanical parameters, such as the mechanical strength of the biofilm matrix, Young's modulus, Reynolds number (*Re*) and biofilm structure. Picioreanu et al. (2009) used 3D computational model that couples fluid dynamics, solute transport and biofouling by biofilm formation in reverse osmosis (RO) and nanofiltration (NF) membrane modules. They found that the biomass accumulation in the feed channel of spiral-wound nanofiltration and reverse osmosis membrane devices, strongly affected the feed channel pressure drop, liquid velocity distribution and residence time distribution.

All the above studies showed that the hydrodynamics around biofilms plays a key role in the development, attachment and detachment of biofilms. The general objective of these studies was to control biofouling by applying high shear force by means of high fluid velocity. The detachment of biofilms in a high shear force may seem efficient from a broad point of view, but could not eliminate biofouling, rather in some cases may worsen the scenarios.

2.6.2 Biomimetic surfaces and underwater superhydrophobicity

Another major stream of AF research is focused on developing antifouling surface with superhydrophobicity, an idea generated from studying different biological surfaces those have the antifouling capabilities due to their hierarchical roughness. Lotus leaf, shark skin, water fern, water strider are some common examples of having natural superhydrophobic surfaces. Researchers have developed many synthetic surfaces mimicking the microtopogarphical arrangements of the exterior of the organisms, such as shark skin, lotus leaf, the body surfaces of different benthic invertebrates (eg blue mussels, edible crabs, the egg-cases of the lesser-spotted dogfish, brittle stars), in order to replace metal-based antifouling coatings on underwater structures (Petronis et al. 2000; Bechert et al. 2000b; Bers and Wahl 2004; Patankar 2004; Schumacher et al. 2008; Bhushan and Jung 2011). A few studies (Marmur 2006a, 2006b) also investigated the potentials of underwater superhydrophobicity (UWSH) with hierarchical microstructures inspired by natural AF surfaces. The idea of UWSH came from the air entrapment (plastrons) inside the grooves of the microstructure and to reduce the contact point and surface accessibility for the settling microorganisms on them (Wu et al. 2013). It also conveys the notion of developing effective velocity slips over those grooves (recirculating fluid particles inside the depressed regions) or air entrapped zones (Ou et al. 2004; Ou and Rothstein 2005; Derek et al. 2004; Hwang and Song 2008). However, some studies (eg Poetes et al. 2010) considered that the limited underwater plastron stability would reduce its scope for commercial applications.

The use of prefabricated patterned surface (ie surface textures at micro-scale) as an AF surface was limited in early days due to its complicated prefabrication processes. Andersson et al. (1999) developed textured surface by molding the Polydimethylsiloxane (PDMS) elastomer against the stainless steel mesh structures and obtained microstructures on scales of 43 and 77 µm. The developed microstructures were qualitatively uniform throughout the grid patterned surfaces. However, these imprinted silicone elastomer based mesh structures demonstrated that such a structure can significantly reduce fouling of barnacles (*Balanus improvisus*). Later on, using sophisticated photolithography technique, Petronis et al. (2000) developed precisely uniform patterns with predefined shape features and showed that PDMS made riblets with height 69 µm and base width 97 µm were most effective in reducing barnacle settlement. They also found that riblets were more effective than pyramids used in microtopographic feature. It has also been suggested that the investigated microtopographies might influence surface-near fluid dynamics and thus prevent settlement of any organisms. Bechert et al. (2000b) developed synthetic shark skin (3D riblets) and tested for drag reduction in a wind tunnel and in an oil channel. They found around 7.3% decreased turbulent shear stress, as compared to a smooth reference plate. Bers and Wahl (2004) replicated microtopographies (<500 µm) of four different marine organisms named: *C. pagurus*, *M. edulis*, *S. canicula* and *O. texturata* and found transitory antifouling properties of these surface microtopographies. Patankar (2004) proposed double-structured roughness to mimic the microstructure of superhydrophobic leaves (eg lotus leaf). He did the theoretical analysis of his proposed surfaces and showed that the double (or multiple) roughness structures or slender pillars are appropriate surface geometries to develop ‘self-cleaning’ surfaces. Though the artificial surfaces with biomimetic microstructures tend to show transitory fouling resistance the question still arises whether the transitory AF characteristics of artificial surfaces are due to the biological responses of microorganisms towards the surface or are following other physical laws.

The precise mechanism by which man-made microtopographies inhibit the settlement and colonisation of microorganisms is still unclear. Researchers have developed different hypotheses on this question and correlated different physical parameters (eg wettability, surface tension, feature sizes, and shapes) with the settlement process. Callow et al. (2002) suggested that the settlement of algal spores (*Ulva* syn. *Enteromorpha*) on a surface can be controlled by surface topography and surface tension. They reported that the shape and scale of features on a surface determine where spores will colonise. Scardino et al. (2006, 2008) presented an attachment point theory based on the size of the settling larvae/spores and the wavelength of the microtexture. Moreover, microorganisms (diatom cells in their study) attached in significantly higher numbers on surfaces where the number of attachment points was the highest, thus reduced numbers of attachment points resulted in lower attachment. Chung et al. (2007) suggested that the protruding features of the surface topography provided a physical obstacle to deter the expansion of small clusters of bacteria, present in the recesses, into microcolonies. Schumacher et al. (2008) developed a synthetic shark skin type patterned surface (Sharklet^{TM}) which showed excellent antifouling properties and hydrophobicity. They introduced the concept of nanoforce gradients based on the lateral force required to cause a 10% end deflection of microstructures in a patterned surface (ie in Sharklet^{TM}). They hypothesised that variations in topographic feature geometry will induce stress gradients within the lateral plane of the cell membrane of a settling cell during initial contact. They also introduced a new roughness index, named Engineered Roughness Index (ERI) to correlate the roughness pattern with its fouling removal efficiency. According to them, the predefined and periodic surface structure will exert a differential tension across the body (or sensing foot) of the settling organism resulting in a thermodynamically unstable surface (Schumacher 2007c). Bhushan and Jung (2011) developed many biomimetic artificial surfaces (hierarchical structures) with dimensions of features ranging from the macroscale to the nanoscale and tested their potentials on superhydrophobicity, self-cleaning, low adhesion, and drag reduction. Carl et al. (2012) demonstrated that wettability has a negligible effect on settlement of pediveligers of the mussel *Mytilus galloprovincialis*. Instead, the presence of topographic structures plays a key role in the settlement of mussels (Carl et al. 2012; Vucko et al. 2013).

In the meantime, the possibility of UWSH with microstructured surfaces was analysed theoretically by Marmur (2006b). He showed that UWSH is, in principle, feasible, and may be thermodynamically stable. However, he also suggested that the degree of superhydrophobicity depends on high roughness ratio of rough surface that keeps the water surface as close as possible to the tops of the roughness asperities. Recent experiments by Truong et al. (2012) and Wu et al. (2013) suggested that the plastron (ie the thin air film separating the substrate from the water in the superhydrophobic state) inside the grooves of microstructures, the primary mechanism of UWSH, is actually led to the reduction of attachment points and surface accessibility for the settling microorganisms. On the other hand, Poetes et al. (2010) stated that the UWSH is thermodynamically metastable. They showed that the plastron life depends on the internal vapour pressure of the gases in the plastron and the hydrostatic pressure which increases with fluid depth. At higher depths, the plastrons are more susceptible to exponential increase of diffusion into water. Thus they concluded the limited underwater plastron stability restricts the development of UWSH and their scope for commercial applications as antifouling surfaces.

From all these studies described above it is evident that the deterrent effects of synthetic patterned surfaces on certain fouling organisms decrease over time of exposure. The potential of AF surfaces with the idea of UWSH is also limited. Here, it should be noted that the biological surfaces inhibit fouling by an integrated defence mechanism that includes chemical, mechanical or physical defences, which may be found singly or in combination (Wahl 1989; Wahl and Lafargue 1990). In contrast to synthetic AF surfaces, these natural surfaces have additional defence mechanisms such as moulting, burrowing and aspects of surface chemistry (eg enzymes), which may combine with repellent surface microtopographies to form a multiple defence system (Thomason et al. 1994; Wahl 1997; Wahl et al. 1998; Bers and Wahl 2004).

In brief, the synthetic biomimetic surfaces show only a transitory fouling resistance capability so far and must undergo intense investigation before their commercial applications.

2.6.3 Fluid dynamics on different surfaces and microswimmers

Studying the fluid dynamics on different surfaces (plain/pattern) has many scientific interests and applications. For example, drag reduction in oil transport and in other vehicles like water vessels, automobiles and aeroplanes have been studied intensively using numerical calculation and experiments (Goldstein and Tuan 1998; Bechert et al. 2000a; Friedmann 2010a; Carlborg and Wijngaart 2011). On the other hand, the study of fluid dynamics received little attention in relation to the biofouling control. Though different studies showed that the swimming kinematics and trajectories of many microorganisms are altered by the presence of nearby boundaries, be they solid or deformable (Lauga et al. 2006; Berke et al. 2008; Drescher et al. 2009; Evans and Lauga 2010; Or et al. 2011; Samson 2010), the importance of analysing the microfluidic environment on microtopographies and related settlement behaviour of microorganisms were not addressed distinctly. One major reason could be the oversimplification of microhydrodynamics near to the surface and around self-propelled microorganisms considering insignificant convections within viscous sublayer. The swimming activities of microorganisms take place at extremely low Reynolds numbers, a regime in which fluid motion is dominated by viscous dissipation. Now the questions arise: will the swimming activities remain the same over patterned surfaces in comparison to a plain surface? Is there any effect of convection on the locomotion of self-propelled microorganisms when the flow condition itself is dynamic rather than static? What are the solid surface boundary effects on the dynamic stability of microorganisms? One major objective of this research is to find out the answers of these questions.

The presence of solid boundaries has profound effects on the dynamics and trajectories of near-surface microorganisms. The swimming dynamics of microorganisms are highly dependent on hydrodynamic interactions, either between immersed cells (group locomotion), or between cells and a surface (boundary effects). For example, the complex circular swimming of *E. coli* (*Re* ~10^{-4}) could be explained by the hydrodynamic interactions between the bacterial cell surface and solid boundaries (Lauga et al. 2006). Vigeant et al. (2002) and Lauga et al. (2006) showed that near a flat surface in a quiescent environment, conditions of forcefree and torque-free swimming result in hydrodynamic trapping of motile *E. coli*. Cosson et al. (2003) and Berke et al. (2008) demonstrated how spermatozoa and *E. coli* become attached to solid surfaces that confine their domain. Hill et al. (2007) showed that hydrodynamic surface interactions enable *E. coli* to seek efficient routes to swim upstream. Zilman et al. (2008) studied the mechanisms of larval contact in two-dimensional Couette (linear shear flow near flat solid boundaries) and Poiseuille (laminar flow in a tube) flows. Drescher et al. (2009) investigated the waltzing dynamics of *Volvox* (a spherical alga) when placed next to a solid surface, where pairs of cells attract one another and can form stable hydrodynamic bound states. Evans and Lauga (2010) showed that the presence of a wall can lead to a change in the waveform expressed by a beating flagellum, which in turn results in an increase or decrease in its propulsive force depending on the type of oscillation. Or et al. (2011) investigated how a plain boundary affected the dynamic stability of low Reynolds number swimmers from the viewpoint of dynamic systems and control theory. However, most of these studies considered only plain surfaces, and did not study any patterned surfaces.

The above mentioned studies indicated that boundary-surface effects on motility of microorganisms lead to varied and important consequences in biological systems. For example, *E. coli* cells are observed to change their swimming trajectories from straight to circular when they are moving parallel to a solid surface (Lauga et al. 2006; Crowdy et al. 2010) or their initial settlement on boundary-surface could be affected by microtopographies (Halder et al. 2013). The study of colonization of microorganisms on plain/irregular surfaces has also received considerable attention in the past, but mostly in macrohydrodynamics. Köhler et al. (1999) studied colonization pattern of different microorganisms, such as *Mytilus edulis, Polydora dliata, Balanus improvisus,* diatoms, hydrozoa, bryozoa, and several ciliates, on prefabricated rough surfaces in the natural flow environment of Baltic Sea. They found that the surface roughness significantly influenced the recruitment pattern of sessile organisms. However, their investigation took place in macrohydrodynamic environment and on macro-scale roughness (0.1-5 mm glass beads on 5 cm × 5 cm smooth glass plates). They concluded that the coarse surface rugosities, as used in their studies, were not sufficient to inhibit the settlement of microorganisms. Instead, abundance of most species investigated was generally higher on rough surfaces than on smooth surfaces. Macrohydrodynamics on plain/irregular surfaces and related settlement of microorganisms were also investigated by Qian et al. (1999), Schultz et al. (2000), Horn et al. (2003), Granhag et al. (2004), Crimaldi et al. (2007). For example, Qian et al. (1999) worked with macrofouling in a unidirectional flow system (pipe flows). Their objective was to determine the influence of hydrodynamics and surface properties of the substratum on larval attachment in pipes by three cosmopolitan fouling organisms: the tube-building polychaete *Hydroides elegans*, the bryozoan *Bugula neritina* and the barnacle *Balanus amphitrite*. They found that the larval settlement was influenced strongly by the chemical characteristics of the substratum and the applied flow rate. They did not investigate the composition of the microbial film on surfaces and, thus, could not determine if there were differences in the species compositions of the biofilms found on surfaces of different tubes. However, they addressed the importance of studying composition of biofilm and its change over time, as well as its influence on larval settlement.

The investigation on microhydrodynamics is relatively new compared to the conventional pipe flow experiments of macrohydrodynamics. Since last decade, a number of researchers started working with fine-scale microtopographies and found AF efficacy of these surfaces (eg Petronis et al. 2000; Bers and Wahl 2004; Scardino et al 2006; Schumacher et al. 2007b; Carl et al. 2012). Most of these studies considered either the static flow conditions or the unspecified flow conditions of natural marine environment. In some other cases, researchers investigated the swimming dynamics of model microswimmers in the unbounded (ie far away from any boundary surface) low Reynolds number flows (eg Najafi and Golestanian 2004; Avron et al. 2005). With the advancement of relevant software (eg Computational Fluid Dynamics (CFD) software, auto-focusing multi-time imaging software) and logistic supports (eg high resolution 3D printer, precision mask fabrication with laser device, digital in-line holographic microscopy (DIHM)), researchers started considering microhydrodynamics on irregular/ patterned surfaces and its relation with the locomotion of microorganisms.

2.6.4 Locomotion of microorganisms and microfluidic analysis

The locomotion of small microorganisms has been of interest to fluid dynamicists and biologists for many years. Most of the studies investigated the locomotion of microorganisms on a plain surface in a quiescent fluid environment (eg Vigeant et al. 2002; Lauga et al. 2006; Hill et al. 2007; Lauga and Power 2009; Evans and Lauga 2010) and in unbounded flow regime (eg Ramia et al. 1993; Lauga 2007). Some early works on swimming dynamics of simple model microswimmers in an unbounded low Reynolds number flow (eg Purcell 1977; Shapere and Wilczek 1989) gave the fundamental guidelines for studying the self-propulsion organisms. The main interest of these studies was to explain the methods of propulsion of artificial swimmers through low *Re* fluids. For example, Purcell (1977), in his famous talk on ‘Life at low Reynolds numbers’, illustrated a remarkably simple swimmer containing two hinges only which has been later widely known as ‘Purcell’s swimmers’ (Figure 2.10). He also presented the ‘Scallop theorem’ which states that the swimming strategy of a scallop with only one hinge (one degree of freedom), is futile at low *Re* fluid. He mentioned that at low *Re*, the reciprocal swimming motion (ie changing body into a certain shape and then going back to the original shape, following the same sequence in reverse) is of no use and independent of time (ie it makes no difference how fast or slow the shape changes).

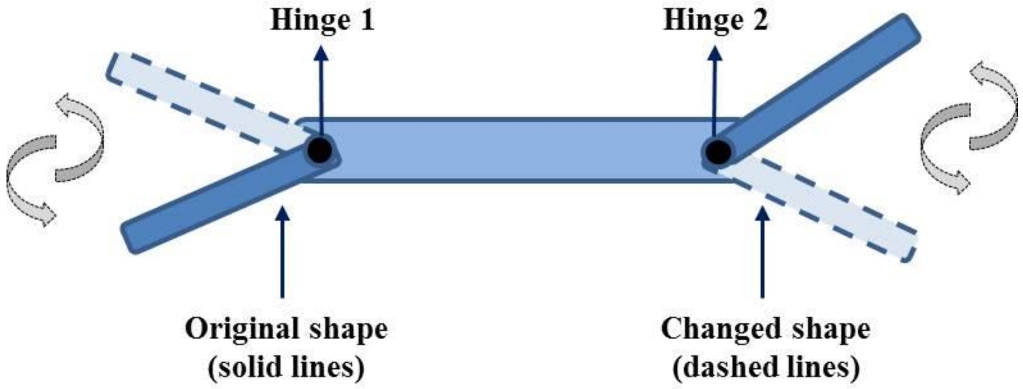

Figure 2.10: Schematic diagram of Purcell’s two-hinge swimmer changing its shape (dashed lines) while swimming. The shape change must be in a nonreciprocal way to get a net motion.

At low *Re* and in Newtonian fluids, a swimmer must deform in a nonreciprocal way in order to generate net motion which requires at least two degrees of freedom (ie two hinges) in the configuration space. Due to the complex interaction between the motion of the fluid and the body, this nonreciprocal way of swimming has been studied theoretically under several simplifications. One approach focuses on axisymmetric swimmers, whose motion is only one-dimensional along the axis of symmetry. Shapere and Wilczek (1989) gave a general kinematic framework for describing the self-propulsion of a cylindrical shape object with varying cross-sections at low *Re* fluid. Najafi and Golestanian (2004) presented a very simple and experimentally accessible model system based on the original non-reciprocal motion related idea of Purcell (1977). Their proposed model could swim forward using periodic internal motions. The swimmer consisted of three hard spheres that were linked through two arms (Figure 2.11), and had the advantage that the details of the hydrodynamic interactions, as well as the swimming velocity and direction, could be worked out with great ease, as compared to the case of the Purcell’s swimmer.

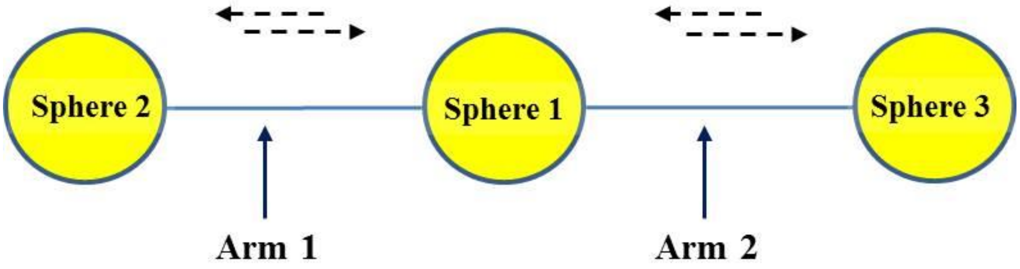

Figure 2.11: A model swimmer proposed by Najafi and Golestanian (2004) based on Purcell's original idea of two-hinge swimmer. The proposed swimmer has three linked spheres connected by two rigid arms of negligible thickness. The arm lengths can increase/ decrease in order to produce a nonreciprocal motion.

Avron et al. (2005) presented another artificial swimmer, made of two spherical bladders that exchange volumes and mutual distance of the bladders in each stroke. He also showed that the modelled microswimmer (a pair of spherical bladders) is superior to other models of artificial swimmers, such as three linked spheres by Najafi and Golestanian (2004) or two-hinge swimmer by Purcell (1977), at low Reynolds numbers. All these studies delineated the swimming mechanism of the artificial microswimmers which evidently support researchers to characterize the swimming behaviour of different living organisms (eg bacteria, larva) in the microscopic world, where viscosity dominates. One major drawback of the unbounded flow analysis is that the unbounded flow neither considers the boundary effects, nor the hydrodynamic interactions of other nearby bodies. In reality, however, the swimming events and the settlement of microorganisms take place typically close to other submerged bodies or solid boundaries. Hence the study of locomotion of microorganisms in an unbounded flow condition is far apart from reality.

Microorganisms, swimming within fluids of non-negligible kinematic viscosity, are subjected to very small length scales and speeds. The Reynolds number (*Re*) associated with this locomotion is therefore very small. For example, *Re* for *E. coli* in a static fluid due to its own motion is $\sim 10^{-4}$ while that of a spermatozoan is $\sim 10^{-2}$. The inertial forces are negligible in these cases in comparison to the viscous effects of the fluid. When the swimming events take place very near to the plain boundary surface in a static fluid condition, where the viscosity effect is the strongest, microorganisms get negligible external forces from surrounding fluid particles. On the other hand, microorganisms moving over patterned surfaces in a static/dynamic fluid flow conditions are still indistinct and require intense investigation. The current study is aimed to investigate a few such issues of scientific interest, for instance, the periodic surface roughness, the associated fluid flow environment, fluid-surface interactions, and the relevant changes in the swimming trajectories of microorganisms.

2.7 Conclusion

The study of microfluidic environment around microorganisms needs to take into account the hydrodynamic interactions between swimmers' bodies and the surface boundaries. The surface boundaries may have different forms and shape patterns based on interest of application/investigation (eg plain surface, irregular pattern surface, or regular patterned surface, ie a surface with predefined microtopographies). The fluid flow conditions over these surfaces could also be either static or dynamic. Both the boundary surface pattern and the fluid flow conditions are significantly important in the investigation of swimming dynamics of microorganisms. Here, it should be noted that microorganisms swim generally by producing a cyclic distortion of the body shape and by the coordinated use of their cilia and flagella (Stone and Samuel 1996; Lauga and Powers 2009). The ambient flow conditions and hydrodynamic interactions between cell bodies and solid boundaries play important roles in maintaining the dynamic stability of microorganisms while swimming, and actively selecting surfaces for their settlement. The nature of the surface pattern, the associated microfluidic environment, and the swimming depths of microorganisms are considered key factors for the changes in the locomotion of microorganisms. As the dynamic stability of microorganisms is considered an important criterion for their surface selection preferences, the parameters regulating it are also important in relation to their initial settlement process. Hence, this study investigated the surface patterns, the associated microhydrodynamics and the swimming dynamics of microorganisms over surfaces. However, the microhydrodynamic conditions around moving microorganisms are believed to be complex, especially where the nearby solid boundaries are deformed/ patterned. In this situation, a numerical study using advanced computer software is more suitable approach than finding an exact analytical solution for the hydrodynamics. In this study, a CFD method has been applied for the investigation of microhydrodynamics around moving microorganisms over plain/patterned surfaces. The following chapter (Chapter 3) will describe the theoretical background of the CFD method used in this study.

Chapter 3

3 Numerical analysis to microfluidic environment around microorganisms

3.1 Introduction

The literature review presented in Chapter 2 specified that the investigation of the microfluidic environment around microorganisms is very important in order to understand the mechanism of transitory AF nature of some microstructure-based pattern surfaces. It has been hypothesized that the surface-near microfluidic environment plays an important role in the initial settlement process of some microorganisms and thus also significantly affect the overall biofouling development process at later stage. The microhydrodynamic conditions around moving microorganisms are also believed to be complex, especially where the nearby solid boundaries are deformed/ patterned instead of a plain surface. It is very difficult to get an analytical solution of this nature. A numerical approach is better suitable to capture the complex scenarios and fluctuating microhydrodynamic conditions with the aid of advanced Computational Fluid Dynamics (CFD) software. CFD is the analysis of systems involving fluid flow, heat transfer and associated phenomena (eg chemical reactions, combustion) by means of computer-based simulation (Versteeg and Malalasekera 2007). CFD codes are structured around the numerical algorithms that can analyse complex fluid flow problems. Hence, in this study, a finite volume based numerical approach has been taken to analyse the microfluidic environment around microorganisms over surfaces.

3.2 Numerical Solution approach

Analytical solutions to the Navier-Stokes equations exist only for the simplest flows under ideal conditions. To obtain solutions for the real flows, a numerical approach must be adopted whereby the equations are replaced by algebraic approximations which may be solved using a powerful CFD solvers. A commercially available CFD solver, ANSYS CFX (Version 14.5, ANSYS Inc., Canonsburg, PA, USA) has been used in this study which follows the finite volume method to solve the Navier-Stokes equations.

3.2.1 CFD solution technique

There are three distinct streams of numerical solution technique: Finite difference, finite element and spectral methods. The finite volume method is a special finite difference formulation technique being used by most of the well-established CFD software. ANSYS CFX software also uses this finite volume method which essentially generates polyhedral finite volumes surrounding the vertices of the underlying mesh elements (eg 3D elements: hexahedrons, tetrahedrons, prisms and pyramids). The numerical algorithm consists of the following steps:

1. integration of the governing equations (in a form of partial differential equations) of fluid flow over all the (finite) control volumes (CVs) of the domain. This is equivalent to applying a basic conservation law to each CV.
2. discretisation- conversion of the resulting integral equations into a system of algebraic equations by generating a set of approximations for the terms in the integral equations.
3. solution of the algebraic equations by an iterative method.

In an element base finite volume method, as used by CFX, it involves discretising the spatial domain into a number of meshes. Meshes are used to construct finite volumes or CVs, which are used to conserve relevant quantities such as mass, momentum, and energy. The development of CVs is the first step of the finite volume method. The next step is to integrate the governing equations of fluid flow over all the CVs. The governing equations of fluid flow represent the mathematical statements of the conservation laws of physics.

For a typical 2D mesh, all solution variables (eg velocities, pressure) and fluid properties (eg density, viscosity) are stored at the nodes (mesh vertices). A CV is constructed (Figure 3.1) around each mesh node using the median dual (defined by the lines joining the centres of the edges and the element centres surrounding the node).

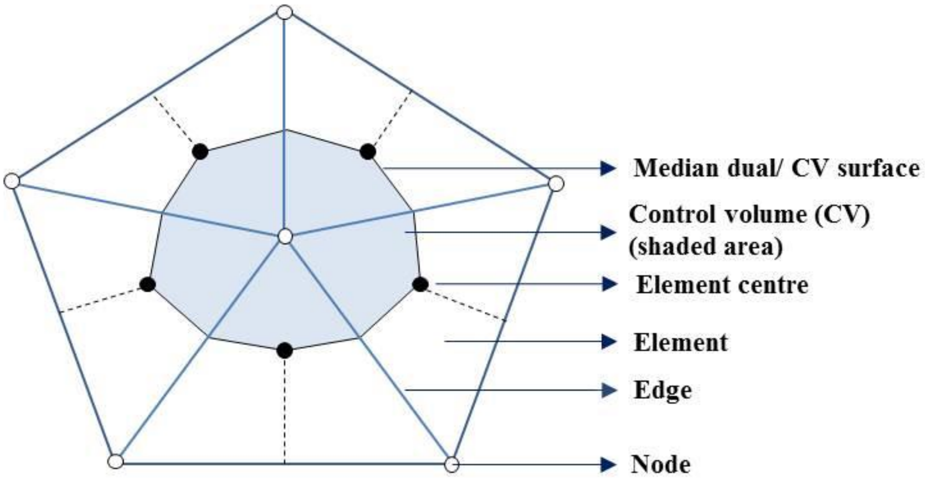

Figure 3.1: Control volume (CV) generation from mesh elements (Source: reproduced from ANSYS CFX documentation 2011).

At these CVs, the conservation laws of physics must be met as follows:

1. the mass of a fluid is conserved (continuity equation)
2. the rate of change of momentum equals the sum of the forces on a fluid particle (momentum equation/ Newton's second law)
3. the rate of change of energy is equal to the sum of the rate of heat addition to and the rate of work done on a fluid particle (energy equation/ first law of thermodynamics)

As this study did not consider any heat transfer or internal (thermal) energy, the energy equation will not be described further. All the fluid properties are functions of space co-ordinates and time, and hence can be written as $\rho(x, y, z, t), P(x, y, z, t), T(x, y, z, t),$ and $U(x, y, z, t)$ for the density, pressure, temperature and the velocity vector, respectively. The derivatives of fluid properties can also be expressed following the same practice (eg x-derivative of P is $\frac{\partial P}{\partial x}$). At CVs, the above mentioned equations which govern the time dependent 3D fluid flow and heat transfer of a Newtonian fluid can be described as follows, starting with the continuity equation:

$$\frac{\partial \rho}{\partial t} + div(\rho \boldsymbol{U}) = 0 \tag{3.1}$$

where $div\ \boldsymbol{U} = \frac{\partial u}{\partial x} + \frac{\partial v}{\partial y} + \frac{\partial w}{\partial z}$, and $\boldsymbol{U}$ is the velocity vector described as $\boldsymbol{U}(u\boldsymbol{i}, v\boldsymbol{j}, w\boldsymbol{k}, t)$. Here, u, v and w are the velocity components in the x ($\boldsymbol{i}$= $longitudinal$), y ($\boldsymbol{j} = lateral$) and z ($\boldsymbol{k} = vertical$) directions, respectively). Equation (3.1) is the continuity or mass conservation equation. The three components of the momentum equation can be written as:

x-momentum: $$\frac{\partial}{\partial t}(\rho u) + div\ (\rho u \boldsymbol{U}) = -\frac{\partial P}{\partial x} + div(\mu\ grad\ u) + S_{Mx} \tag{3.2}$$

where $div(\mu\ grad\ u) = \frac{\partial}{\partial x}\left(\mu \frac{\partial u}{\partial x}\right) + \frac{\partial}{\partial y}\left(\mu \frac{\partial v}{\partial y}\right) + \frac{\partial}{\partial z}\left(\mu \frac{\partial w}{\partial z}\right)$ and S_{Mx} is the momentum source in the x-direction. The dynamic viscosity of the fluid is μ, which relates viscous stresses to linear deformations (eg linear elongating deformation components $\frac{\partial u}{\partial x}$, $\frac{\partial v}{\partial y}$, $\frac{\partial w}{\partial w}$). Here, it should be noted that, in a Newtonian fluid the viscous stresses are proportional to the rates of deformation. The deformation components will be discussed further in Chapter 5. The two other momentum components can be written as

y-momentum: $$\frac{\partial}{\partial t}(\rho v) + div\ (\rho v \boldsymbol{U}) = -\frac{\partial P}{\partial y} + div(\mu\ grad\ v) + S_{My} \tag{3.3}$$

and,

z-momentum: $$\frac{\partial}{\partial t}(\rho w) + div\ (\rho w \boldsymbol{U}) = -\frac{\partial P}{\partial z} + div(\mu\ grad\ w) + S_{Mz} \tag{3.4}$$

Here, Equations (3.1-3.4) are the Navier-Stokes equations written in the most useful form for the development of finite volume method.

To describe finite volume method further, a transport equation with a general variable (φ) will be introduced in the conservative form:

$$\frac{\partial}{\partial t}(\rho\varphi) + div(\rho\varphi\boldsymbol{U}) = div(\Gamma\ grad\ \varphi) + S_{\varphi} \tag{3.5}$$

where μ is the fluid viscosity, Γ is the diffusion coefficient, and the source term in this equation is S_φ. Equation 3.5 is the so-called transport equation for property φ, where setting φ equal to 1, u, v, w and selecting appropriate values for diffusion coefficient Γ and source terms, one can obtain Equations (3.1-3.4) respectively.

Physically Equation (3.5) highlights the various transport processes, such as convection/ advection, diffusion and source momentum. Each of the term of this equation will be discussed individually later in this chapter.

3.3 Integration of the governing equations

Equation (3.5) is used as the starting point for computational procedures in the finite volume method and the first step here is the integration of this equation. When the integration of Equation (3.5) over a CV takes place, and Gauss's divergence theorem is applied to convert volume integrals involving divergence (div) and gradient operators ($grad$) to surface integrals, Equation (3.5) becomes

$$\underbrace{\frac{d}{dt}\left(\int_V \rho\varphi dV\right)}_{Transient} + \underbrace{\int_A \boldsymbol{n}.(\rho\varphi\boldsymbol{U})dA}_{Advection} = \underbrace{\int_A \boldsymbol{n}.(\Gamma \,\mathrm{grad}\, \varphi)dA}_{Diffusion} + \underbrace{\int_V S_\varphi dV}_{Source} \tag{3.6}$$

where, the Gauss's divergence theorem states that for a vector *a*

$$\int_V div(\boldsymbol{a})dV = \int_A \boldsymbol{n}.\boldsymbol{a}dA \tag{3.7}$$

where $\boldsymbol{n}.\boldsymbol{a}$ is the component of vector $\boldsymbol{a}$ in the direction of the vector $\boldsymbol{n}$ normal to the surface element dA. Thus, the integral of the divergence of a vector $\boldsymbol{a}$ over a volume is equal to the component of $\boldsymbol{a}$ in the direction normal to the surface which bounds the volume integrated over the entire bounding surface A.

In Equation (3.6), $\int_V$ and $\int_A$ denote volume and surface integrals, respectively. The volume integrals represent sources or accumulation terms, and the surface integrals represent the summation of the fluxes. The left most term of Equation (3.6) states the rate of change of the total amount of fluid property φ in the CV and designated as the transient term. The second term means the net rate of decrease of fluid property φ of the fluid element due to advection. Here the product $\boldsymbol{n}.(\rho\varphi\boldsymbol{U})dA$ expresses the flux component of property φ due to fluid flow along the outward normal surface vector $\boldsymbol{n}$, and termed as advective flux. The first term on the right hand side of Equation (3.6) is the diffusive term which indicates the net rate of increase of fluid property φ of the fluid element due to diffusion across the CV boundaries. It includes diffusive flux $\boldsymbol{n}.(\Gamma\,\mathrm{grad}\,\varphi)$ which is positive in the direction of a negative gradient of the fluid property φ. The right most term in Equation (3.6) is the source term which indicates the rate of increase of fluid property φ as a result of sources inside the fluid element/ CV. In words, Equation (3.6) can be expressed in words as follows:

Rate of increase of φ inside the CV	+	Rate of decrease of φ due to convection across CV faces	=	Rate of increase of φ due to diffusion across CV faces	+	Rate of generation of φ due to sources inside CV

In a time dependent problem (transient analysis), it is also necessary to integrate each term with respect to time t over a small interval Δt, for example, from (t) until $(t + \Delta t)$. So, the transport equation (Equation 3.6) can be re-written for a time-dependent process, as:

$$\int_t^{t+\Delta t} \frac{d}{dt}\left(\int_V \rho\varphi dV\right)dt + \int_t^{t+\Delta t}\left(\int_A \boldsymbol{n}.(\rho\varphi\boldsymbol{U})dAdt = \int_t^{t+\Delta t}\int_A \boldsymbol{n}.(\Gamma\, grad\ \varphi)dAdt + \int_t^{t+\Delta t}\int_V S_\varphi dVdt \qquad (3.8)$$

The next step of the finite volume method is to discretise the volume and surface integrals of Equation (3.6).

3.4 Discretization

The key step of the finite volume method is the integration of the governing equations over a CV to yield a discretised equation at its nodal point. Volume integrals are discretised within each element sector and accumulated to which the sector belongs. Surface integrals are discretised at the integration points (ip*n*, *n* = 1, 2, 3…) located at the centre of each surface segment within an element and then distributed to the adjacent control volumes. Figure 3.2 illustrates the integration points in a single 2D triangular element.

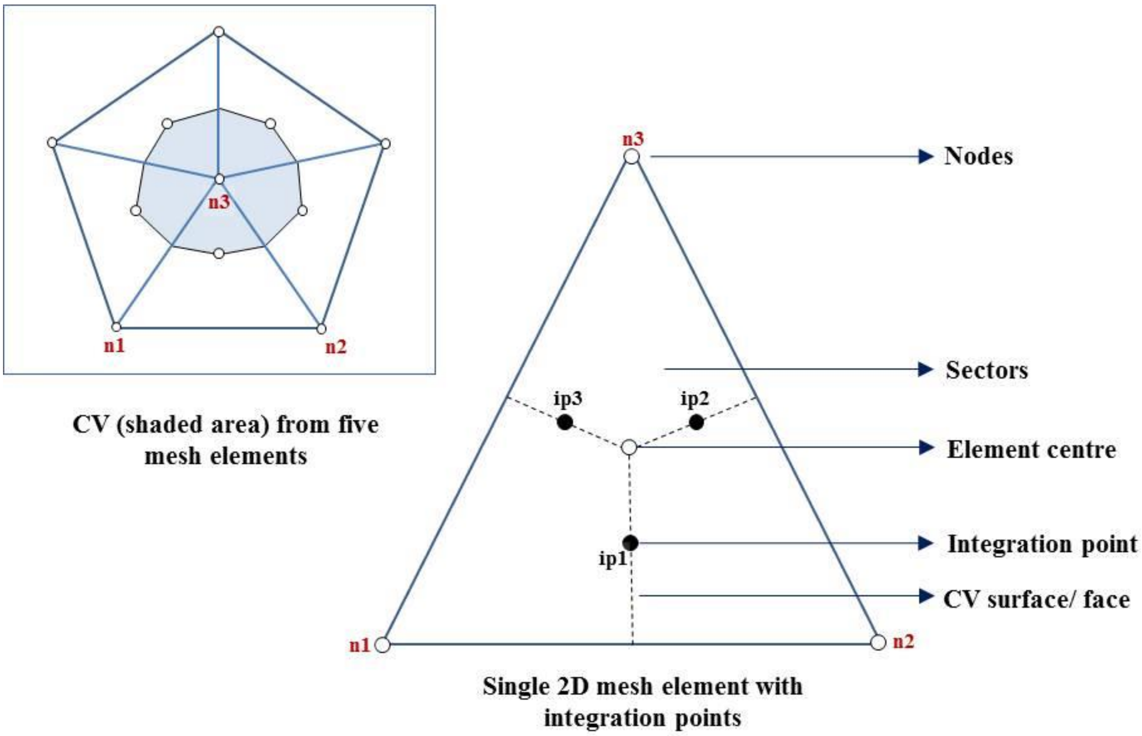

CV (shaded area) from five mesh elements

Single 2D mesh element with integration points

Figure 3.2: Integration points of a single 2D triangular element where the surface integrals are discretised. A CV surrounding a nodal point is also shown in the inset (Source: reproduced from ANSYS CFX documentation 2011).

As the surface integrals are equal and opposite for CVs adjacent to the integration points, the surface integrals are guaranteed to be locally conservative.

After discretising the volume and surface integrals, the integral equation (Equation 3.6) becomes

$$V\left(\frac{\rho\varphi-\rho^0\varphi^0}{\Delta t}\right)+\sum_{ip}\dot{m}_{ip}\varphi_{ip}=\sum_{ip}(\Gamma grad\ \varphi\Delta n)_{ip}+\overline{S_\varphi}V \qquad (3.9)$$

where $\dot{m}_{ip}=(\rho\boldsymbol{U}\Delta n)_{ip}$ is the discrete mass flow through a surface of CV, and V is the CV, Δt is the time step, Δn is the discrete outward surface vector. The subscript ip denotes evaluation at an integration point, summations ($\sum_{ip}$) are over all the integration points of the CV, and the superscript $(^{\circ})$ refers to the old time level. Here it should be noted that the first order backward Euler scheme has been assumed in Equations (3.9), although the second order scheme was used in this study for a transient analysis which will be described in the following discretization schemes section.

3.5 Properties of discretization schemes

Different schemes are needed to discretise all volume and surface integrals. The following sections will demonstrate different schemes used in this study for this discretization purpose. The discretization schemes must also fulfil some fundamental properties of numerical calculations, such as, conservativeness, boundedness, transportiveness and order accuracy. A detail description of these properties can also be found in Versteeg and Malalasekera (2007).

3.5.1 Conservativeness

The conservativeness of fluid property φ must be ensured throughout the discretization procedures. Physically it means that the flux of φ leaving a CV across a certain face must be equal to the flux of φ entering the adjacent CV through the same face. Consistency in flux expression in all adjacent CVs is highly needed for the conservativeness of φ in the whole solution domain. Inconsistent flux interpolation formulae give rise to unsuitable schemes that do not satisfy the overall conservation.

3.5.2 Boundedness

In most of the cases, the discretised equations are solved using an iterative numerical technique. This technique starts with the solution procedure using approximated value of φ and then performs successive updates until a converged solution is obtained. One desirable feature of this convergent iterative method is boundedness which states that the internal nodal values of fluid property φ should be bounded by its boundary values (ie remain within given boundary values) in the absence of sources. Another essential criterion for the boundedness property is that all coefficients of the discretised equations should have the same sign (usually positive). Physically it means that an increase in the variable φ at one node should result in an increase in φ at adjacent nodes. Without satisfying the boundedness property, the solution of discretised equations will contain wiggles/ oscillations.

3.5.3 Transportiveness

Transportiveness is the distribution of φ from nearby sources to a nodal point based on flow directionality and the magnitude of the Peclet number, Pe (ie the ratio of rate of advection to rate of diffusion). In the case of pure diffusion, when the fluid is stagnant ($Pe \rightarrow 0$), the diffusion process tends to spread φ in all direction from adjacent source points. Hence, the effect at a nodal point (ie the point of calculation) from the nearby points depends on their distances and diffusivity. On the other hand, at large values of Pe number, the influencing becomes increasingly biased towards the upstream direction of flow. Thus, the conditions at nodal point (ie the solution of variable φ) depends on the transportiveness of nearby sources of φ based on flow direction and Pe number. The discretization scheme needs to take into consideration of the directionality of influencing and magnitude of Pe number.

3.5.4 Order accuracy

The discretization schemes use different levels of order accuracy for the discrete approximations based on Taylor series truncation error. Increasing the order accuracy of an approximation generally implies that the truncation error is reduced more quickly by developing fine mesh following successive mesh refinement (grid independent) or by applying small time steps. However, high-order approximations (eg the QUICK scheme, third-order accurate) are numerically less stable and increases computational load.

3.6 Different discretization schemes and shape functions

3.6.1 Transient term

For CVs that do not deform in time (incompressible), the general discrete approximation of the transient term for the nth time step is:

$$\frac{\partial}{\partial t}\int_V \rho\varphi dV) \approx V\left(\frac{(\rho\varphi)^{n+\frac{1}{2}}-(\rho\varphi)^{n-\frac{1}{2}}}{\Delta t}\right) \tag{3.10}$$

where values at the start and end of the time assigned the superscripts $n-\frac{1}{2}$ and $n+\frac{1}{2}$, respectively. With the first order backward Euler scheme, the start and end of time step values are respectively approximated using the old (ie $n-\frac{1}{2} \approx {}^{\circ}$) and current time level solution values. The resulting discretization is

$$\frac{\partial}{\partial t}\int_{V} \rho\varphi dV) \approx V\left(\frac{\rho\varphi-(\rho\varphi)^{o}}{\Delta t}\right) \tag{3.11}$$

It is robust (ie numerically stable), fully implicit, bounded, and conservative in time and does not have a time step size limitation. This discretization is, however, only first order accurate in time and will introduce discretization errors that tend to diffuse steep temporal gradients. Hence, the second order backward Euler scheme in this study. This scheme approximated the start (old) and end (current) time step values as:

Start time step: $$(\rho\varphi)^{n-\frac{1}{2}} = (\rho\varphi)^{\mathrm{o}} + \frac{1}{2}((\rho\varphi)^{\mathrm{o}} - (\rho\varphi)^{\mathrm{oo}}) \tag{3.12}$$

End time step: $$(\rho\varphi)^{n+\frac{1}{2}} = (\rho\varphi) + \frac{1}{2}((\rho\varphi) - (\rho\varphi)^{\mathrm{o}}) \tag{3.13}$$

where the superscript (°) and (°°) refer to the immediate old time level and the next old time level data. When these values are substituted into the general discrete approximation (Equation 3.9), the resulting discretised equation is

$$\frac{\partial}{\partial t}\int_{V} \rho\varphi dV) \approx V\left(\frac{\frac{3}{2}(\rho\varphi)-2(\rho\varphi)^{o}+\frac{1}{2}(\rho\varphi)^{oo}}{\Delta t}\right) \tag{3.14}$$

This scheme is also robust, fully implicit, bounded, and conservative in time and does not have a time step size limitation. It is also second-order accurate in time and can be suitably used in the problem described in this study.

3.6.2 Advection term

The advection term requires the integration point values of φ (ie φ_{ip}) to be approximated in terms of the surrounding nodal values of φ. The advection scheme implemented in ANSYS CFX can be cast in the form

$$\varphi_{ip} = \varphi_{up} + \psi\nabla\varphi.\Delta\boldsymbol{r} \tag{3.15}$$

where φ_{up} is the value at the upwind node, and $\boldsymbol{r}$ is the vector from the upwind node to the ip integration point. CV gradient $\nabla\varphi$ can be defined as a form of the Gauss's divergence theorem

$$\nabla\varphi = \frac{1}{V}\sum_{ip}(\varphi\Delta\boldsymbol{n})_{ip} \tag{3.16}$$

where $\Delta\boldsymbol{n}$ is the outward surface vector at ip and φ to be evaluated at integration points using finite-element shape functions. The value of ψ function (ie flux limiter function) is determined by the ratio of upwind-side gradient to downwind-side gradient and hence the nature of the scheme. For example, the first order Upwind Difference Scheme (UDS) uses ψ=0. A value of ψ=1 yields the Central Difference scheme (CDS). The basic UDS is the most stable and unconditionally bounded scheme, but it introduces a high level of false diffusion due to its low order of accuracy (first-order). The CDS scheme, on the other hand, can give spurious 'wiggles' or oscillations in the solutions when the Pe number is high (Versteeg and Malalasekera 2007). A Total Variation Diminishing (TVD) scheme can address this problem which is specially formulated to achieve oscillation free solutions.

In this study, a High Resolution (HR) scheme, a special monotonicity preserving TVD scheme, has been used which sets a nonlinear recipe for ψ at each node. The ψ value in this scheme is computed to be as close to 1 as possible without introducing new wiggles. The advective flux is then evaluated using the values of ψ and $\nabla\varphi$ from the upwind node, where ψ value is based on the boundedness principles used by Barth and Jesperson (1989). The Barth and Jesperson scheme stated that the values of the reconstructed polynomial (φ_{ip}) within the CV should not exceed the maximum and minimum values (φ_{min} and φ_{max}) at the neighbours of the CV. This methodology involves first computing φ_{min} and φ_{max} at each node using a stencil (ie a model proposed by Barth and Jesperson 1989) involving adjacent nodes (including the node itself). Then the Equation (3.15) is solved for each integration point around the node so that the value of ψ does not undershoot φ_{min} or overshoot φ_{max}. The nodal value for ψ is taken to be the minimum value of all integration point values surrounding the node. The value of ψ is also not permitted to exceed 1. The Barth and Jesperson scheme is equivalent to the TVD-MUSCL scheme (ie Total Variation Diminishing - Monotonic Upstream-centered

Scheme for Conservation Laws) when applied to one-dimensional situations (Darwish and Moukalled 2003).

3.6.3 Diffusion term

Shape functions are used to evaluate spatial derivatives for all the diffusion terms. ANSYS CFX uses finite-element shape functions to approximate these derivatives or solution gradients at integration points (ip). Finite-element shape functions describe the variation of a variable φ varies within an element as follows:

$$\varphi = \sum_{i=1}^{N_{node}} N_i \varphi_i \tag{3.17}$$

where N_i is the shape function for node i, and φ_i is the value of φ at node i. The summation ($\sum_{i=1}^{N_{node}}$) is over all nodes of an element where $\sum_{i=1}^{N_{node}} N_i = 1$.

The shape functions used in ANSYS CFX are linear in terms of parametric coordinates (s, t, u). For example, for a tetrahedral element (as shown in Figure 3.3) the tri-linear shape functions for the nodes ($i = 1, 2, 3, 4$) are:

$$\left.\begin{aligned} N_1(s,t,u) &= 1 - s - t - u \\ N_2(s,t,u) &= s \\ N_3(s,t,u) &= t \\ N_4(s,t,u) &= u \end{aligned}\right\} \tag{3.18}$$

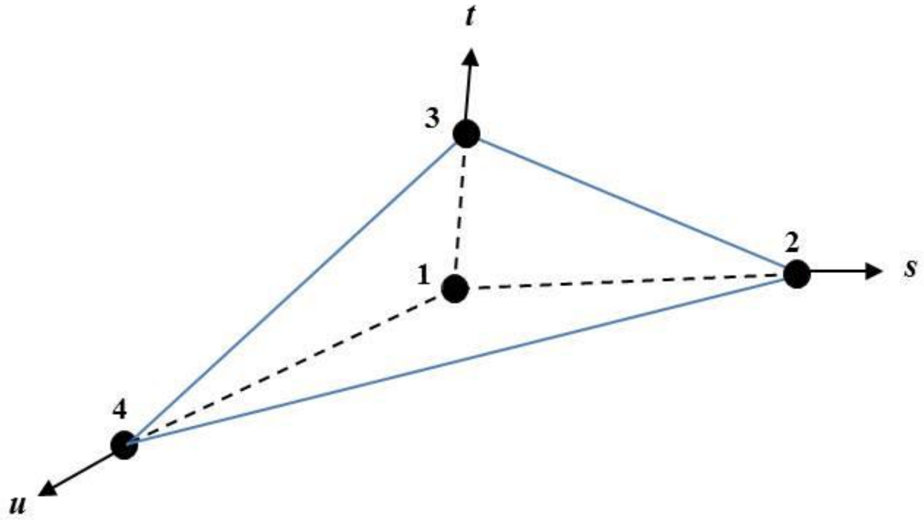

Figure 3.3: A tetrahedral element showing four nodal points in a parametric coordinate system (Source: reproduced from ANSYS CFX documentation 2011).

For a derivate in the x-direction at integration point ip:

$$\left.\frac{\partial \varphi}{\partial x}\right]_{ip} = \sum_n \left.\frac{\partial N_n}{\partial x}\right]_{ip} \varphi_n \tag{3.19}$$

The summation ($\sum_n$) is over all the shape functions for the element. The shape function gradients can be evaluated at the actual location of each integration point (true tri-linear interpolation), or at the location where each ip surface intersects the element edge (linear-linear interpolation). In this study, the linear-linear interpolation scheme was used for both pressure and velocity interpolations along with the parametric shape function option. The linear-linear scheme improves solution robustness, though it locally reduces the spatial order-accuracy of the discrete approximation.

3.6.4 Source term

Source term in Equation (3.6) is an additionally applied variable in the transport equation to a volume defined by a sub-domain or to a point within a domain. A point source is actually implemented as a volumetric source within a single domain element whose centre is the nearest to the point as specified within a domain. The source term can be a momentum source, bulk source or any general source in a scalar equation (eg the energy, turbulence or mass fraction equations). In this study, a general momentum source (as an immersed solid) has been used to model a swimming microorganism inside the fluid. Detail description of the source term/immersed solid used in this study can be found in the later sections of this chapter.

3.7 Solution strategy

ANSYS CFX uses a coupled solver, which solves the hydrodynamic equations (for *u, v, w, p*) as a single system. This solution approach uses a fully implicit discretization of the equations at any given time step. The flow chart, as shown in Figure (3.4), illustrates the general field solution process used in the CFX-Solver. The solution of each set of field equations consists of two numerically intensive operations. For each time steps:

1. Coefficient generation: The nonlinear equations are linearized and assembled into the solution matrix.
2. Equation solution: The linear equations are solved using an Algebraic Multigrid method.

When solving fields in the CFX-Solver, the outer iteration is controlled by the physical time scale and time step for steady and transient analyses, respectively. Only one inner (linearization) iteration is performed per outer iteration in steady state analyses, whereas multiple inner iterations are performed per outer iteration (or time step) in transient analyses.

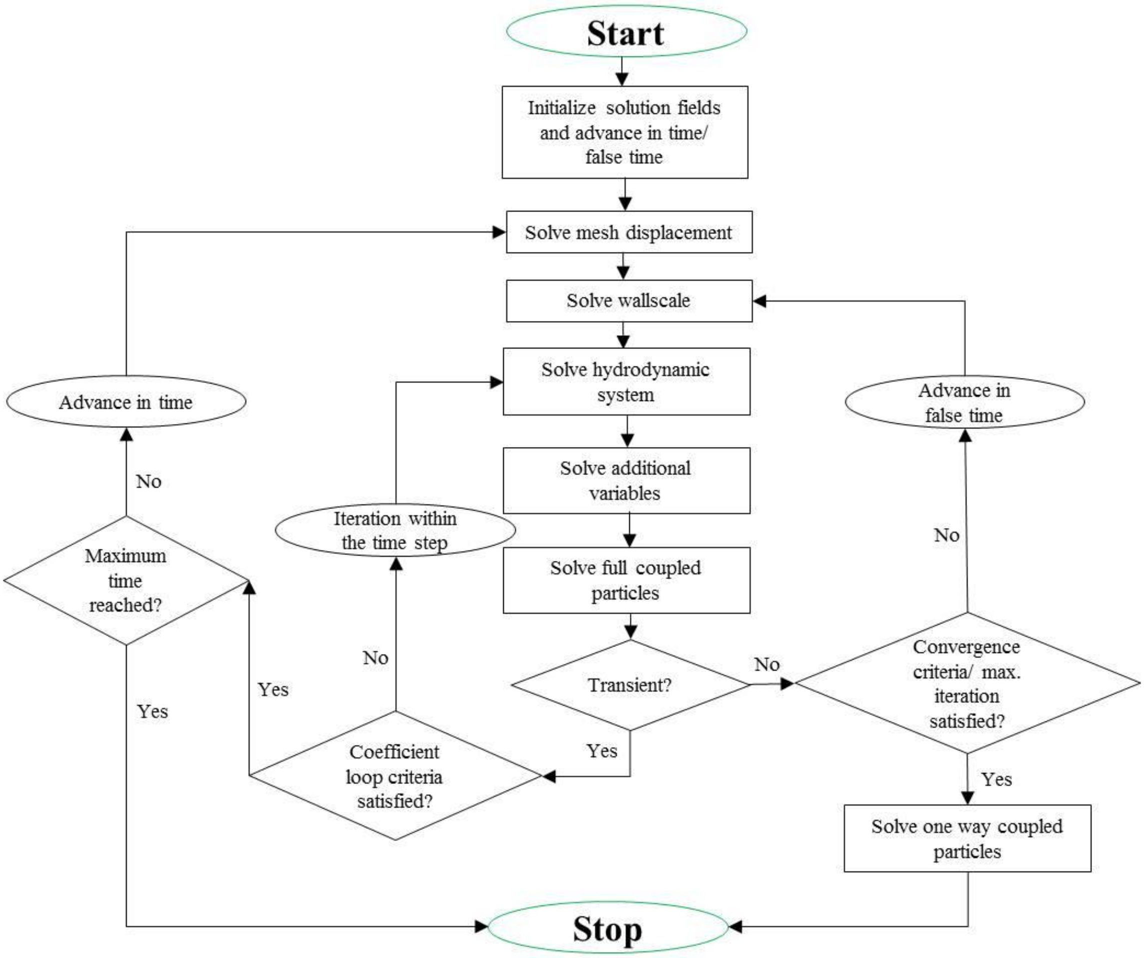

Figure 3.4: The general field solution process used by CFX-Solver in a transient and steady state analyses. (Source: reproduced from ANSYS CFX documentation 2011).

ANSYS CFX uses a Multigrid (MG) accelerated Incomplete Lower Upper (ILU) factorization technique for solving the discrete system of linearized equations. The linear sets of equations that arise by applying the finite volume method to all elements in the domain are discrete conservation equations. The system of equations can be written in the form:

$$\sum_{nb_i} a_i^{nb}\,\varphi_i^{nb} = b_i \tag{3.20}$$

where φ is the solution, b is the right hand side, a is the coefficients of the equation, i is the identifying number of the CV/node and *nb* means ‘neighbour’, but also includes the central coefficient multiplying the solution at the *i*th location. The Algebraic MG used by CFX-Solver, forms a system of discrete equations for a coarse mesh by summing the fine mesh equations. This results in virtual coarsening of the mesh spacing during the course of the iterations, and then refining the mesh to obtain an accurate solution. This technique significantly improves the convergence rates. The ILU factorization technique is an iterative solver whereby the exact solution of the equations is approached during the course of several iterations.

The linearized system of discrete equations described above (Equation 3.20) can be written in the general matrix form:

$$[A][\varphi] = [b] \tag{3.21}$$

where $[A]$ is the coefficient matrix, [φ] the solution vector and [b] the right hand side. The above equation can be solved iteratively by starting with an approximate solution, φ^n, that is to be improved by a correction, φ', to yield a better solution, φ^{n+1}, that is

$$\varphi^{n+1} = \varphi^n + \varphi' \tag{3.22}$$

where φ' is a solution of:

$$\dot{A}\varphi' = r^{\,n} \tag{3.23}$$

where $\dot{A}$ is the recomputed matrix of coefficients from the fine mesh coefficient matrix $[A]$, and $r^{\,n}$ is the residual which can be obtained from:

$$r^{\,n} = b - A\varphi^n \tag{3.24}$$

Repeated application of this algorithm will yield a solution of the desired accuracy.

3.8 Modelling of a microorganism as an immersed solid

In this study, a swimming microorganism was modelled as an immersed solid in a pre-defined fluid domain. To model any rigid solid object (immersed solid) that can move through fluid domain, CFX provides an option of immersed solid modelling in steady/transient state. The model involves the use of an immersed solid domain that is placed inside a fluid domain to represent the rigid solid object, including its shape, position, orientation and velocity. As the simulation proceeds, CFX-Solver calculates which parts of the fluid domain are overlapped by the immersed solid (ie within the immersed solid domain), and applies a source momentum to the fluid from inside the immersed solid domain in order to force the fluid to move with the solid. This has the effect of making the flow outside the immersed solid domain behave as if it were flowing around a rigid solid object. Additional forcing terms are applied at the boundary in order to improve the near-wall behaviour of the flow near the immersed solid boundary.

For example, in Figure 3.5, an arbitrary circular shape immersed solid domain is placed inside a fluid domain. When the immersed solid object is placed inside a fluid domain, it occupies the same volume of space as part of the fluid domain which contains the immersed solid. The ambient fluid flow conditions change accordingly based on the applied velocity of the immersed solid.

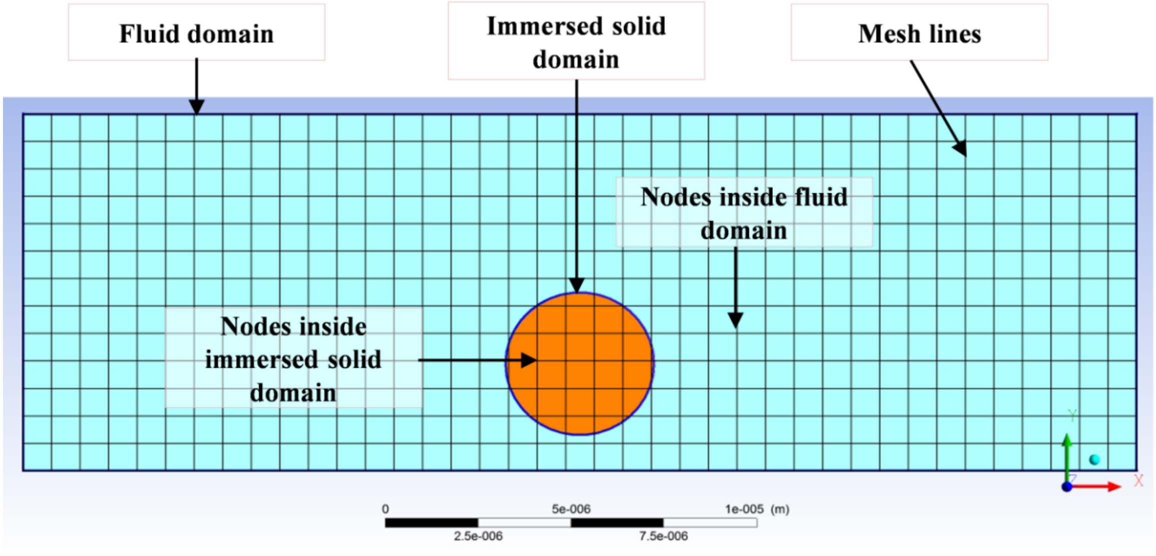

Figure 3.5: An immersed solid domain is placed inside a fluid domain. Additional source momentum would be applied to the mesh nodes lying inside the immersed solid domain.

The immersed solid boundary details can be depicted more clearly by taking a closer look (Figure 3.6) into previous figure (Figure 3.5). The nodes and the points near the boundary are labelled with different colors in Figure 3.6. The meaning of each label is also tabulated in Table 3.1.

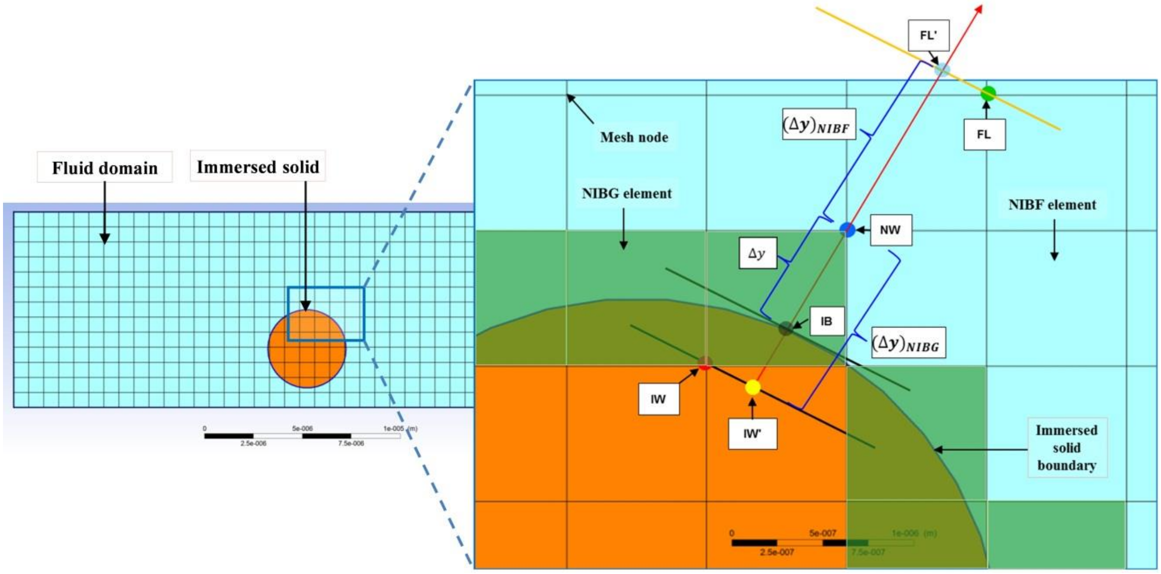

Figure 3.6: Immersed solid boundary details with near-wall elements and nodal distances. The arrow (red color) represents the wall normal distance corresponding to the given NW node. (Source: reproduced from ANSYS CFX documentation 2011).

Table 3.1: The nodes and the points near the boundary of a model immersed solid as shown in Figure 3.6.

Label	Meaning	Color labelling
IW	In-wall node	Red
IW'	In-wall point	Yellow
NW	Near-wall node	Deep blue
IB	Point on the immersed solid boundary	Black
FL	Fluid node	Green
FL'	Fluid point	Light blue

In Figure 3.6, the NIBG elements are elements between corresponding NW and IW nodes. These elements are in common boundary of immersed solid and outside fluid (ie elements which the immersed solid surface cuts through) and are in light green color. The NIBF elements between corresponding FL and NW nodes are entirely fluid elements (ie fully of fluid domains) and indicated as light blue colour elements. These are the elements which are immediately adjacent to the NIBG elements. The immersed solid boundary distances from the corresponding nodes have been noted as Δy, $(\Delta y)_{NIBG}$ and $(\Delta y)_{NIBF}$. Here it should be noted that Δy is the wall distance between the NW node and the IB point along the wall normal direction, and $(\Delta y)_{NIBG}$ is the distance between the NW node and the IW' point. $(\Delta y)_{NIBF}$ is the distance between the FL' point and the NW node.

The immersed solid is moving with a given velocity U_{IB}^{IMS} at its boundary through the fluid at U_{FL} velocity. The moving immersed solid develops forcing velocity which also alters the adjacent flow fields. This forcing velocity could be represented as a source term in the momentum equation (Equation 3.2) as

$$S_i = -\alpha\beta C\,(U_i - U_i^F) \tag{3.25}$$

where $U_i = U_x, U_y, U_z$ are the components of fluid velocity and $U_i^F = U_x^F, U_y^F, U_z^F$ are the components of forcing velocity due to the immersed solid. The momentum source coefficient $-C$ is a large number and is evaluated as the average of the three diagonal coefficients in the momentum equation. Further, α is the momentum source scaling factor which controls the size of the source term in the momentum equation. The default value for α in CFX, is 10, which balances the solution between accuracy and robustness. A higher value leads to a more accurate solution but is less robust and can give convergence difficulties.

The forcing function β, in Equation (3.25) is a special function which is used to calculate applied forcing terms based on near-wall treatment. If no near-wall treatment is used near the immersed solid boundary, the β function is set to be zero for fluid nodes lying outside the immersed solid domain, and one for fluid nodes inside the immersed solid. This is ideal for laminar flow conditions, the conditions used in this study. If near-wall treatment is activated, the β function is set to be volume-averaged inside function so that the β values and the corresponding forcing terms near the immersed boundary will be non-zero. The volume-averaged inside function averages the inside function, weighted by the nodal volume.

3.8.1 Solution procedure for an immersed solid

The CFX solver automatically updates the mesh positions of the immersed solid at the beginning of each time step for a transient simulation. When the position is set, the solver sets up a list of fluid nodes that lie inside the given immersed solid. The solver then applies the immersed solid sources to the fluid nodes that lie inside the immersed solid in order to drive the fluid velocity towards the immersed solid velocity.

In the case of laminar flow treatment (as used in this study), no wall scale equation is solved. Instead, the velocity near the immersed boundary is computed based on the wall distances, assuming constant wall shear in the boundary profile region. The tangential velocity at the near-wall fluid node (eg NW node) is governed by

$$(U_{NW}^{F})_{Tang} = (U_{IB}^{IMS})_{Tang} + (\frac{\mu_{FL}}{\mu_{NW}})\{\frac{(\Delta y)}{(\Delta y_{NBIF}+\Delta y)}\}\{(U_{FL})_{Tang} - (U_{IB}^{IMS})_{Tang}\} \tag{3.26}$$

where $(U_{NW}^{F})_{Tang}$ is the tangential component of the forcing velocity at the NW node, μ_{NW} is the dynamic viscosity at the NW node, U_{FL} and μ_{FL} are the fluid velocity and dynamic viscosity, respectively at the FL node. $(U_{IB}^{IMS})_{Tang}$ is the tangential component of the immersed solid boundary velocity at IB point. Here it should be noted that, $(\Delta y_{NBIF} + \Delta y)$ is the normal distance between the FL node and the immersed boundary as shown in Figure 3.6.

The normal component of the forcing velocity at the NW node is computed as the normal component of the boundary velocity, $(U_{IB}^{IMS})_{Norm}$ at the IB point on the immersed boundary:

$$(U_{NW}^{F})_{norm} = (U_{IB}^{IMS})_{Norm} \tag{3.27}$$

Thus the fluid velocity at the near-wall nodes is forced to be

$$U_{NW}^{F} = \sqrt{(U_{IB}^{IMS})_{Norm}^{2} + (U_{NW}^{F})_{Tang}^{2}} \tag{3.28}$$

In this way, the velocity field is forced to flow around the immersed boundary and thus also alleviate the problem of streamlines penetrating the immersed solid. At the beginning of each time steps, new fluid nodes come closer/inside the immersed boundary and simulated accordingly.

3.9 Conclusion

In this chapter, the numerical approach of modelling an immersed solid moving through a fluid domain has been demonstrated. The described method has been applied in this study to model swimming microorganism (a model bacterium) placed in the close vicinity of various solid boundary surfaces (plain/patterned). The immersed solid solution technique is a newly added feature in ANSYS CFX which is convenient for this kind of investigation. A bi-directional approach (ie fluid-structure interaction) of immersed solid could be an improved alternative of this modelling which is, however, currently unavailable in the immersed solid solution scheme of ANSYS CFX. The CFD results presented in this study were validated and supported by analytical solution and experimental output, respectively. Two different microbiological experiments were conducted using controlled hydrodynamics in a microchannel to support the CFD results. The materials and methods of these experiments have been described in the next chapter (Chapter 4).

Chapter 4

4 Materials and method: fabrication of microchannel and patterned surfaces

4.1 Introduction

The antifouling (AF) efficacy of synthetic microstructured/ patterned surfaces has been examined through novel experiment using a microchannel-based biofim reactor and controlled hydrodynamic set-up. A separate experiment was also conducted to investigate the dynamic stability of individual *Escherichia coli* cells over synthetic surfaces. The essential components of these experiments were the prefabricated microchannel and patterned surfaces. The fabrication of these items was done in a microfabrication lab following the standard protocol of fabricating microfluidic devices using the photolithography method.

The list of the prefabricated items is as follows:

1. Microwell arrays (sequentially placed 10 arrays) on two separate glass slides
2. One single microwell array on a glass slide
3. Polydimethylsiloxane (PDMS)-made rectangular microchannel

Microwell arrays were developed in two different phases for two experiments. In the first phase, 10 sequentially placed arrays of various diameter (1-10 µm) were developed on two different standard microscopy glass slide (75 mm × 25 mm × 1 mm), which were used for the first microbiological experiment (details in Chapter 5). A PDMS-made microchannel was also fabricated in this phase. A single microwell array with fixed diameter (10 µm) was developed in the second phase and was used in the second experiment (details in Chapter 6). The detail description of the materials and method used in developing these items and relevant processes will be presented in the following sections.

4.2 Photolithography method

Photolithography is a process used in microfabrication technique to transfer the geometric shape patterns from a mask onto a designated surface. The fundamental concept behind photolithography is the selective exposure of a photosensitive polymer known as photoresist, to ultraviolet (UV) light. This selective exposure is achieved by illuminating the photoresist through a mask (photomask), which typically consists of opaque chrome features on a transparent quartz backing. The result of this exposure is that localized chemical reactions are affected within the photoresist, which modulate its solubility and allow for the creation of discrete photoresist features. Photoresist being liquid film, can be spread out onto a substrate and can be exposed with a desired pattern. Patterns are thus transferred to a predefined photoresist layer. The first step involved in this photolithography method is to design the shape pattern and then the development of photomask imprinted with the shape pattern. Detail description of this step can be found in the following sections.

4.3 Pattern design and photomask generation

4.3.1 Pattern design

Two-dimensional (2D) circular shape wells arrayed over a specified area in two different phases for developing two surface patterns. The surface patterns consisted of (10 × 10) microwell arrays were fabricated in blocks and separated by plain surfaces. The sizes of the arrays of microwells were varied sequentially between 1 and 10 µm (diameter) with a 1-10 µm spacing. The arrays of microwells were distinguished with a code in the form D##S##. For example, D10S02 indicated microwells of 10 µm diameter and 2 µm edge to edge spacing. One single line of arrays was chosen at a time for one experiment with fixed spacing (2/5 µm). A PDMS microchannel was then placed over the selected line of arrays to form a closed rectangular channel. The line of arrays with 2 µm spacing was labelled as D01S02- D10S02 (Figure 4.1A). A second line of arrays with 5 µm spacing was chosen for similar experiment and labelled as D01S05- D10S05 (details in Chapter 5). In the second phase of microfabrication, a second pattern comprised of one single array of microwells was developed and labelled as D10S07 (Figure 4.1B). Detail of dimensions of all these arrays and experimental design set-up will be available in the relevant chapters. No surfaces contained any feature dimension smaller than 1 µm. The dimensional limitation was defined based on the known resolution limit of UV photolithography (~0.5 µm under ideal conditions) (Zheng 2005).

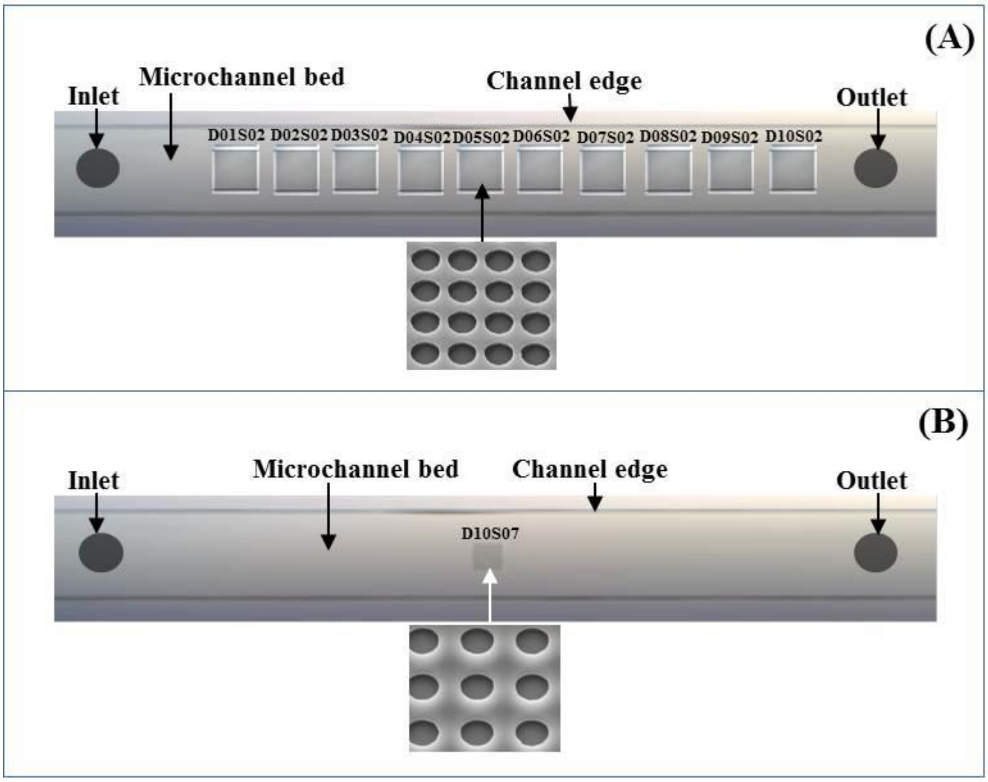

Figure 4.1: Pattern design of synthetic surfaces: (A) Ten blocks of microwell array in a microchannel bed with sequentially varied diameter of wells (labelled as D01S02-D10S02); (B) Single block of microwell array in a channel bed. Microwell arrays were developed onto a standard microscopic glass slide and then enclosed by a transparent PDMS-made microchannel.

4.3.2 Photomask specification

The Karl Suss brand mask aligners (model MJB3 and MA6) were used in the fabrication process. These contact masks aligner model supports (75 mm × 75 mm) to (175 mm × 175 mm) square photomasks and 75-200 mm diameter substrate/silicon wafers. Photomask is a piece of glass/quartz that can be used to transfer a design pattern to a material layer for further processing of photolithography. Photomask used in this study was made of Soda Lime (100 mm × 100 mm × 2.25 mm) with a thin a layer of chrome (~ 70 nm). The CAD design area for microwell arrays and microchannel were (11 mm × 11 mm) and (1 mm × 50 mm), respectively, which fit within the available design area of a (100 mm × 100 mm) square photomask (Figure 4.2).

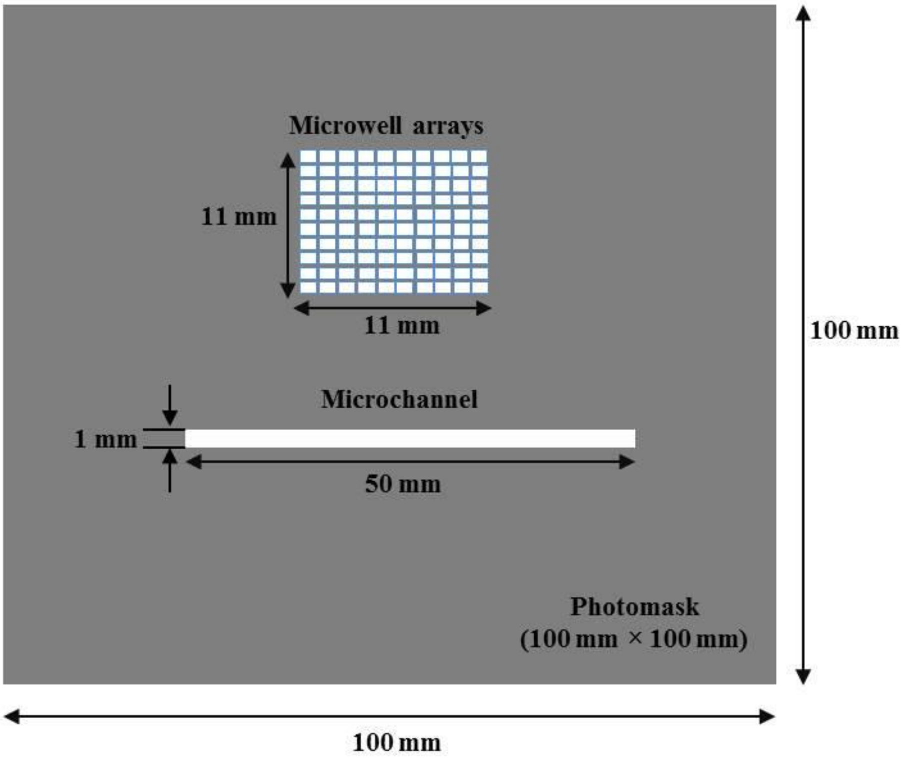

Figure 4.2: Schematic of photomask dimensions with representative design patterns of microwell arrays and microchannel. Dimensions are not to scale.

4.3.3 Pattern design digitization

Surface patterns were drawn using a student version of AutoCAD 2011 software package (Autodesk, Inc. USA). Figure 4.3 shows a CAD drawing with circular shape pattern

(D10S02) used in this study to develop microwell arrays. After finalizing the AutoCAD drawings and saving them in the proper file format (.dwg), the files were transferred to a professional photomask developer. The developer used a CAD translator program, named LinkCAD, to convert CAD files (.dwg) to GDSII file format (.gds).

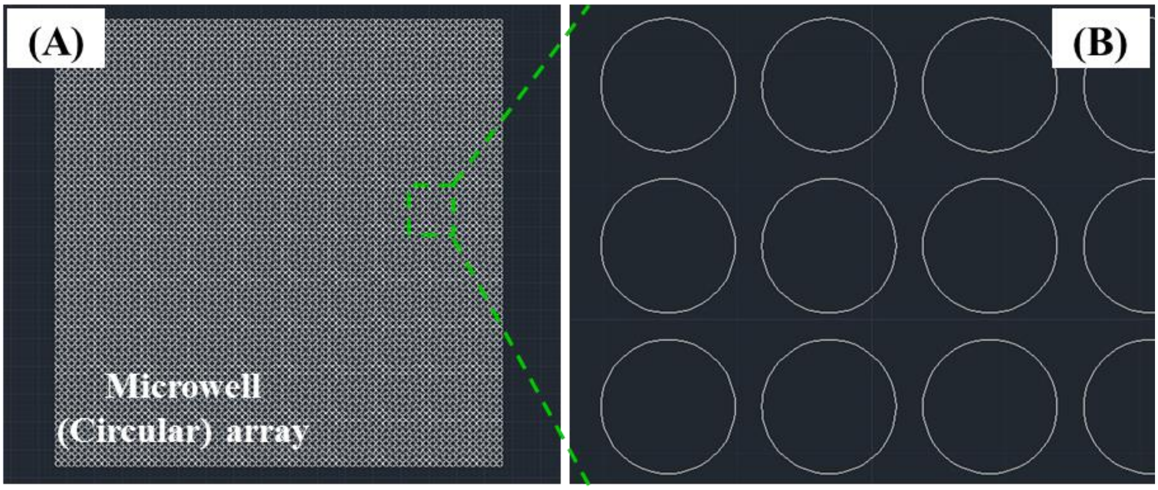

Figure 4.3: Surface pattern design by AutoCAD software: (A) An array of microwells (1 mm × 1 mm); (B) Zoom-in view of shape pattern (Circular, diameter 10 µm and spacing – edge to edge 2 µm, designated as D10S02).

4.3.4 Photomask fabrication

Photomask was developed by a commercial outsource, named Bandwidth Foundry International Pty Ltd, Australia. A laser writer named Heidelberg DWL200 was used for the writing process involved in the photomask development. The conventional procedures of photomask fabrication using DWL200 have been shown in Figure 4.4. Briefly, the blank photomask is made of Soda Lime/quartz with a thin a layer of chrome (< 100 nm) and photoresist. The blank photomask is subjected to laser exposure with DWL optical system where Scanning laser beam exposed photoresist following the layout (digitized design pattern) provided. After completing the writing/exposure process, the development of photoresist process started. The developing solution dissolve exposed resist and open the chrome layer. The next step is the chrome etching which develops the design pattern. The final step involves stripping of the photoresist layer by using Sulphuric-peroxide mixture, flushing and spin-drying. Figure 4.5 shows a representative final product photomask after completing all relevant processes.

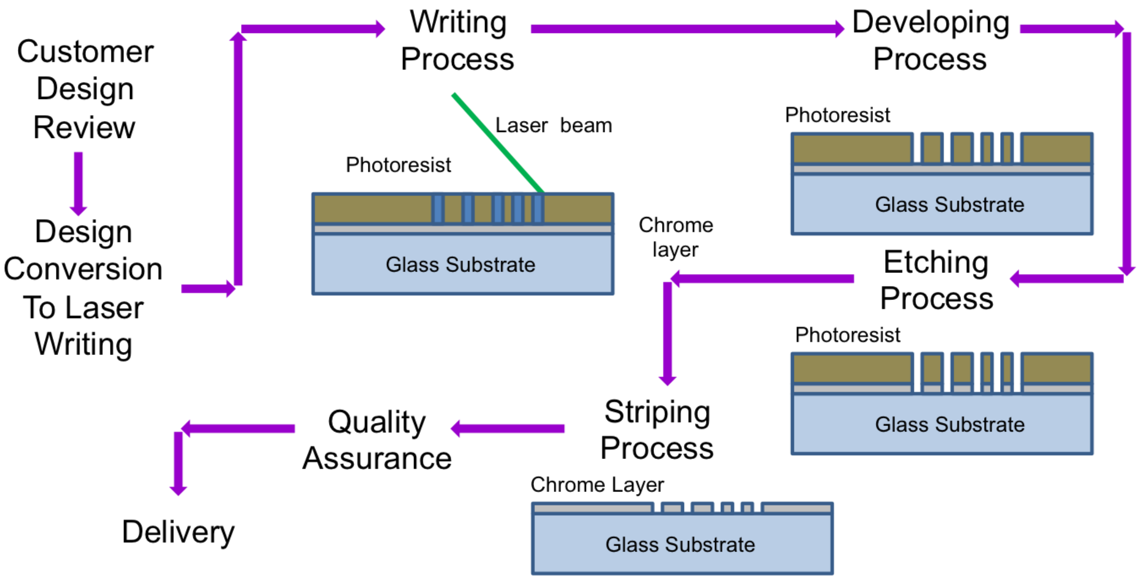

Figure 4.4: Schematic of photomask fabrication in Bandwidth Foundry International Pty Ltd, Australia (Source: http://www.bwfoundry.com).

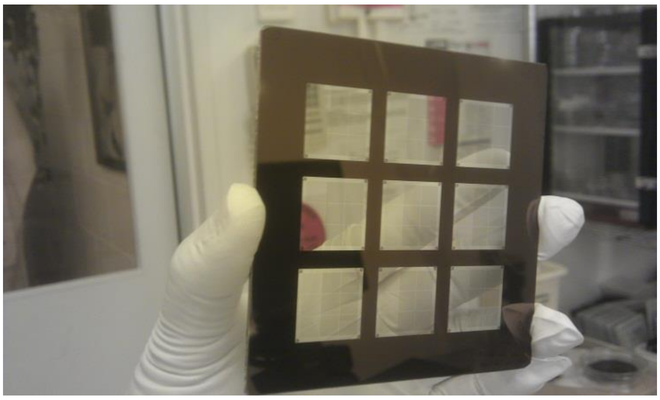

Figure 4.5: A typical photomask (dark areas are Chrome coated) of size (100 mm × 100 mm).

4.4 Process of photolithography

Photolithography, also termed as optical lithography, involves the transfer a geometric pattern from a photomask to a light-sensitive chemical ‘photoresist’ onto the substrate. It is essentially the same process that is used in lithographic printing. Photoresists are classified as either negative or positive, wherein their solubility is either increased or decreased by optical exposure, respectively. They are typically handled in liquid form, which is derived by the inclusion of solvents, and are coated as thin films onto suitable substrates by spin coating. Here, the centrifugal forces exerted by a spinning substrate reduce its thickness to an amount proportional to the spin speed and its viscosity. Thicknesses ranging from tens of nanometers to hundreds of microns are routinely obtained. The standard substrate used is the polished silicon wafer (Figure 4.6). However, in situation where the substrate itself needs to be transparent, other suitable material can also be used (eg glass slide, as used in this study). The entire photolithographic development was performed in the Microelectronic and Materials Technology Centre (MMTC), RMIT University, Australia.

Figure 4.6: Silicon wafer (100 mm diameter) with a polished surface which is commonly used as a standard substrate in the photolithography process.

Microwell-based patterned surfaces were fabricated onto glass slides using an epoxy-based negative photoresist SU-8 2005 (Microchem, USA). The microchannel was made of PDMS elastomer using KMPR 1025 (Microchem, USA) photoresist mould. The steps involved in developing the microwell-based patterned surface and the microchannel have been outlined in Figure 4.7.

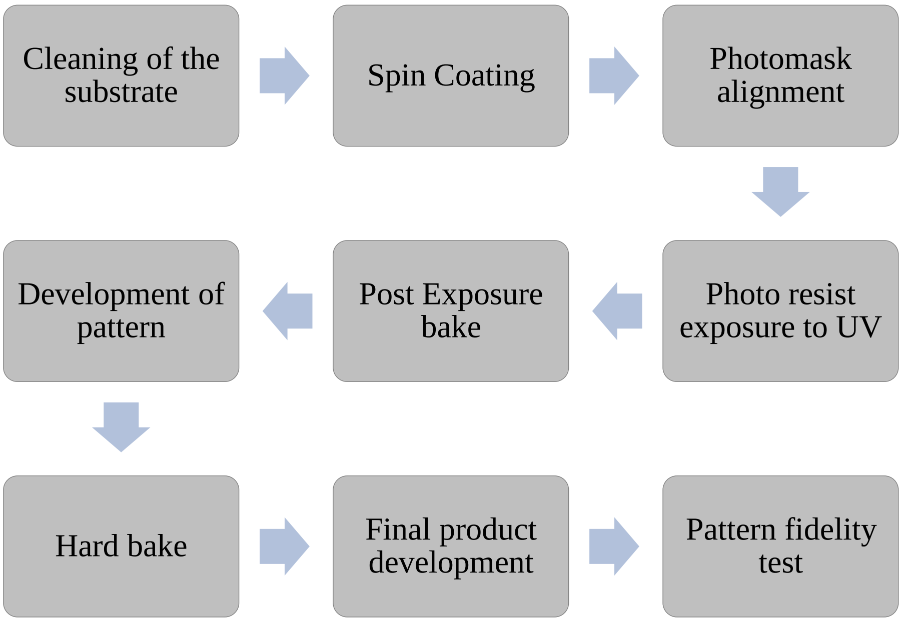

Figure 4.7: Flowchart of the conventional photolithography processes involved in the development of patterned surfaces and the microchannel.

The steps of the above mentioned photolithography technique have been described briefly in the following sections.

4.4.1 Cleaning/pre-treatment of the substrate

Performing photolithography requires the use of a clean-room environment. This minimizes the influence of airborne particulates on the fabrication process, which in turn allows for the routine deposition of uniform polymer films, and uninterrupted mechanical contact between photoresist films and masks.

Fabrication of the microwell-based patterned surfaces and microchannel was thus conducted in a clean-room environment situated at MMTC which began with the preparation of substrates. In the first step, the substrates (ie glass slide and silicon wafer) were chemically cleaned to remove particulate matter on the surface as well as any traces of organic, ionic, and metallic impurities. To develop microwells array, two 1mm glass slides were cleaned with acetone and isopropanol and dehydrated at 180°C for 5 min.

Similarly for developing microchannel, the 100 mm diameter silicon wafer was cleaned using acetone and isopropanol.

4.4.2 Spin coating

Spin coating has been used for several decades for the application of thin films. A typical process involves depositing a small puddle of a fluid resin onto the centre of a substrate and then spinning the substrate at high speed (typically around 3000 rpm) using a spin coater (Figure 4.8). Centripetal acceleration will cause the resin to spread to, and eventually off, the edge of the substrate leaving a thin film of resin on the surface. Final film thickness and other properties (eg uniformity and bonding) depend on the nature of the resin (viscosity, drying rate, (%) solids, and surface tension) and the parameters chosen for the spin process. Factors such as final rotational speed, acceleration, and fume exhaust contribute to how the properties of coated films are defined.

In this study, the cleaned and dehydrated glass slides were spin coated with the epoxy SU-8 2005 (Microchem, USA). The desired film thickness (5 µm) was achieved by setting the spin at 3000 rpm for 30 s. A 100 mm silicon wafer was spin coated to develop microchannel with KMPR 1025 (MicroChem, USA) photoresist using a spread cycle of 300 rpm and 100 rpm for 10 s and a development cycle of 1000 rpm and 300 rpm for 30 s, in order to achieve a film of 110 mm thickness with good uniformity. A cycle of edge bead removal was conducted for 30 s using edge bead removal solvent.

Figure 4.8: Spin coater is used to develop thin film of resin on the substrate surface. Epoxy Su-8 resin and KMPR 1025 (photoresist) have been used in this study to develop patterns on the glass surfaces and silicon wafer, respectively.

4.4.3 Soft bake

The epoxy based photoresist (onto glass slides) was soft baked on a hotplate for 2 min at 95°C to evaporate the remaining solvent, and then it was exposed to UV light through a high-resolution photomask. Similarly, the KMPR coated wafer was soft baked by ramping the temperature at 6°C min^{-1} starting from 23°C and holding at 100°C for 4 min to dry out the solvents.

4.4.4 Photomask alignment and photoresist exposure

Photomask contains the design pattern which can be transferred to the photoresist using contact mask aligner. A contact mask aligner achieves pattern transfer by mechanically mating the photomask to the photoresist, after which the two are illuminated with a planar ultraviolet wave front at normal incidence. Two different contact mask aligners, MA6 and MJB3, were used in this study (Figure 4.9). The SU-8 film of the glass slide was exposed to UV light through a high-resolution photomask for 6 s using a MA6 contact mask aligner (Karl Suss) with wavelengths of 365 and 405 nm (power 38mWcm^{-2}). Similarly, the KMPR film was exposed with a mask pattern for 2 min of UV on an MJB3 contact mask aligner with a wavelength of 360 nm and a power of (power 8mWcm^{-2}), using 2 exposures of 1 min each in order to avoid over heating the substrate.

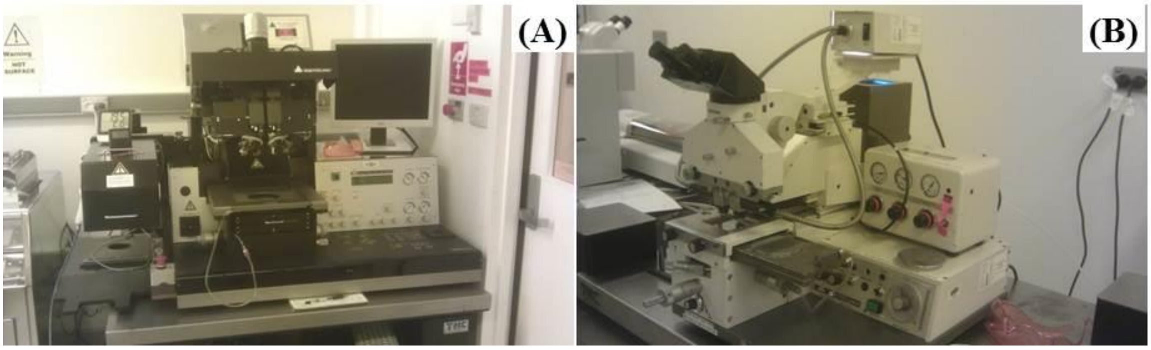

Figure 4.9: (A) MA6 and (B) MJB3 contact mask aligners were used to transfer patterns form photomasks to the Su-8 coated glass slides and KMPR coated silicon wafer, respectively.

4.4.5 Post exposure bake

After exposure the patterns were cross-linked by baking on a hotplate for 3 min at 95°C for glass slides, and for 4 min at 100°C for silicon wafer (increasing the temperature at 6°C min^{-1} starting from 23°C). The exposed and cross-linked films were then cooled down slowly to room temperature with the sample on the hotplate to avoid thermal stress on the films and possible cracks due to sudden changes in temperature.

4.4.6 Development of patterns

The glass slides were immersed in SU-8 developer (Microchem, USA) for 1 min to develop microwells by removing the unexposed photoresist from the surface. Then the glass slides were cleaned with isopropanol and deionized water very carefully so that the cleaning process does not alter the surface patterns. The KMPR coated silicon wafer was also developed by immersing into KMPR developer for 12 min with periodic agitation to remove the unexposed material. After developing the KMPR pattern, the wafer was cleaned with isopropanol and deionized water and a final hard bake was done.

4.4.7 Hard bake

The fabrication of microwells arrays onto the glass slides was completed with the above mentioned development and cleaning process. The microchannel fabrication process continued with hard backing and mould casting processes.

After cleaning the developed KMPR pattern, the silicon wafer was hard baked by heating the sample to 120°C for 3 h. Hard baking improved and strengthened the cross-linked KMPR pattern and extend the service life. The KMPR pattern was then ready for use as a mould for casting PDMS channel.

4.5 Fabrication of PDMS microchannel

The microchannel that was placed over a single line of array to develop the flow cell system was made of PDMS elastomer. It was developed using prefabricated KMPR mould as described above. The reason behind the use of PDMS as the material for microchannel is because of its many advantages in fabrication ease, suitable physical properties (eg low surface energy of 21.6 dyne/cm) (Barnes et al. 2003), biocompatibility and economy. Moreover, its optical transparency down to ~300 nm (Long 2002) makes it very well suited for microscopy analysis. It is the most widely used material in microfluidic device fabrication (Kalele et al. 2007, Gorgi 2008). PDMS is commercially available from Dow Corning as Sylgard 184 elastomer. Dow and Coring’s Sylgard 184 is a two-part system with mix ratio of cross-linker/curing agent A: siloxane B = 1:10. Increasing the cross-linker ratio in the mix can increase the rigidity of the PDMS produced (Campbell et al. 1999). Upon mixing, the PDMS was degassed for 30 min and then poured onto the KMPR mould previously made and contained within a polymethyl methacrylate (PMMA) shim. The PDMS was then cured in an oven at 100°C for 20 min. The PDMS channel was pealed from the KMPR mould and 0.75 mm inlet and outlet holes were made using a biopsy punch (Harris Uni-core™) (Figure 4.10).

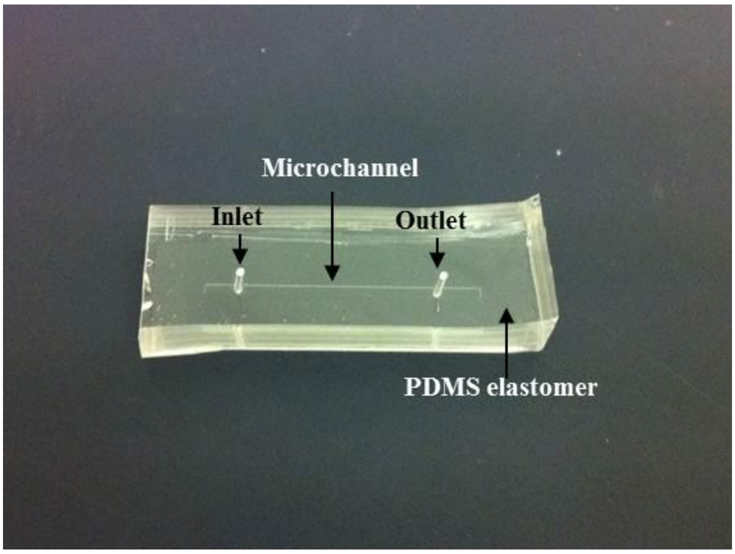

Figure 4.10: PDMS-made microchannel with inlet and outlet ports at the end of the channel.

4.6 Pattern fidelity evaluation

The surface patterns (arrays of microwells) were assessed using environmental scanning electron microscopic (ESEM; FEI Quanta 200, FEI Company, Hillsboro, OR, USA) (Figure 4.11). All ESEM images were taken at 30° tilt to get a clear view inside the wells (well depth 5 μm). The ESEM facility, including scientific and technical assistance, was provided by the RMIT Microscopy and Microanalysis Facility (a part of the Australian Microscopy and Microanalysis Research Facility), at RMIT University.

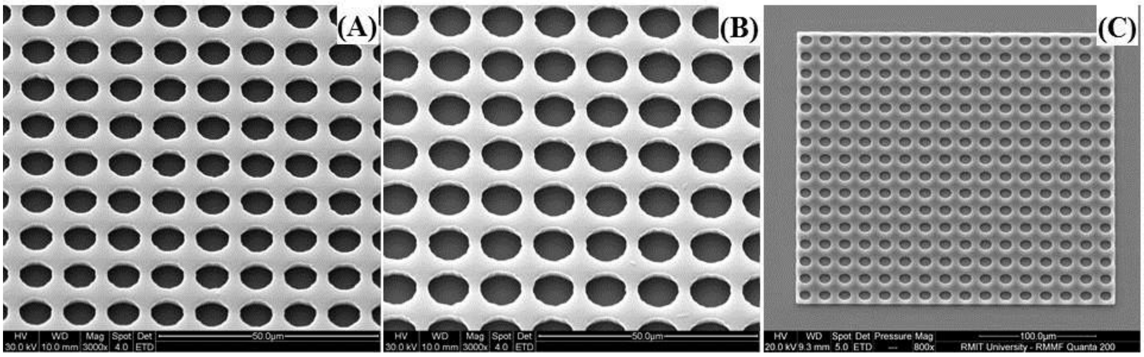

Figure 4.11: Assessment of surface patterns using ESEM: (A) D08S02- diameter 8 µm and spacing 2 µm; (B) D10S02- diameter 10 µm and spacing 2 µm; (C) Single array of wells with D10S07- diameter 10 µm and spacing 7 µm, used in the second microbiological experiment. All ESEM images were taken at 30° tilt to get a clear view inside the wells.

4.7 Conclusion

Photolithography is a widely used technique for design, fabrication and testing of microfluidic systems. The PDMS-made microchannel made it possible to analyse the microfluidic conditions and biofilm development with a greater control and precision. Various shape geometries and dimensions are now also possible in surface pattern design with greater accuracy. Irregular shape surface patterns (eg Sweat and Johnson 2013) or non-uniform patterns (eg Andersson et al. 1999) can influence the results with less control on microhydrodynamics. The development of microchannel and predefined surface patterns (eg circular shape pattern, as used in this study) established a new platform for the analysis of microhydrodynamics in relation to the early settlement of microorganisms and biofouling control for submerged surfaces. The next chapter (Chapter 5) will present a comparison of bacterial biofilm formation on these prefabricated surfaces with a real-time biofilm development monitoring system.

Chapter 5

5 Antifouling efficacy of synthetic patterned surfaces and microfluidic environment

5.1 Contributions

A novel microchannel-based flow cell reactor was proposed for conducting a set of microbiological experiments aiming to investigate the bacterial settlement on various synthetic patterned surfaces. The biofilm formation on microwell arrays (with varying diameter and spacing) was assessed experimentally based on (%) surface coverage, and compared with that on plain surface. Computational Fluid Dynamics (CFD) investigation of microfluidic environment was also performed to characterize the flow fields inside the microchannel. The experimental set-up with microchannel-based flow cell reactor, the assessment of biofilm formation on surfaces and the relevant numerical simulations were done solely by the author of this dissertation. The prefabrication of microchannel and surfaces was done in the microfabrication laboratory in the school of Electrical and Computer Engineering, RMIT University.

The content of this chapter has been published in 'Biofouling: The Journal of Bioadhesion and Biofilm Research' journal. It is presented here with small modifications.

Halder P, Nasabi M, Lopez FJT, Jayasuriya N, Bhattacharya S, Deighton M, Mitchell A, and Bhuiyan MA. 2013. A novel approach to determine the efficacy of patterned surfaces for biofouling control in relation to its microfluidic environment. Biofouling. 29:697-713.

5.2 Introduction

The research gaps presented in Chapter 2 need to be addressed to develop and optimize effective antifouling (AF) surfaces. Considering these research gaps, a set of experiments were designed and conducted to characterise the AF efficacy of microwell-based patterned surfaces. In this chapter, the details of the first three experiments, their design set-up and related Computational Fluid Dynamics (CFD) simulations will be presented. Another re-designed experiment that assessed the dynamic stability of individual microorganisms over surfaces will be described in Chapter 6.

The first three experiments were conducted to identify the correlation between bacterial biofilm formation and the microfluidic environment associated with various patterned and plain surfaces. Two different flow conditions (ie static and dynamic) were set for these experiments. A novel *in vitro* flow cell model (microchannel) was implemented for growing *Escherichia coli* bacterial biofilms under controlled hydrodynamic conditions on patterned surfaces. CFD simulations were also carried out to see how the microfluidic conditions were affecting the initial settlement of microorganisms.

5.3 Materials and methods

5.3.1 Experimental design setup

This test set-up is analogous to experiments described by Stoodley et al. (2002) and Lee et al. (2008). The flow cell apparatus used light microscopy (LM) to observe and quantify every stage of biofilm development under conditions of continuous flow. This test set-up has many advantages over the conventional Petri dish culture of microorganisms, which uses static/shaking fluid flow conditions (Carman et al. 2006; Schumacher et al. 2008; Cooper et al. 2011). Fluid flow conditions in a microchannel can be controlled more precisely (Lee et al. 2008; Zhang et al. 2011) than other methods of macrohydrodynamics (Qian et al. 1999; Schultz et al. 2000; Horn et al. 2003; Granhag et al. 2004; Crimaldi et al. 2007). A major drawback of using LM to monitor cell growth is its limited working distance for higher magnification objective lenses (eg for a 40× objective lens, the working distance is 2mm only). This was resolved by using a microchannel on a thin glass slide (1mm) and placing it on an inverted microscope. This imaging technique allowed real-time monitoring of live cells, which was not feasible in a Petri dish culture. Different geometric features of patterned surfaces were compared concurrently under the same conditions of flow and cell culture. Most importantly, as the fluid flow of this microchannel was controlled specifically, a correlation between the near-surface microhydrodynamics and biofilm growth could be established using CFD simulations. The entire microchannel system was enclosed to minimise the possibility of contamination.

5.3.2 Biofilm reactor system

Biofilms were grown in a rectangular polydimethylsiloxane (PDMS) microchannel (1mm wide, 0.11mm deep and 50mm long), whose channel bed was a thin glass slide, coated with SU-8 epoxy patterned with arrays of circular wells (microwells). The sizes of the arrays of microwells were varied sequentially between 1 and 10 μm (diameter) with a 1–10 μm spacing. The fabrication technique and relevant processes of developing this PDMS microchannel and microwell arrays can also be found in the previous chapter (Chapter 4). The microchannel was connected with a ‘once-through’ flow tube, fed from a mixing chamber as shown in Figure 5.1. The various components of the test set-up were connected by platinum-cured silicone tubing (L/S$^{®}$ 13, 16, Masterflex $^{®}$). The flow of nutrients into the mixing chamber and the flow rate into the flow cell were controlled by a dual channel peristaltic pump (Masterflex$^{®}$, L/S$^{®}$ drive with Easy-load® 3 pump head). The inflow rates of the sterile nutrient medium at the mixing chamber and the inlet of the microchannel were the same (0.001 ml s^{-1}). One glass flow break (BST FB 50, Biosurface Technologies Corp. USA) was used between the peristaltic pump and the mixing chamber and another was placed in the effluent line between the waste reservoir and the flow cell to avoid contamination. To capture gas bubbles before they entered the flow cell, a bubble trap (BST FC 33, Biosurface Technologies Corp. USA) was used between the peristaltic pump and the flow cell. The bubble trap also acted as a pulse damper to reduce pulses of inflow developed by the peristaltic pump. The flow cell was positioned on the stage of an inverted light microscope (Carl Zeiss, Axiovert 25c) for continuous monitoring of the growth of the biofilm.

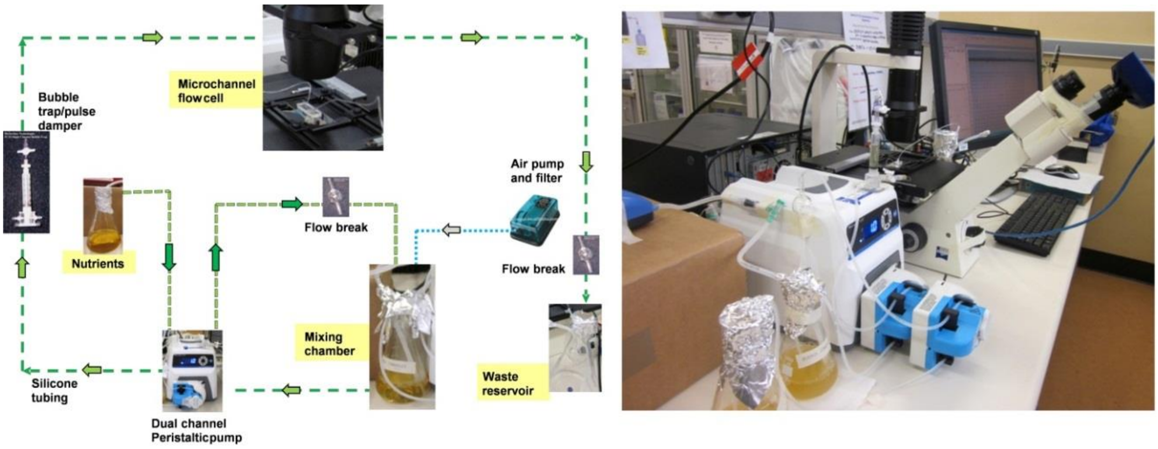

Figure 5.1: Schematic of experiment (left) and laboratory setup (right) for biofilm growth assessment on patterned surfaces.

5.3.3 Flow cell fabrication

The flow cell device consisted of two components: microwell arrays fabricated on a glass slide using an epoxy-based negative photoresist SU-8 2005 (Microchem, USA) and a microchannel made of PDMS (Figure 5.2). The microwell arrays were fabricated in blocks of (1000× 1000) μm^2 separated by 100 μm of plain surfaces. The arrays of microwells were distinguished with a code in the form D##S##. For example, D10S05 indicated microwells of 10 μm diameter and 5 μm edge to edge spacing. Details of this labelling procedure have been described in Chapter 4. A prefabricated PDMS microchannel was placed over the microwell arrays to form a closed rectangular channel with one inlet and one outlet at the ends (Figure 5.2). In total, three experiments were conducted to compare the growth of biofilms on different geometries under different fluid flow conditions. The first two experiments were set with sequentially placed 1– 10 μm diameter circular wells with 2 and 5 μm spacing (designated as D01S02– D10S02 and D01S05– D10S05, respectively), under flowing fluid conditions. The third experiment was conducted on the entire array of microstructured surfaces placed in a Petri dish under static fluid conditions. The microwells were fabricated using a conventional photolithography technique as described in Chapter 4.

Briefly, a 1mm glass slide was cleaned and then spin-coated with SU-8 2005 (Microchem, USA) to yield the desired film thickness of 5 μm (microwell depth). The resist was then soft baked and exposed to UV light through a high-resolution photomask.

Then the coated surface was hot baked and immersed in SU-8 developer to develop microwells. The PDMS microchannel was fabricated following the method of Lopez et al. (2010). Briefly, a mould of the inverse microchannel pattern was developed using KMPR photoresist and then the PDMS microchannel was cast against this mould. Finally, the microwell arrays and the microchannel were brought into conformal contact and bonded. The two-layered device (flow cell device) was mounted on an inverted microscope stage. The inlet and outlet ports of the microchannel were cut with a 0.75mm punch (Harris Uni-core™) and were connected by a flat-ended 0.81mm metal pin to the tubing (L/S® 13, Masterflex®).

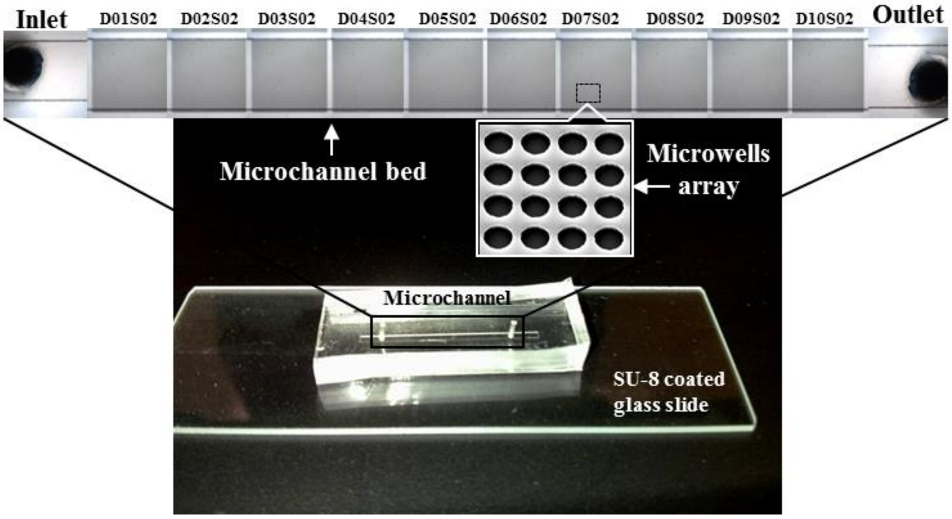

Figure 5.2: Microchannel made from PDMS with arrays of microwells (patterned surfaces) fabricated on a SU-8 coated glass slide. A zoom-in view of the microchannel bed shows array of microwells with D07S02 configuration.

5.3.4 Flow cell hydrodynamics

Published data suggest that the critical shear stress required to detach microorganisms from surfaces varies greatly depending on parameters such as, species, morphology, contact time, physico-chemical properties of the contact surfaces, adhesive properties of the secretions of the microorganisms, successive attachments and biofilm density (Finlay et al. 2002; Granhag et al. 2004; Bol et al. 2009, Larsson et al. 2010). For example, the critical shear stress of mixed species biofilms, developed from activated sludge, varies from 0.01 to 0.5 Pa (Bol et al. 2009). Studies on fouling removal by applying water jet (eg Granhag et al. 2007) showed that algal spores such as *Ulva intestinalis (syn. Enteromorpha intestinalis)* failed to settle in a free-stream flow speed which is ~ 20 cm s^{-1}. Granhag et al. (2007) also showed that green alga *Ulva intestinalis* were able to settle to a greater extent (< 50% settlement compared with still water) when flow speed at spore height was lower than or equal to the swimming speed of the spores (~ 0.2 mm s^{-1}). As this study aimed to investigate the efficacy of different patterned surfaces rather than the hydrodynamic approach of biofilm detachment, an identical value of flow rate was taken (0.001 ml s^{-1}) for the first set of microbiological experiments under flowing fluid conditions. Experiments with similar microwell configurations were also conducted under static fluid conditions to compare the effects of flow environments. The maximum wall shear stress and average flow velocity of the flow cell were calculated analytically for a rectangular channel with a plain surface bed. For capillary geometries where the depth is much smaller than the width (at least 5 times) the wall shear stress τ_W can be written as (Macosko and Larson 1994):

$$\tau_w = \frac{6Q\mu}{bh^2} \tag{5.1}$$

where Q = flow rate (defined as $Q = \bar{V}bh$) in [ml s^{-1}] and μ = dynamic viscosity of water at 20°C (μ = 1.0×10^{-3} N.s m^{-2}). The width b = 1 mm, the height h = 0.11 mm and the corresponding flow rate Q = 0.001 ml s^{-1} gave the shear stress τ_W= 0.5 Pa at the channel bed. The developed strain rate was $\dot{\gamma} = \tau_w / \mu$ = 500 s^{-1}. The average flow velocity was $\bar{V}$ = 9.17 mm s^{-1} and the corresponding Reynolds number Re = 1.82, calculated as:

$$Re = \frac{\rho u D}{\mu} \tag{5.2}$$

where ρ = density of water at 20°C (ρ= 1.0×10^{3} kg m^{-3}) and D is the hydraulic depth of the channel ($D = 2bh/(b+h)$ = 0.2 mm). In laminar flow, the hydrodynamic entry length was calculated approximately (Kays and Crawford 1993; Bhatti and Shah 1987) as $L_{h,laminar} \cong 0.05\,ReD = 20\ \mu\mathrm{m}$. The calculated Reynolds number (~2.0) and hydrodynamic entry length (< 0.1 mm, plain surface next to microwells array) confirm that the applied flow was fully developed laminar flow.

Here, it should be noted that the applied flow rate developed about 30× higher velocity near to the surface (1mms^{-1} at 0.002mm height from the surface) than the average swimming velocity (~0.03mms^{-1}) of the model microorganism, *E. coli* K-12 (Berg 2004; Darnton et al. 2010) in a bulk liquid. The applied strain rate (500 s^{-1}) was sufficient (ie >10 s^{-1}) to dominate the hydrodynamic forces over the flagellar propulsion of *E. coli* (Hill et al. 2007). The settlement scenario could therefore be observed in an intensive shear-driven microfluidic environment where physical factors, like hydrodynamic forces, become considerably more prominent than biological factors (eg self-propulsion and chemotaxis), which is not the case under static flow conditions.

5.3.5 Reactor sterilization

The majority of the reactor system and nutrients were autoclaved. Heat-sensitive components were sterilized using a method adapted from Fisher and Petrini (1992) by exposure to 70% ethanol for 15 min, 40% NaOCl solution (~12% available chlorine when undiluted) for 15 min, and again to 70% ethanol for 15 min. To verify sterility prior to inoculation, three 0.1 ml aliquots of effluent were plated onto King’s B agar after the flow system had been run with sterile media for three days following the method described by Stoodley et al. (2002). Cultures were incubated at 37 °C for 24 h and examined for microbial growth.

5.3.6 Inocula and nutrients

Biofilms of *E. coli* K-12 were grown in the flow cell as well as in a Petri dish for 4 days (96 h). Briefly, nutrient broth (CM0067, Nutrient broth No. 2, Oxoid, UK) was added to the mixing chamber and inoculated with *E. coli*. The chamber was placed in a shaker incubator (INFORS HT, Switzerland) at 80 rpm and 37 °C for 24 h. The final concentration of *E. coli* in the mixing chamber was determined by serial dilutions and plate counts (~1.0×10^{7} CFU ml^{-1}). The chamber was then connected with the flow cell system for continuous culture with nutrient feed and waste disposal for the next 96 h. For culture in static fluid conditions, the test surface was immersed in the inoculated nutrient broth for 96 h.

5.3.7 Image analysis

For the first two experiments, real-time biofilm growth was monitored continuously and images were captured at regular intervals using light microscopy using LM (phase contrast) and a Carl Zeiss microscope camera (AxioCam MRc). At the end of 96 h of exposure to fluid flow, images were taken using an environmental scanning electron microscopic (ESEM; FEI Quanta 200, FEI Company, Hillsboro, OR, USA). All ESEM images were taken at 30° tilt to get a clear view inside the wells (well depth 5 μm). Samples were prepared for ESEM by sputter coating with gold (~10 nm). In the case of the third experiment, ESEM images only were taken after 96 h of batch culture. All images were analysed for percentage surface coverage using IMAGEJ software (http://rsbweb.nih.gov/ij/).

5.3.8 Statistical analysis

Bacterial settlement on each surface type was reported as the mean surface coverage (in %) from three replicate sets of ESEM images. In total, the three replicate sets contained 126 images (ie 3 sets × 21 surfaces × 2 flow conditions) of bacterial settlement on different pattern and plain surfaces for two different flow regimes (static/ dynamic). Statistical differences between the surfaces were evaluated using a two-way ANOVA followed by the Sidak multiple comparisons test. Statistical differences were considered significant at the 95% confidence level. All statistical analyses were performed using GraphPad Prism software (version 6.00 for Windows; GraphPad Software, La Jolla California USA, www.graphpad.com).

5.3.9 CFD analysis of patterned surfaces

A commercially available CFD software package (ANSYS CFX, Version 13.00, ANSYS Inc., Canonsburg, PA, USA) was used to solve both continuity and Navier–Stokes equations (Equations 5.3 and 5.4, respectively) for pressure and velocity fields.

$$\vec{\nabla} \cdot \vec{V} = 0 \tag{5.3}$$

$$\rho \frac{D\vec{V}}{Dt} = -\vec{\nabla}P + \rho\vec{g} + \mu\nabla^2\vec{V} \qquad (5.4)$$

The velocity vector $\vec{V}$ can be described here as:

$$\vec{V} = u\vec{i} + v\vec{j} + w\vec{k} \qquad (5.5)$$

where u, v and w are the velocity components in the x (longitudinal), y (vertical) and z (lateral) directions, respectively. The fluid domains were considered differently in the two sets of simulations of plain and patterned surfaces. For the first simulation, the entire fluid domain (1mm wide, 0.11mm deep and 50mm long) of the microchannel was taken to verify the resultant wall shear stress as obtained analytically from Equation 1. The inlet flow rate was set at 0.001 ml s^{-1} as used in the experiments. Channel walls were considered plain surfaces with no-slip boundary conditions. Wall shear stress was ~0.5 Pa at the maximum area of the channel bed (as shown in Figure 5.3A). To model the flow over small microstructures on the surfaces, three small domains around the microstructures were considered within the viscous sublayer of a fully developed laminar flow (second set of simulations). Each fluid domain was 65 µm in length, 50 µm in width and 10 µm in depth; two consisted of D10S05 and D10S02 size microwells (in arrays of 4×3) at the channel bed, while the third one was a plain surface. As the velocity profile of the full-depth channel was parabolic in nature and the very surface velocity distribution was linear (Figure 5.3B and C), the flow in this region (within the viscous sublayer) could be considered the same as the flow between two parallel plates to generate Couette flow (Freidmann 2010b). To get a similar range of shear stress (~ 0.5 Pa as obtained from the analytical solution using Equation 1 and in the first simulation) at the channel bed, a velocity of 5mms^{-1} (as shown in Figure 5.3C) was applied to the upper plate of the fluid domains of the second set of simulations.

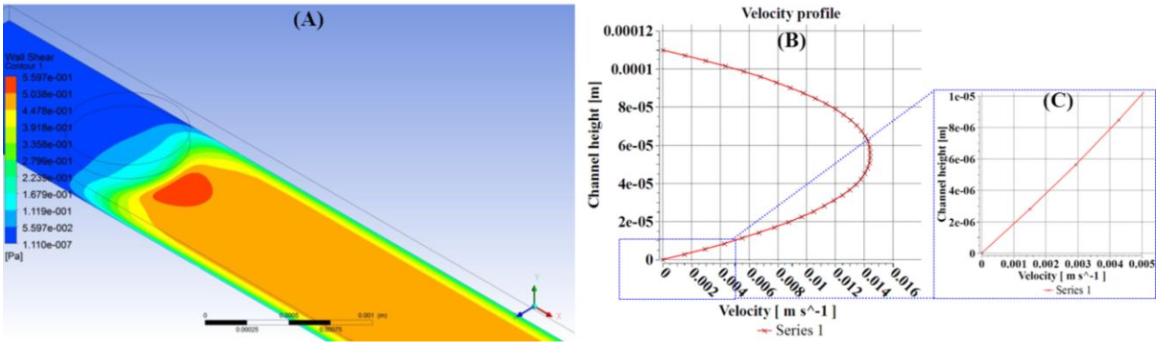

Figure 5.3: CFD simulation and velocity profile of a microchannel: (A) Part of entire fluid domain of a microchannel shows wall shear development at the channel bed near to the inlet; (B) parabolic velocity profile of the microchannel at its full depth; (C) linear velocity distribution within the viscous sublayer at 10 µm height from the channel bed; the velocity at this height is 5 mms^{-1}.

5.4 Results

The surface coverage of bacteria showed dissimilarities for different patterned and plain surfaces. In most cases, ESEM images indicated that microorganisms preferred to settle on plain surfaces *cf.* patterned surfaces, but this varied with flow conditions (Figure 5.4). The mean surface coverage areas for plain surfaces were 84.02% in static and 65.96% in dynamic flow conditions, respectively (see also Table 5.1).

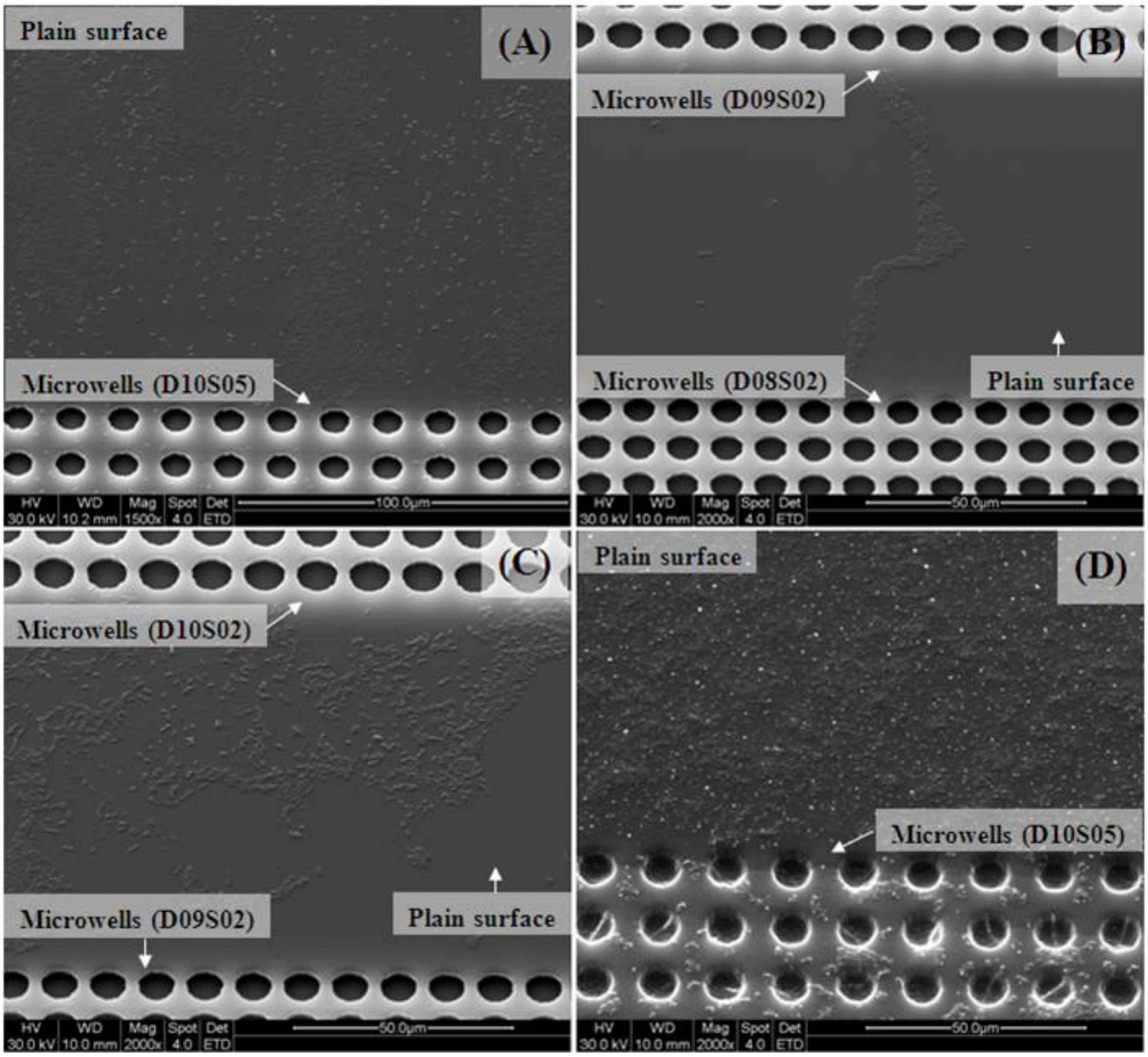

Figure 5.4:ESEM images of *E. coli* settlement on surfaces after 96 h of flowing fluid conditions (A–C) and static fluid conditions (D). Settlement on (A) a plain surface next to D10S05 microwells, (B) in between D09S02 and D08S02, (C) in between D10S02 and D09S02, (D) on a plain surface next to D10S05. *E. coli* preferred to settle mainly on plain surfaces instead of adjacent patterned surfaces in flowing fluid conditions (A–C). Flow direction from bottom to top of image for (A–C).

Table 5.1: Comparison of bacterial microcolonies on different surfaces in static and dynamic flow conditions.

				Size of microcolony			
Surface type	Flow condition	Number of microcolonies 1000 µm^{-2}	Surface coverage (%)	Mean (µm^2)	SD (µm^2)	Min. (µm^2)	Max. (µm^2)
D05S02	Static	16.14	61.73	29.1	29.37	1.48	193.35
D05S05	Static	22.00	59.29	15.22	23.31	0.81	202.68
D08S02	Static	16.48	42.39	19.94	14.78	1.26	79.51
D08S05	Static	17.89	30.62	20.35	22.39	0.83	166.18
D10S02	Static	13.25	20.58	19.66	14.36	0.62	72.1
D10S05	Static	13.58	39.24	34.62	43.56	0.54	274.64
Plain	Static	6.54	84.02	79.63	455.82	3.4	3833.09
D05S02	Dynamic	0.45	0.12	3.1	0.68	2.5	4.29
D05S05	Dynamic	16.39	6.71	7.63	31.56	0.55	329
D08S02	Dynamic	0.16	0.05	1.42	0.00	1.42	1.42
D08S05	Dynamic	25.33	18.02	3.55	4.29	0.74	33.43
D10S02	Dynamic	0.62	1.28	1.97	0.42	1.55	2.42
D10S05	Dynamic	18.42	2.25	3.07	2.53	0.63	17.93
Plain	Dynamic	7.49	65.96	107.24	391.71	0.74	1468.16

The settlement of bacteria on patterned surfaces was compared with plain surfaces for two different flow conditions (static and dynamic) with two different spacings (5 and 2 µm) between wells (Figure 5.5). In the case of 5 µm spacing, there was no significant difference in the surface coverage between the plain surface and the microwells (D01S05–D07S05) under static conditions, but significant differences existed in all cases under dynamic flow condition, except for D01S05–D03S05 and D06S05 surfaces (Figure 5.5A). Similarly, in the case of 2 µm spacing, there was no significant difference between the plain surface and the microwells (D01S02– D05S02) under static flow conditions, but significant differences existed in all cases between plain and patterned surfaces under dynamic flow conditions (Figure 5.5B). It should be noted that bacterial coverage on plain surfaces under different flow conditions was not significantly different ($p = 0.05$). These data suggested that bacterial settlement on patterned surfaces with 2 µm spacing showed the most variation *cf.* plain surfaces under dynamic flow conditions.

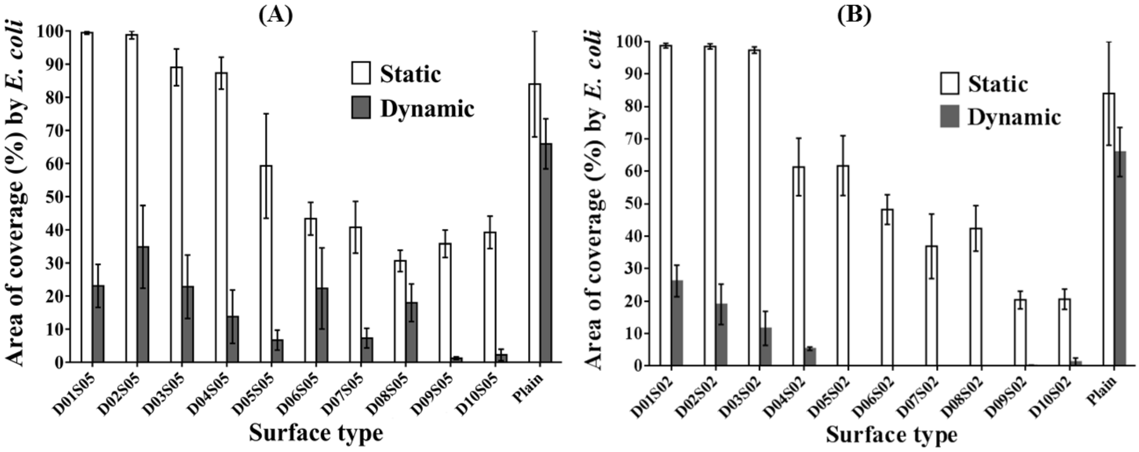

Figure 5.5:Bacterial settlement (surface area coverage (%)) for different surfaces in two different flow conditions. (A) Surfaces with 5 µm spacing, (B) surfaces with 2 µm spacing. Each datum point represents mean surface coverage (%) ± SEM (standard error mean).

Another comparison of surface coverage area in relation to flow condition (static *vs* dynamic) showed that differences in bacterial settlement between surfaces were most inconsistent for larger spaced (5 µm) microwells. For example, coverage on D06S05, D08S05 and plain surfaces were not significantly different between static to dynamic flow conditions (Figure 5.5A). On the other hand, more sequential and consistent results could be found in the case of wells with a 2 µm spacing. For this case, sequentially placed surfaces such as D09S02, D10S02 and plain surfaces did not show significantly different surface coverage (Figure 5.5B) under different flow conditions in a two-way ANOVA analysis followed by the Sidak multiple comparisons test. It could be noted that in dynamic flow conditions the surface coverage was the lowest for D06S02–D09S02 surfaces. All statistical differences were analyzed by 2-way ANOVA followed by Sidak’s multiple comparisons test using GraphPad Prism software. The analysis was double-checked by Bonferroni’s multiple comparisons test (at 95% confidence interval) and the result was found consistent. In all cases, surface coverage was lower in dynamic flow conditions than in static flow conditions.

The effect of smaller diameter microtopographies was examined in relation to the phenomenon of spreading out of settlement areas after 96 h of continuous culture (LM images, Figure 5.6). It was observed that the settlement areas covered both plain surface (area between D02S02 and D03S02) and smaller diameter microwells (Figure 5.6A), whereas settlement expansion was restricted to plain surfaces bounded by larger diameter microwells (area between D08S02 and D09S02; Figure 5.6B).

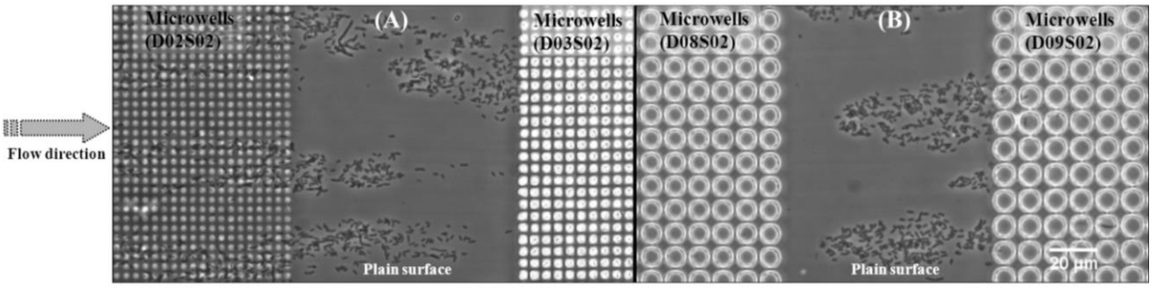

Figure 5.6: Light microscope images to compare the settlement of *E. coli* on different locations of the microchannel bed after 96 h of flowing fluid conditions. (A) Settlement in between D02S02 and D03S02, (B) in between D08S02 and D09S02. The settlement of *E. coli* covered both the plain surface and the smaller microwells (D02S02–D03S02) but could not extend in the case of the larger microwells (D08S02 and D09S02). Flow direction from left to right. Scale bar = 20 μm.

The effects of fluid flow conditions (static/dynamic) and spacing were also compared for the same diameter (10 μm) microwells (Figure 5.7) and for different diameter (5, 8 and 10 μm) microwells (Figure 5.8). In relation to flow conditions, higher numbers of bacterial cells settled on the surfaces in static fluid conditions (Figure 5.7A and C, 47.02 and 26.04% surface coverage, respectively) than flowing fluid conditions (Figure 5.7B and D, 5.65 and 0.12% surface coverage, respectively). Similarly, spacing between microwells also exhibited a distinct influence on the settlement events under different flow conditions. For spacings of 2 μm as opposed to 5 μm for microwells with the same diameter (10 μm), settlement of *E. coli* was reduced to a minimum level (Figure 5.7B and D, 5.65 and 0.12%, respectively).

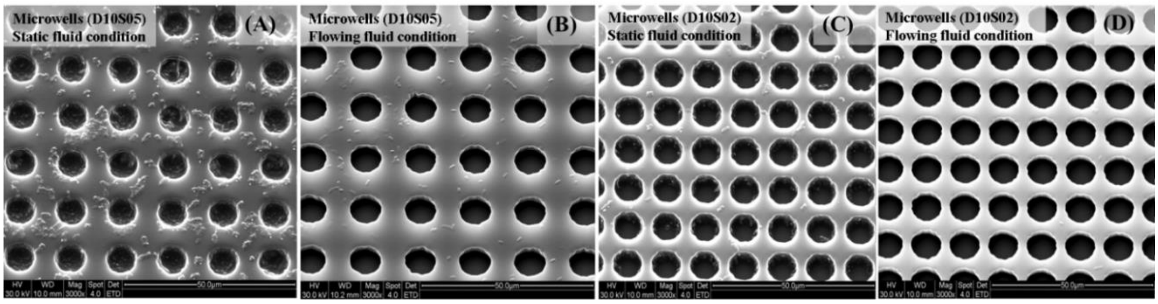

Figure 5.7: ESEM images of the settlement of *E. coli* on surfaces after 96 h of culture. (A) D10S05 in a static fluid condition (surface coverage = 47.02%), (B) D10S05 in a flowing fluid condition (surface coverage = 5.65%), (C) D10S02 in a static fluid condition

(surface coverage = 5.65%), (C) D10S02 in a static fluid condition (surface coverage = 26.04%) and (D) D10S02 in a flowing fluid condition (surface coverage = 0.12%). Scale bars = 50 μm.

Similar results were observed for different diameter microwells (Figure 5.8). The influence of the spacing between wells was evident in dynamic flow conditions compared to static conditions. Settlement decreased significantly with a reduction in spacing. For example, in dynamic flow conditions, surface coverage of 18.02% on D08S05 reduced to 0.05% on D08S02 (Figure 5.8B; Table 5.1). However, in static flow conditions, a reduction in spacing (eg for 5 and 8 μm diameters) increased the settlement in some cases (Figure 5.8A). In dynamic flow conditions, patterned surfaces became more effective at inhibiting group settlement (gregariousness) of microorganisms than plain surfaces.

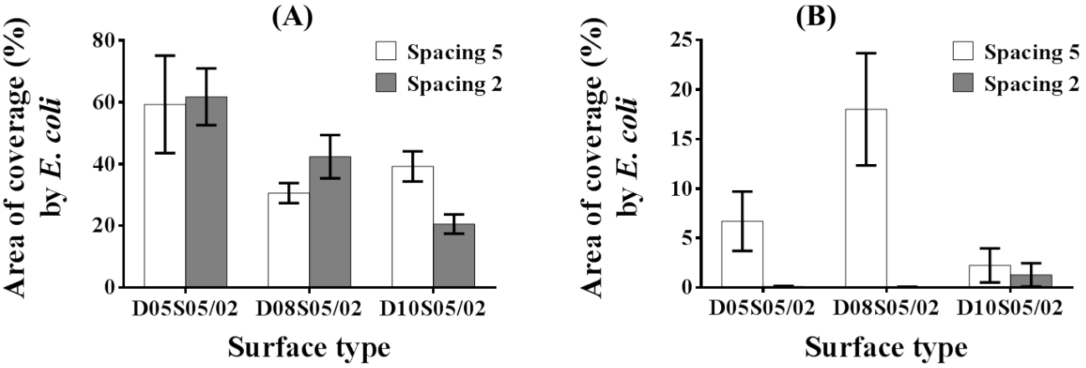

Figure 5.8: Bacterial settlement (surface area coverage (%)) for 2 spacings (2, 5 μm) on different surfaces (diameter of microwells = 5/ 8/10 μm) in two different flow conditions. (A) static flow conditions, (B) dynamic flow conditions. Each datum point represents mean surface coverage (%) ± SEM.

Figure 5.9 shows that the few microcolonies that developed on the plain surface were very large in size in comparison to microcolonies settled on a D08S05 patterned surface. The maximum sizes of bacterial clusters on plain and D08S05 surfaces were 1468.16 and 33.43 μm^2, respectively, in dynamic flow conditions (Figure 5.9; Table 5.1). Table 5.1 shows more a detailed comparison of these observations. Higher standard deviations (SD) for plain surfaces (SD = 455.82 and 391.71 μm^2 for static and dynamic flow conditions, respectively), indicated the wider variation in sizes of microcolonies (min. 3.4 μm^2 to max. 3833.09 μm^2). The sizes of microcolonies were more uniform for patterned surfaces (eg SD 4.29 μm^2 for D08S05) in dynamic flow conditions. It could therefore be stated that patterned surfaces inhibited formation of larger bacterial clusters. A similar observation on the inhibition of group settlement by *Staphylococcus aureus* by microtopographies (Sharklet™) was made by Chung et al. (2007). These authors suggested that the protruding features of the Sharklet™ pattern provided a physical obstacle, deterring the expansion of small clusters of bacteria, present in the recesses, into microcolonies. However, these experiments were conducted under static flow conditions only. Extrapolation of these observations for the entire channel bed suggests that the settlement of microorganisms was effected by flow conditions along with microwell geometric features. In fact, the microwell features influenced the distribution pattern of the resultant shear stress depending on the applied flow conditions which were evaluated by CFD analysis and are discussed in the next section.

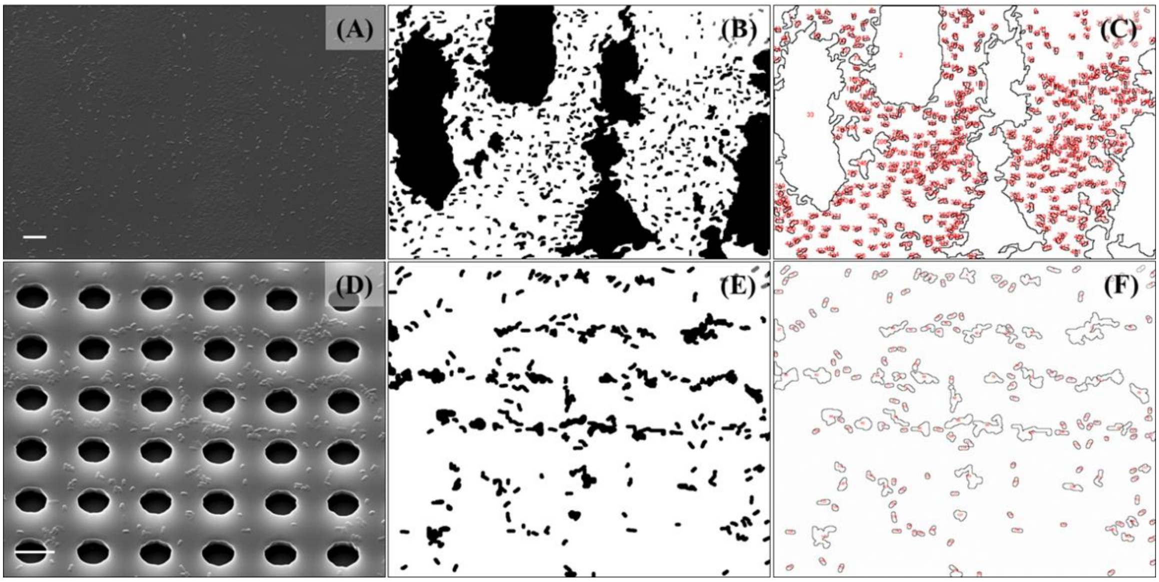

Figure 5.9: Group settlement inhibition by patterned surface in dynamic flow conditions (images were analysed using IMAGEJ software). (A) ESEM image of a plain surface, (B) areas of bacterial cluster formation, (C) surface coverage count, development of larger microcolonies (max. size 1468.16 μm^2); (D) ESEM image of D08S05 surface, (E) areas of bacterial settlement, (F) surface coverage count, mostly smaller microcolonies (max. size 33.43 μm^2); clusters on plain surfaces were 44 times larger than on a D08S05 surface. Scale bars = 10 μm.

5.5 Discussion

From the experimental results described in this study, it is evident that settlement of *E. coli* shows dependency on surface patterns and fluid flow conditions. The surface selection preference by *E. coli* was determined noticeably by ambient microfluidic environments. In flowing fluid conditions, fluid particles may undergo four fundamental types of motion or deformation: (1) translation (velocity), (2) rotation (angular velocity), (3) linear strain (extensional strain) and (4) shear strain (angular deformation). All these four types of motion or deformation usually occur simultaneously in a fluid domain depending on surface geometric features. The resultant hydrodynamic forces experienced by the microorganisms could have impacts on the overall settlement scenarios. Microorganisms, contrary to any inert particle, could respond actively according to the ambient hydrodynamic forces. In comparison to flowing fluid conditions, static fluid only exerts hydrostatic pressure P, which always acts inward and normal to the surface. For a fluid at rest, the stress tensor can be written as:

$$\sigma_{ij} = \begin{pmatrix} \sigma_{xx} & \sigma_{xy} & \sigma_{xz} \\ \sigma_{yx} & \sigma_{yy} & \sigma_{yz} \\ \sigma_{zx} & \sigma_{zy} & \sigma_{zz} \end{pmatrix} = \begin{pmatrix} -P & 0 & 0 \\ 0 & -P & 0 \\ 0 & 0 & -P \end{pmatrix} \tag{5.6}$$

So in a static fluid condition, microorganisms (in this study, *E. coli*) conform to hydrostatic pressure only and can settle easily on surfaces. Conversely, in flowing fluid conditions the hydrostatic pressure still acts inwardly normal to the surface; in addition viscous stresses exist. As the hydrostatic pressure does not contribute to the dynamics of the flow field for an incompressible flow without free surfaces, the stress tensor entirely depends on the velocity field of the fluid domain. The velocity field of a flowing fluid domain contributes to kinematic components, such as vorticity (from angular velocity), linear strain rate (due to acceleration/deceleration of the fluid particle) and shear strain rate (due to angular deformation of the fluid particle). Thus, the microfluidic environment of flowing fluid conditions is completely different from static fluid conditions. The velocity field is rapidly varying near to the microtopographies; it shows recirculation and steep fluctuations (Figures 5.10 and 5.11). The velocity components (u, v and w) near to microwells show spatial (advective) acceleration/ deceleration (Figure 5.11) and contribute to the total stress tensor as given in Equation 5.7. It should be noted that conservative values (ie half the control volume values next to wall boundaries) of velocity components are shown in Figure 5.11.

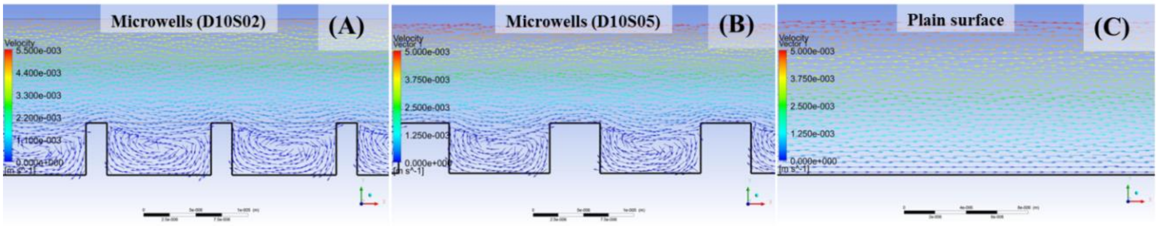

Figure 5.10: Velocity vectors on microwells and a plain surface (m s^{-1}). (A) D10S02 microwells array, (B) D10S05 microwells array, and (C) plain surface. Microwells developed recirculation zones in the depressions in contrast to a uniform velocity distribution on a plain surface. Flow direction from left to right.

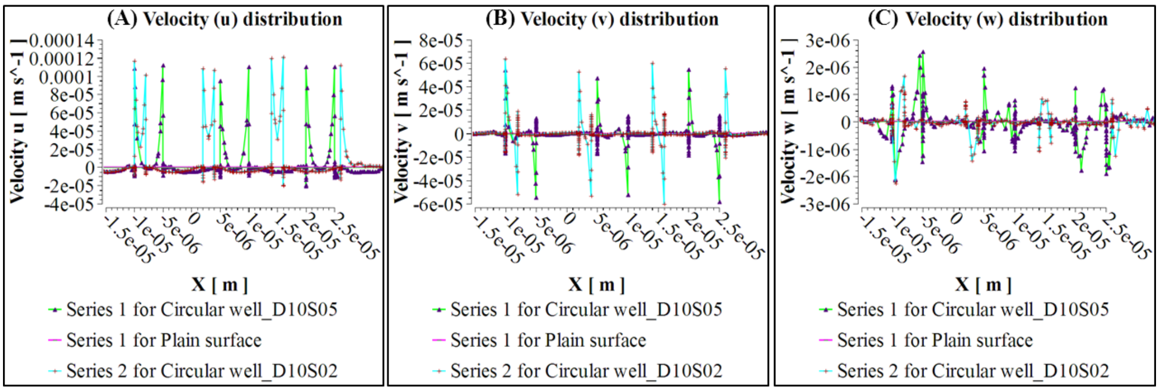

Figure 5.11: The velocity distributions on the microwells and a plain surface: (A) *u*; (B) *v*; (C) *w* components. Microwells developed spatial fluctuations (acceleration/deceleration) near to their edges in comparison to a uniform velocity distribution on the plain surface.

The components of the stress tensor of a flowing fluid can be expressed in terms of these velocity components and the pressure field. For a flowing fluid, the stress tensor can be written as:

$$\sigma_{ij} = \begin{pmatrix} -P & 0 & 0 \\ 0 & -P & 0 \\ 0 & 0 & -P \end{pmatrix} + \begin{pmatrix} \tau_{xx} & \tau_{xy} & \tau_{xz} \\ \tau_{yx} & \tau_{yy} & \tau_{yz} \\ \tau_{zx} & \tau_{zy} & \tau_{zz} \end{pmatrix} \qquad (5.7)$$

where the right-most part of the equation is the viscous stress tensor, τ_{ij}. For an incompressible Newtonian fluid with constant properties (as used in this study; water at 20 °C), the viscous stress tensor can be defined (Kundu and Cohen 2008) as:

$$\tau_{ij} = 2\mu\varepsilon_{ij} \tag{5.8}$$

where ε_{ij} is the strain rate tensor. The newly added viscous stress tensor in Equation (5.7) can be written as:

$$\tau_{ij} = \begin{pmatrix} \tau_{xx} & \tau_{xy} & \tau_{xz} \\ \tau_{yx} & \tau_{yy} & \tau_{yz} \\ \tau_{zx} & \tau_{zy} & \tau_{zz} \end{pmatrix} = 2\mu\varepsilon_{ij} = 2\mu \begin{pmatrix} \frac{\partial u}{\partial x} & \frac{1}{2}\left(\frac{\partial u}{\partial y} + \frac{\partial v}{\partial x}\right) & \frac{1}{2}\left(\frac{\partial u}{\partial z} + \frac{\partial w}{\partial x}\right) \\ \frac{1}{2}\left(\frac{\partial v}{\partial x} + \frac{\partial u}{\partial y}\right) & \frac{\partial v}{\partial y} & \frac{1}{2}\left(\frac{\partial v}{\partial z} + \frac{\partial w}{\partial y}\right) \\ \frac{1}{2}\left(\frac{\partial w}{\partial x} + \frac{\partial u}{\partial z}\right) & \frac{1}{2}\left(\frac{\partial w}{\partial y} + \frac{\partial v}{\partial z}\right) & \frac{\partial w}{\partial z} \end{pmatrix} \tag{5.9}$$

The symmetric second-order strain rate tensor (Equation 5.9) contains both linear strain rate (diagonal components) and shear strain rate (off-diagonal components). It can be noted that strain rate components depend entirely on velocity components for a constant fluid viscosity. For patterned surfaces, the near-surface microfluidic environment contains all the components of the strain rate tensor of Equation 5.9. On the other hand, for a fully developed two-dimensional Couette flow on a plain surface, it can be shown that the fluid particles are not accelerating in the flow field, neither by local acceleration (as the flow is steady), nor by advective acceleration (Çengel and Cimbala 2010). The component of this viscous stress tensor for a plain surface reduces to:

$$\tau_{ij} = \begin{pmatrix} 0 & \mu\frac{\partial u}{\partial y} & 0 \\ \mu\frac{\partial u}{\partial y} & 0 & 0 \\ 0 & 0 & 0 \end{pmatrix} \tag{5.10}$$

Equation (5.10) shows that for a plain surface with steady unidirectional flow, microorganisms experience shear strain at a constant rate arising from the variation in velocity with depth and fluid viscosity. This observation was also confirmed by CFD simulation of the fluid domain on a plain surface (Figure 5.12C). Conversely, for patterned surfaces, microorganisms experience differential strain rates (Figure 5.12A and B) which could be considered as key factors for disrupting the process of settlement.

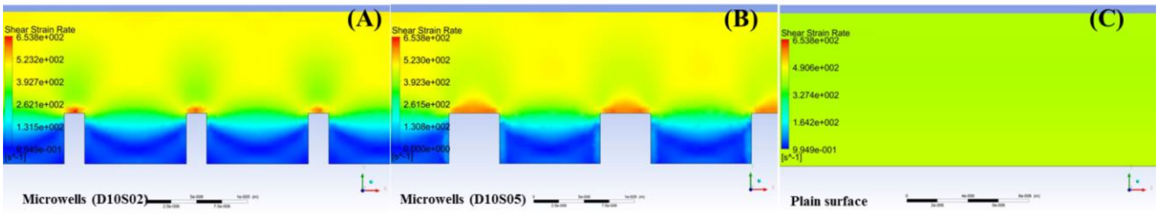

Figure 5.12: Shear strain rate distribution on microwells and a plain surface. (A) D10S02 microwells array, (B) D10S05 microwells array and (C) a plain surface. Differential strain rates can be seen in fluid domains of patterned surfaces (max. strain rate ~ 650 s^{-1}). In contrast, uniform shear strain rate (~ 500 s^{-1}) can be found in the entire fluid domain of a plain surface. Flow direction from left to right.

The quantitative rates of shear strain experienced by microorganisms can be examined further by modelling a swimming microorganism in static and shear flow conditions. Shear flow over patterned surfaces could be more crucial than flow over a plain surface due to specific interactions between the helical flagella and a fluctuating boundary surface. To explain complex scenarios, like circular swimming of an individual *E. coli* close to a surface, translational and rotational velocities of the organisms need to be considered along with proximity effects from solid boundaries (Lauga et al. 2006). In this study, a very simplified model was presented to examine the near-surface flow field developed by a self-propelled microorganism in static and dynamic flow conditions. For the cases presented here, rotational velocity was ignored. Firstly, a single microorganism was considered to move parallel to an infinite plane wall at a distance of 1 μm from the wall in a static flow condition (Figure 5.13A). *E. coli* was modelled as a rod-shaped bacterium 2 μm long × 1 μm diameter, with a 10 μm long × 0.5 μm diameter flagellar bundle (tail). The total length of *E. coli* was 12 μm, as described in Koch and Subramanian (2011). In the sphere–stick model by Cisneros et al. (2007), a morphologically similar swimming bacterium, *Bacillus subtilis* was considered as a spherical body (non-dimensional radius 0.1) with a cylindrical flagellum bundle (non-dimensional radius 0.02, length 0.4). Marcos et al. (2012) also modelled *B. subtilis* as a sphere of radius 0.8 μm attached to a left-handed rigid helix with axial length of 6 μm and diameter of 0.48 μm. Lauga et al. (2006) modelled *E. coli* using a similar approach with a spherical body attached to a single, left-handed rigid helix. In live cell modelling with a microwell device, Chen et al. (2012) considered leukaemic cells as spheres. Here, it should be noted that a similar microwell device was also used in this study to assess *E. coli* settlement. Microorganisms were considered as active immerged particles with a velocity of 30 µm s^{-1} in static flow conditions (Figure 5.13A). A transient flow analysis was performed for a total duration of 1.2 s with 0.1 s time steps. Similar considerations were also applied for shear flow (shear rate 500 s^{-1}) over plain and patterned surfaces with total time duration of 0.1 s and time steps of 0.01 s (Figure 5.13B–E). From these simulations, it was evident that in the dynamic flow condition, *E. coli* experienced a continuous microfluidic disturbance near to the microtopographic boundaries (Figure 5.13C and E). The strain rate experienced by a single microorganism in microwell areas was as high as ~ 650 s^{-1}. On a plain surface the maximum strain rate experienced by a microorganism on its body was ~ 10 s^{-1} in static and ~ 500 s^{-1} in dynamic flow conditions. The fluctuating strain rate developed on patterned surfaces could be sensed by microorganisms and make the surface appear unfavourable for settlement.

The collective (population) hydrodynamics (in case of group locomotion) could also influence the flow field substantially (Koch and Subramanian 2011; Guasto et al. 2012), but this aspect was not considered in this simplified modelling.

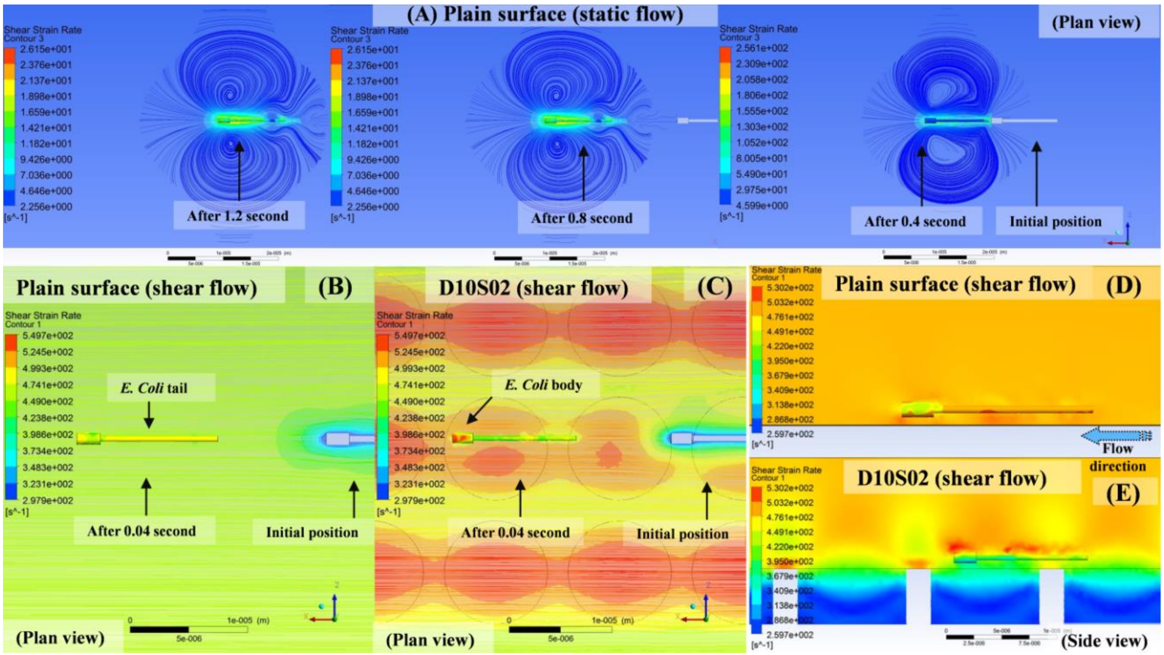

Figure 5.13: Streamlines of the velocity field and shear strain rate on *E. coli* under different conditions (s^{-1}). (A) *E. coli* swimming with self-flagellar propulsion (velocity 30 µms^{-1}) in a static flow environment (bacterial positions are shown after propulsion for 0.4,

0.8 and 1.2 s). Maximum strain rate experienced by a microorganism on its body is ~10 s^{-1}. Circular streamlines around a freely swimming rod-shaped bacterium diminish rapidly in the far field. (B) Bacterial locomotion in a shear flow on a plain surface; (C) on D10S02 microwells. (A–C) are plan views. (D) Shear strain rate distribution with bacterial locomotion on a plain surface; (E) on D10S02 microwells. (D–E) are side views of the fluid domain at 0.06 s of simulation. Velocity field was also shown with 50% transparency in the contour plot (A–C) to aid the visualization. Flow direction from right to left (B–E).

The distribution pattern of wall shear stress could also have an impact on settlement scenarios. Microorganisms settled preferably on plain surfaces; and CFD simulation of the plain surface indicated that the wall shear distribution was uniform throughout the area (Figure 5.14C and D). In contrast, microwell areas with varying shear stress patterns (Figure 5.14D) were rarely selected by *E. coli* for their initial settlement. It can be noted that the shape, spacing and size of the microwells influence the resultant shear stress distribution pattern, depending on the flow conditions applied. Circular shape microwells developed high shear bounded zones along the peripheries of the wells (Figure 5.14A and B), which could have a strong influence on the interruption of cell–cell signalling processes (quorum sensing). Quorum sensing (QS) is a cell-density-dependent activity where autoinducer molecules play a role to induce the expression of target genes to regulate a number of functions (Willey et al. 2008). Kirisits et al. (2007) showed that the hydrodynamic environment influences this QS process in the case of formation of a biofilm by *Pseudomonas aeruginosa*, which secretes acylhomoserine lactone as the autoinducer molecule. These authors showed that as the rate of fluid flow in a biofilm system increases, the signalling molecules wash out and the amount of biomass in the biofilm required for full QS induction of the population increases. *E. coli* also produces biofilms in response to a universal signalling molecule (AI-2), a product of the LuxS enzyme (Niu et al. 2013). *E. coli* harbours the Lsr regulatory pathway through which AI-2 controls biofilm formation and other phenotypes (Gonzalez Barrios et al. 2006; Li et al. 2007; Xavier et al. 2007). Since fewer *E. coli* cells were able to settle in the microwell bottoms (in high wall shear bounded isolated zones), it is likely that AI-2 molecules failed to reach the threshold level required to initiate biofilm formation. However, further research is needed to test this hypothesis. In relation to spacing between microwells, it was found that microwells arranged with smaller spacing (D10S02) developed higher shear stress at their edges (Figure 5.14A and B). The sharply fluctuating shear stress in a small area could present an unfavourable environment for bacterial settlement.

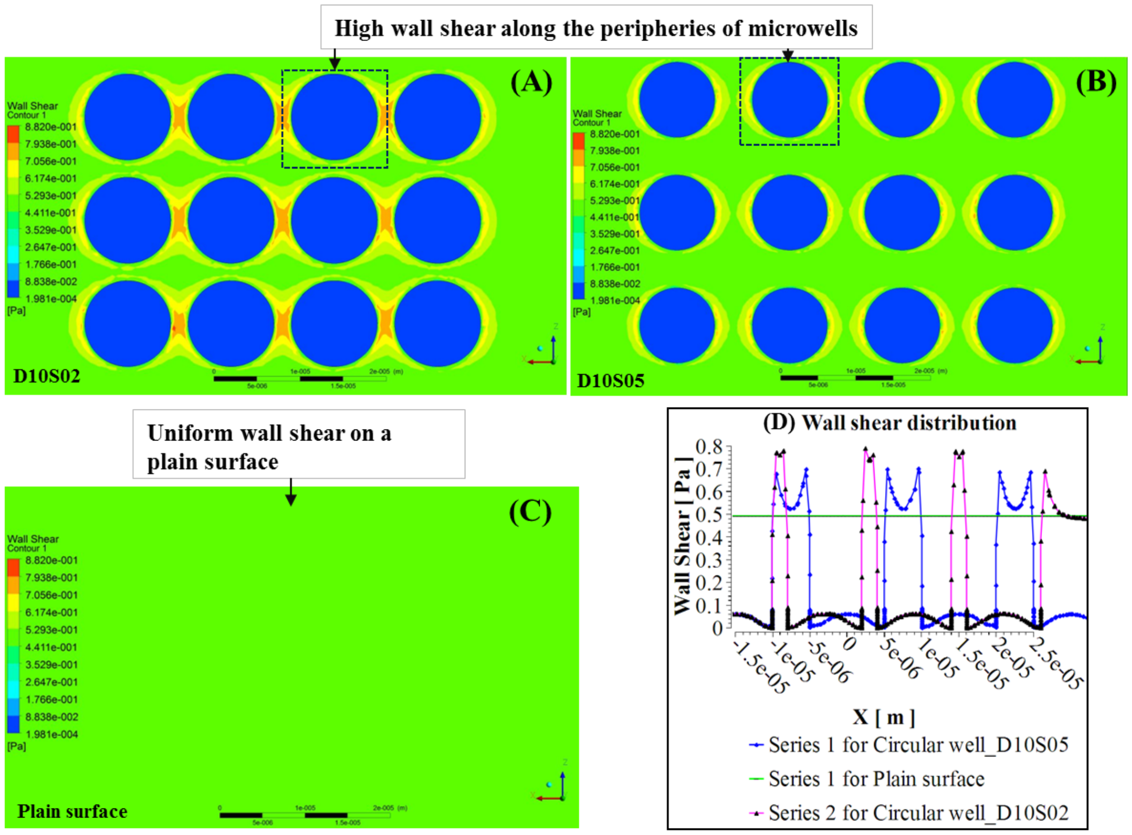

Figure 5.14: Wall shear distribution on microwells and a plain surface at the channel bed: (A) on D10S02 microwells array; (B) on D10S05 microwells array; (C) on the plain surface; (D) graph showing wall shear for D10S02, D10S05 and plain surfaces. Microwells develop high shear bounded zones in comparison to uniform shear distribution on a plain surface. Smaller spaced microwells (D10S02) developed higher shear at the edges than larger spaced microwells (D10S05).

The size of the microwells also exerted a noticeable influence in the settlement event as observed in the experiments. CFD simulation (Figure 5.15) of different sized microwells with constant spacing (2 µm) showed that the development and distribution of wall shear depended on the diameter of the microwells. Larger sized microwells (D10S02) develop higher shear at their edges and bottom than smaller sized (D05S02) microwells (Figure 5.15C). Here, it should be noted that feature dimensions of a patterned surface need also to be considered in relation to the body size of a microorganism (in this study, *E. coli* body size ~2–5 µm). Feature sizes smaller than the body size of the microorganism might not develop adequate microfluidic shear stress to inhibit settlement.

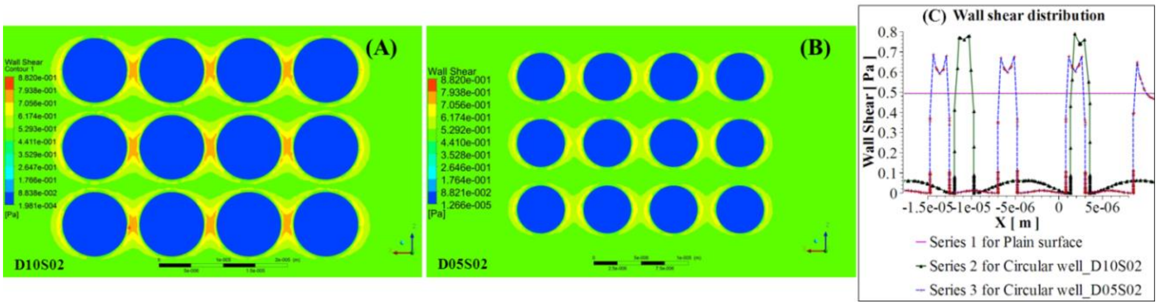

Figure 5.15: Wall shear distribution on different diameter microwells with constant spacing at the channel bed (Pa): (A) on D10S02 microwells array; (B) on D05S02 microwells array; (C) graph showing wall shear for D10S02, D05S02 and plain surfaces. Microwells with larger diameter (10 μm) developed higher wall shear stress in comparison to smaller 5 μm microwells and plain surfaces.

From this study, two related microfluidic conditions were deemed necessary for inhibiting the settlement of microorganisms: high shear bounded zone development and sharply fluctuating stress–strain rate. Pattern surfaces, like microwells, fragment group settlement (gregariousness) by developing high shear bounded zones along the peripheries of the microwells. Individual settlement of microorganisms could be restrained by the sharp fluctuations of stress– strain rate experienced by a microorganism along the entire path of its progression. It can be argued that the development of non-bounded high shear stress around protruding portions of the microstructures, such as pillars and ridges, might not be the most appropriate solution for biofouling control in consideration of the microfluidic environment. An enclosed pattern (eg circular, rectangular or hexagonal wells) developing high shear bounded isolated areas, could be considered more effective for biofouling control in a flowing fluid environment (see more details in Chapter 7). However, further research is needed to test this hypothesis. The antifouling efficacy of similarly patterned microtopographies depends on the intensity of the resultant wall shear and strain rates. Structural features with less spacing were more AF in this respect.

5.6 Conclusion

The present study demonstrates that microorganisms on patterned surfaces experience a complex microhydrodynamic environment, which includes differential strain rates, fluctuating velocity distribution and recirculation, and a distribution pattern of wall shear that develops in response to the structural pattern of the surfaces. Any surface, patterned or plain, develops a particular microfluidic environment under specific fluid flow condition. The observed AF properties of patterned surfaces have shown a dependency with the near-surface fluid dynamics. The characterisation of any irregular/patterned surfaces based on AF efficacy is believed to be complex, involving a number of interrelated parameters, including biological factors, presence of other organisms, surface chemistry, nutrient supply and ambient fluid properties. This study considered only the predefined microstructure-based patterned surfaces in a high flow velocity environment which could have disrupted different biological activities of microorganisms (including its swimming) along with their early settlement. In the present study, the near-surface microfluidic conditions were found to be the determinant factors of the AF behaviour shown by patterned surfaces. CFD simulations also showed that the fluctuating stress-strain rates of microhydrodynamics affected the natural swimming trajectory a motile organism. From this point of view, it can be hypothesized that a microfluidic disturbances developed on a patterned surface could affect the self-propelled microorganisms significantly, and thus also could affect the subsequent stages of biofilm development. To prove this hypothesis, it is very important to investigate the dynamic interactions (ie effect on swimming) of a motile bacterium (eg *E. coli*) with microtopographies in relation to the initial settlement process. The next chapter (Chapter 6) will present the details of another microbiological experiment with a re-designed test set-up, which investigated the dynamic stability of *E. coli* on a single array of microwells. The test results were also compared with the trajectories of *E. coli* over a conventional plain surface and CFD simulations.

Chapter 6

6 Dynamic stability of microorganisms on patterned surfaces

6.1 Contributions

A second microbiological experiment was conducted to identify the motility patterns of individual bacterial cells over plain and patterned surfaces. The cell bodies were subjected to controlled hydrodynamic conditions at micro-scale. The experimental set-up was re-designed from the previously described experiments (Chapter 5), including a single array of microwells instead of a series of microwell arrays on the microchannel bed and an integrated video microscopy system with time-lapse imaging module. CFD simulations were also performed to characterize the individual cell trajectories over plain and microwell-based patterned surfaces.

The content of this chapter has been published in ‘Biofouling: The Journal of Bioadhesion and Biofilm Research’ journal. It is presented here with small modifications.

Halder, P. Nasabi, M. Jayasuriya, N. Shimeta, J. Deighton, M. Bhattacharya, S. Mitchell, A. and Bhuiyan, MA. 2014. An assessment of dynamic stability of microorganisms on patterned surfaces in relation to biofouling control. Biofouling: Vol. 30: 695-707.

6.2 Introduction

Chapter 5 summarized that the microstructure-based patterned surfaces are showing transitory antifouling (AF) capabilities due to the microfluidic disturbances developed on them. Experimental results and CFD simulations also suggested that the surface patterning may generate altered hydrodynamics which makes the early stages of biofilm formation by microorganisms on these surfaces more difficult. It is speculated that the fluctuating stress–strain rates and enclosed wall shear stress pattern developed on patterned surfaces disrupt the stability of microorganisms. However, still questions arise: why and how the swimming dynamics of an individual organism changes near to the solid boundaries? Is the swimming dynamics different at surface-distant swimming from that at near-surface? How microtopographies alter the natural motility of swimming microorganisms? The answers of these questions could be essential for optimising the microstructure-based AF patterned surfaces. Several studies (see Chapter 2) suggested that the swimming kinematics and trajectories of microorganisms can be altered by the presence of nearby boundaries. The AF efficacy showed by microtopographies is more a hydromechanical phenomenon than a biological/ physico-chemical process in this respect. Thus, the settlement (ie attachment) of microorganisms, their locomotion on plain and patterned surfaces and the near-surface microfluidic environment are the main interest of investigation of this study. This chapter will combine both the experimental and computational aspects to better understand the interaction between a motile microorganism and a patterned surface.

The trajectories of *Escherichia coli* (K-12) cells across a patterned surface of a microwell array within a microchannel-based flow cell system were assessed with a time-lapse imaging module in the demonstrated experiment in this chapter. The microwell array was composed of 256 circular wells, each with diameter 10 µm, spacing 7 µm and depth 5 µm. The dynamics of *E. coli* over microwell-based patterned surfaces were compared with those over plain surfaces and an increased velocity of cell bodies was observed in the case of patterned surfaces. The swimming dynamics of an individual *E. coli* cells were also investigated at two different fluid depths.

The goal of this study was to investigate the dynamic stability of *E. coli* on a prefabricated microwell-patterned surface compared with a conventional plain surface. The main focus was how the complex microfluidic environment developed on patterned surfaces disrupted the settlement of bacterial cells.

6.3 Materials and methods

6.3.1 Experimental design and set-up

This test set-up is analogous to that used in experiments described in Chapter 5. However, it was re-designed from the previous one with a single array of microwells to observe bacterial motility under controlled hydrodynamic conditions. The flow cell was combined with light microscopic (LM) imaging and a time-lapse module to observe and quantify every stage of locomotion of *E. coli* under conditions of continuous flow. Leica Application Suite (LAS®) multi-time imaging software (LAS MultiTime, Leica Microsystems Pty Ltd, Sydney, Australia) gave real-time monitoring and sequential image acquisition at specified time intervals. The dynamic stability of individual cells on plain and patterned surfaces was compared concurrently under the same conditions of flow and cell culture. The fluid flow of the microchannel was controlled precisely (in terms of shear rates) with a digital drive and microbore tubing system. The culture medium and most of the flow cell system were autoclaved. Heat-sensitive components were sterilised using a method adapted from Fisher and Petrini (1992). *E. coli* (ATCC® 25922™) was induced in the flow cell after inoculating into a mixing chamber. Details of the inoculation, sterilisation procedures and nutrients can be found in the previous chapter (Chapter 5). The entire microchannel system was enclosed to minimise the possibility of contamination.

6.3.2 Microchannel flow cell system

Bacterial motility was observed in a rectangular polydimethylsiloxane (PDMS) microchannel as described in Chapter 5. The channel bed was modified for this new experiment, patterned with a single array of circular wells (microwells, depth 5 µm). The prefabricated microwell array was (272 × 272) μm^2, composed of microwells with 10 µm diameter and 7 μm edge to edge spacing (indicated as D10S07). Previously described experiments (in Chapter 5) showed that the geometric feature sizes of a prefabricated microtopography need to consider the body size of the microorganisms for higher AF efficiency. It was also found that feature size smaller than the cell body size showed negligible effect on settlement of *E. coli*. Conversely, other studies (eg Scardino et al. 2006; Sweat and Johnson 2013) showed that substantially larger features than the cell body size can provide physical protection to the settling cells against hydrodynamic forces. Hence, in this study the microwell configuration D10S07 was chosen to be slightly larger than the body size of *E. coli* (~2-5 μm). The microchannel was connected with a 'once-through' flow tube, fed from a mixing chamber as shown in Figure 6.1. The various components of the test set-up were connected by platinum-cured silicone tubing (0.25 mm Microbore Tygon® E-Lab tubing, L/S® 13, 16, Masterflex®). The flow of nutrients into the mixing chamber and flow rate into the flow cell were controlled by a high precision peristaltic pump, mounted with multi-channel pump head (Masterflex®, L/S® digital drive with L/S® four-channel pump head). The six rollers of the pump head ensured delivery of low-pulsation synchronous flow. The inflow rates of the sterile culture medium at the mixing chamber and the inlet of the microchannel were the same (0.02 μl s^{-1}). Two glass flow breaks and one bubble trap were placed in the same order as described in the previous experiment (see Chapter 5). The flow cell was positioned on the stage of an inverted light microscope (Carl Zeiss, Axiovert 25c) for the continuous monitoring of bacterial motility.

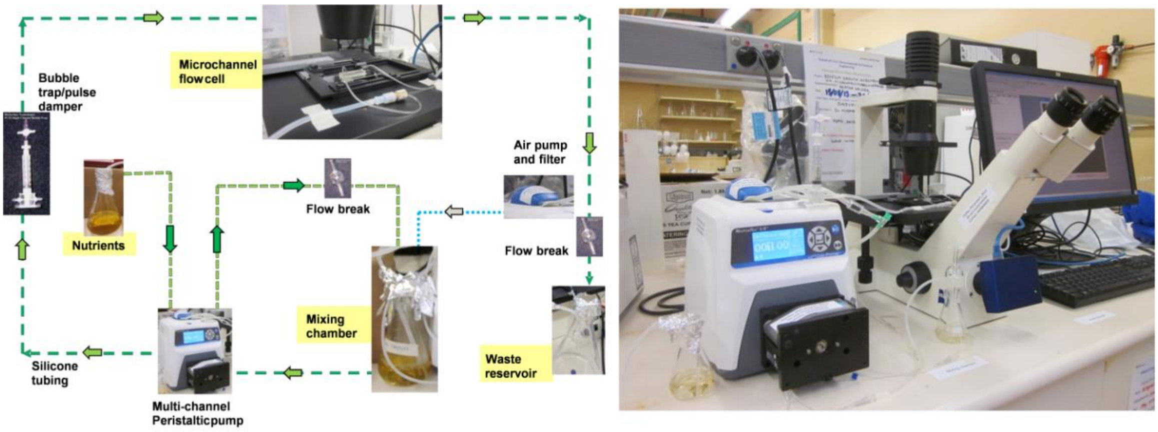

Figure 6.1: Schematic of experiment (left) and laboratory set-up (right) for observing bacterial motility on patterned surface.

6.3.3 Flow cell fabrication

The flow cell device consisted of two components: a microwell array fabricated on a glass slide using an epoxy-based negative photoresist SU-8 2005 (MicroChem Corp., Newton, MA, USA) and a microchannel made of PDMS. The microwell array (16 × 16) was fabricated on a surface area of (272 × 272) μm^2. The PDMS microchannel was then placed over the microwell array to form a closed rectangular channel with one inlet and one outlet at the ends (Figure 6.2). The steps involved in the flow cell fabrication can be found in detail in Chapter 4.

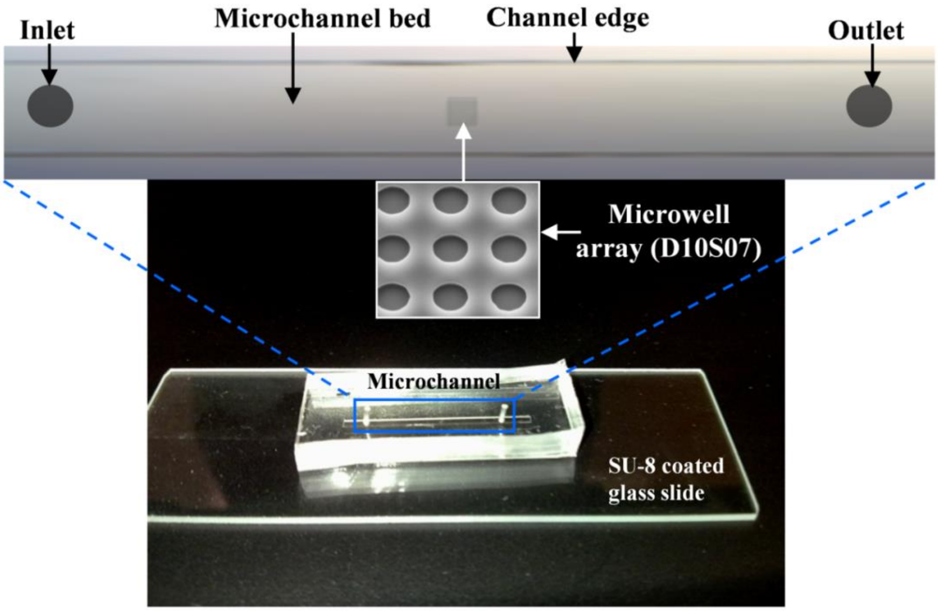

Figure 6.2. Microchannel made from PDMS with array of microwells (patterned surface) fabricated on a SU-8 coated glass slide. A zoom-in view of the microchannel bed shows array of microwells with D10S07 configuration.

6.3.4 Flow cell hydrodynamics

The fluid velocity was carefully controlled to obtain sequential images of bacterial motility. As this study aimed to investigate the motility of individual bacterial cells in relation to fluid–structure interactions, a very low flow rate was applied (0.02 $\mu l\ s^{-1}$) for this experiment. The critical strain rate for suppressing the self-propulsion of *E. coli* is >

10 s^{-1}, as suggested by Hill et al. (2007). The selected flow rate ensured that the induced hydrodynamic forces did not manipulate the self-propulsion of cells significantly. Instead, a tractable path line of a bacterium could be identified within the field of view (FOV) of the objective lens (40 ×) and compared for both plain and patterned surfaces using a time-lapse imaging system. The given flow condition was necessary to propel and track individual cells as they crossed the smooth surface and then encountered the patterned surface without disrupting their self-propulsion capability significantly. The developed wall shear stress at the channel bed was ~ 0.01 Pa. The calculated Reynolds number, hydrodynamic entry length and the shear strain rates were ~ 0.03, 0.3 μm and 10 s^{-1}, respectively. The steps involved in these calculations can be found in Chapter 5.

6.3.5 Image analysis

For the cell motility experiment, real-time locomotion of bacteria was monitored continuously using LM (phase contrast) and a digital microscope camera (Leica DFC310 FX). The video microscopy system was supported by a Leica application suite (LAS MultiTime® module) with time stamping option. A total of seven video clips (labelled as Observations 1–7) were obtained using the video microscopy system. The duration of each video clip was 20 s with a 1 s interval of time stamping. Still images were captured and saved separately at every second from the acquired video clips. The frame rate was ~20 frames per second (fps) for most of the video clips. Thus, it was easy to retrieve suitable still images from the series of frames embedded in the video clips. Figure 6.3 shows some of these still images, identifying the positions of individual *E. coli* at different time points. In total, 147 still images (ie 21 images × 7 video clips) were retrieved from the acquired clips. All still images were analysed further to identify bacterial swimming trajectories using IMAGEJ software (http://rsbweb.nih.gov/ij/).

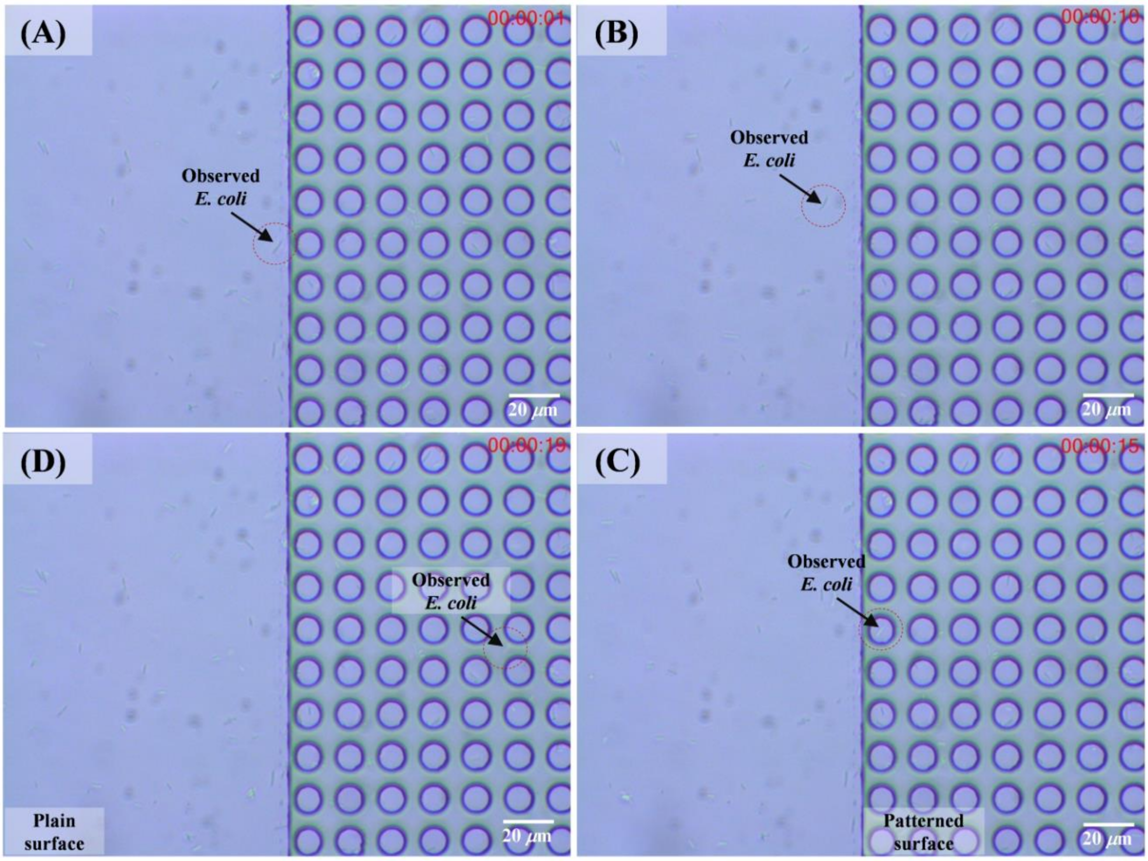

Figure 6.3: LM images (still images) showing the positions of individual *E. coli* at different time intervals (acquired from video clips): (A) over the adjacent plain surface at 1 s; (B) over the plain surface at 10 s; (C) over the patterned surface at 15 s; (D) over the patterned surface at 19 s. Flow direction from left to right.

Images were also taken using an environmental scanning electron microscopic (ESEM; FEI Quanta 200, FEI Company, Hillsboro, OR, USA) to characterise the microwell array in relation to the elevation difference from the adjacent plain surface (Figure 6.4). All ESEM images were taken at 30° tilt to get a clear view of the elevation difference and microwell depth (5 µm).

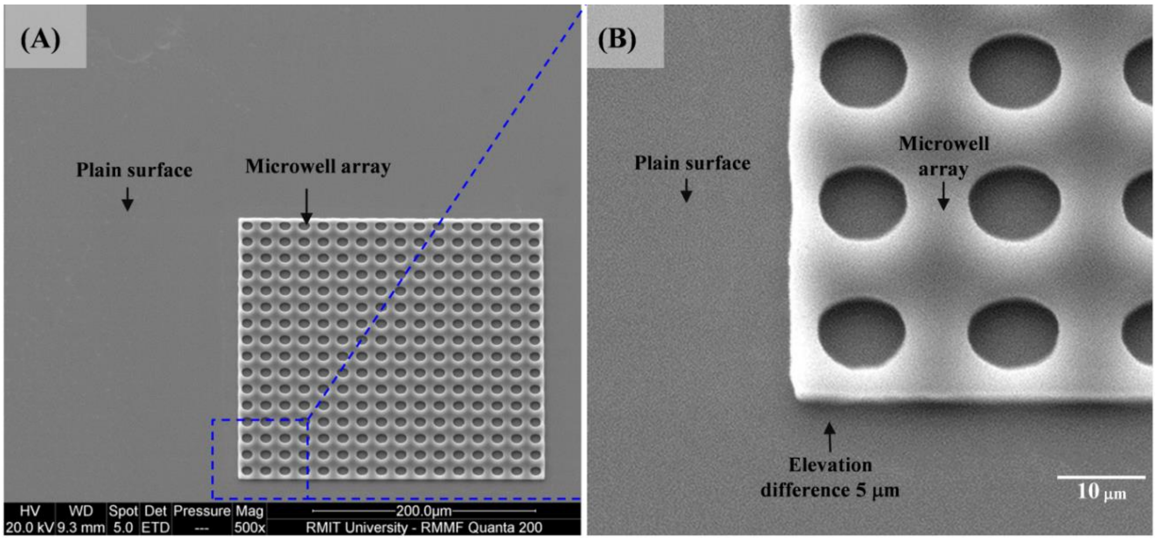

Figure 6.4: Elevation difference in plain and patterned surfaces: (A) ESEM image shows protruded microwell array (image was taken at a 30° tilt to get a clear view of the elevation difference); (B) a zoom-in view of microwell array showing change in elevation from plain to microwells (5 µm).

To characterise the effect of solid boundaries on cell dynamics, it was essential to find out at what depth the bacterial cells were swimming. It was difficult to assess the swimming depth using LM as cells changed focal planes very frequently. In this study, swimming depth was assessed based on the focal plane set-up of the microscope at a known depth. For example, to observe cells on the plain surface at a higher swimming depth, the focal plane of the microscope was adjusted to the top of the microwell array (Figure 6.5, see also Figure 6.4). This ensured that the observed bacterium (within LM field of view) was swimming at a distance ~ 5 µm above the bottom surface.

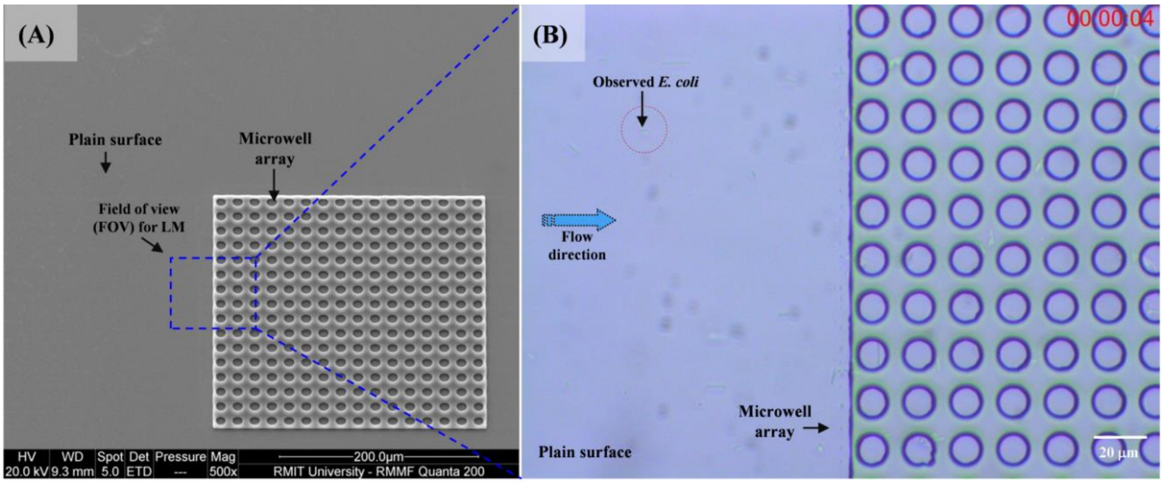

Figure 6.5: Focal plane and FOV selection to observe bacterial locomotion at a greater distance above the surface: (A) ESEM image shows protruded microwell array (elevation difference between plain and patterned surfaces is 5 µm) and the FOV location for LM imaging; (B) LM image shows flow direction and *E. coli* trajectory in the FOV of the LM.

6.3.6 Statistical analysis

Statistical differences between the swimming velocities of cells over plain/patterned surfaces were analysed using a two-way ANOVA followed by the Tukey’s multiple comparisons test. Here, two different factors were considered, which included the surface patterning (plain/pattern) and the swimming depths (1 µm/5 µm). Parametric t-tests (paired) were also conducted for all identified bacterial cells without discriminating them in relation to swimming depths to see the effect of surface patterning only on cell dynamics. In all tests, statistical differences were considered significant at the 95% confidence level. Bacterial cells were also considered independent for all statistical analyses. All these analyses were performed using GraphPad Prism software (version 6.00 for Windows; GraphPad Software, La Jolla, CA, USA; www.graphpad.com).

6.3.7 CFD analysis with patterned surfaces

To investigate the effects of solid boundaries (plain/patterned) on the swimming trajectory and the dynamic stability of *E. coli*, a commercially available CFD software package (ANSYS CFX, Version 14.5, ANSYS Inc., Canonsburg, PA, USA) was applied to calculate flow fields around the moving bacterial cells. The bacteria were modelled as immersed solids near to the surface and the complex microfluidic environment was solved using a finite volume method and described in details in Chapter 3.

The entire channel was simulated initially to find the developed wall shear stress (~0.01 Pa) on the plain surface, which was validated by the analytical solution described in Chapter 5. In this regard, the inlet flow rate was set at 0.02 µl s^{-1} and the channel walls were considered plain surfaces with no-slip boundary conditions. Other studies (Lee et al. 2008; Tovar-Lopez et al. 2010; Chen et al. 2012) also applied no-slip boundary conditions for the channel walls to simulate the flow field in a microchannel using CFD. Wall shear stress was ~ 0.01 Pa at the maximum area of the channel bed (Figure 6.6A). To save computational time, the fluid domains were subsequently considered differently in the two sets of simulations for plain and patterned surfaces. In both cases, a segment (100 µm wide, 100 µm deep and 150 µm long) of the entire microchannel was taken as a computational domain. For patterned surfaces, 5 µm circular wells were additionally included in the channel bed. The flow condition around a bacterium was simulated by an immersed solid placed in this computational domain (Figure 6.6B).

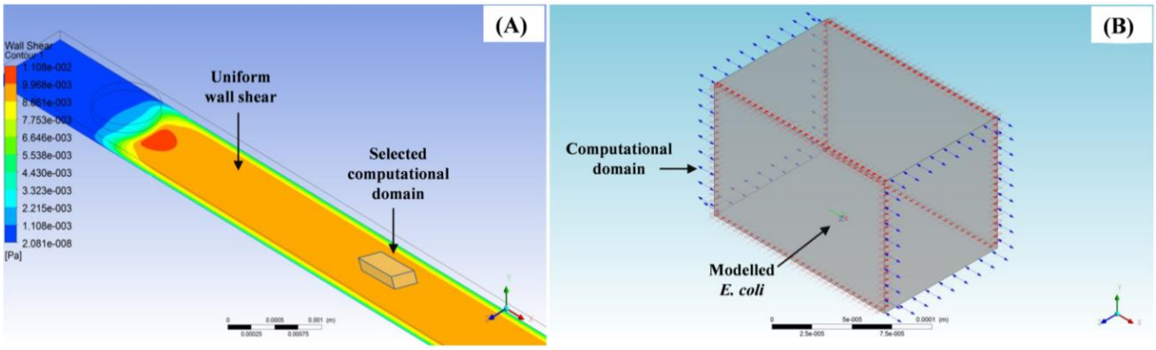

Figure 6.6: CFD simulation of microchannel: (A) Simulation of entire microchannel shows that the wall shear stress is ~0.01 Pa at the maximum area of the plain surface bed (a segment of the whole microchannel was selected for the later stage simulations); (B) selected computational domain, showing the position of a modelled *E. coli* cell near to the channel bed.

To model a self-propelled microorganism (an individual cell), both the translational and rotational velocities of the organism were considered. *E. coli* was modelled as a rod-shaped bacterium with dimensions remaining the same as described in Chapter 5. It was considered that the modelled *E. coli* would swim parallel to an infinite plain wall at three different distances of 2, 5 and 15 μm from the bottom in static and flowing fluid conditions. The different swimming depths were taken to see the effects of wall distance on bacterial motility. *E. coli* moved with a translational and rotational (flagellar bundle) velocity of 30 μm s^{-1} and 100 Hz (62.83 radian s^{-1}) respectively, as found by Berg (2004) and Darnton et al. (2010). A transient scheme (second-order backward Euler) with an immersed solid solution technique was taken for a total duration of 1 s with 0.01 s time steps. A high resolution scheme (HRS) was selected to solve convection terms of the Navier–Stokes equations. Details of the numerical procedures used in this study can be found in Chapter 3.

A grid independence analysis (mesh convergence) was conducted by increasing the number of nodes and calculating the maximum wall shear for all the cases. Figure 6.7 shows the percentage difference between the maximum wall shear calculated for subsequent refinements (relative error) as a function of the number of nodes. Plots are shown for fluid domains with plain boundaries and immersed solids (model bacterium with self-velocity of 30 μm s^{-1}) at distances of 2, 5 and 15 μm from the bottom. Mesh convergence was assumed satisfied when variation in the maximum wall shear values was < 5%, although a finer mesh was used to have a better description of the complex flow-field around a moving microorganism. Mesh statistics showed that in all cases > 3 million nodes were generated. Mesh elements were mostly hexagonal (94% hexahedrons and 6% prisms). The mesh orthogonal quality was in the range of 0.67–0.99 (acceptable value ≥ 0.1) and skewness was in the range of 3.99E-04–0.6 (acceptable value ≤ 0.8).

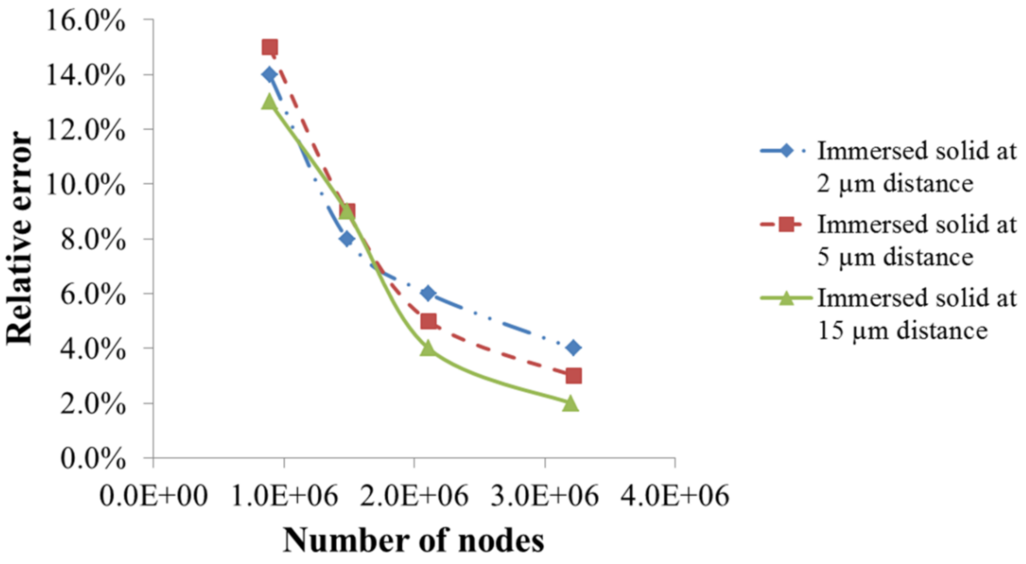

Figure 6.7: Mesh convergence analysis of fluid domains with plain boundaries and immersed solids (model bacteria) at 2 μm, 5 μm and 15 μm distances from the bottom.

6.4 Results

The motility pattern of cells changed with the nature of the nearby solid boundaries (ie plain or patterned). In most cases, video microscopy indicated that *E. coli* cells had more dynamic control over plain surfaces than over patterned surfaces. The trajectory of an individual bacterium, which could be identified over both plain and patterned surface regions, showed that a cell remained for a longer time period over a plain surface than over a patterned surface. Generally it was observed that circular swimming, the pattern described by Lauga et al. (2006), was more common over the plain surface. In contrast, less curved swimming trajectories of cells were observed over the patterned surface.

Still images captured from video clips were analysed for positions and velocities of cells using IMAGEJ software. Firstly, an arbitrarily selected Cartesian coordinate was taken on the starting image (ie image at 0 s) as a reference point and then the following images were analysed in relation to that reference point. For example, in Observation 1 (Cell 1), the initial position (at 0 s) of the observed microorganism was at 36 μm and 60 μm in the x and y axes, respectively (Figure 6.8A). All distances were measured from the reference coordinate axes (0, 0) and then plotted into a graph to obtain a motility path line for individual cells (Figure 6.8B). Following these steps, three different sets of data were generated from three individual cells in each observation. In total, 21 different motility path lines (ie 3 cells × 7 observations) of 21 cells were identified (Table 6.1).

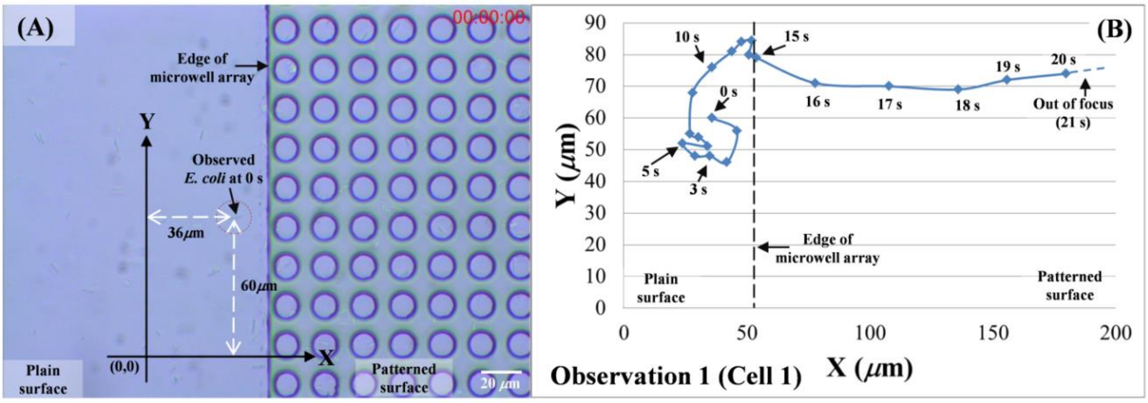

Figure 6.8: Individual swimming trajectories of *E. coli* on plain and patterned surfaces: (A) reference coordinate (0, 0) set-up in LM image; (B) graph showing an individual *E. coli* path line at different time intervals. *E. coli* cells showed a circular motion on the plain surface and stayed longer than on the adjacent patterned surface.

Table 6.1: Comparison of bacterial locomotion and residence time over different surfaces at different swimming depths

Approx. swimming depth	**Observation labels**	**Individual cell velocity (μm sec^{-1})**						**Mean velocity ± SD (μm sec^{-1}) {Avg. residence time (%)}***	
		Plain			**Pattern**			**Plain**	**Pattern**
		Cell 1	Cell 2	Cell 3	Cell 1	Cell 2	Cell 3		
1 μm	Observation 1	9.95	18.22	11.36	26.32	31.18	17.30	17.26 ± 6.85 {62.52}	25.51 ± 7.75 {37.48}
	Observation 2	11.95	30.61	30.75	14.23	39.17	36.41		
	Observation 4	15.62	13.95	18.96	31.21	14.80	26.40		
	Observation 5	7.88	16.00	21.20	23.85	17.26	32.93		
	Observation 6	12.30	23.01	17.11	21.02	28.18	22.30		
5 μm	Observation 3	32.67	29.94	42.28	41.66	32.50	50.71	31.22± 6.07 {60.40}	37.19 ± 9.82 {39.60}
	Observation 7	24.18	29.31	28.92	21.70	35.50	41.05		

* The average residence times (%) are shown inside the bracket {}.

Residence time on plain and pattern surfaces was averaged from the datasets obtained and expressed as a percentage of the total time (Table 6.1). Firstly, individual cell residence times were calculated from individual observations. For example, in Observation 1 (Cell 1), the observed individual cell (as shown in Figure 6.8B) remained for 14 s on the plain surface compared with only 6 s on the patterned surface. So, the residence time was calculated as 75% on the plain surface and 25% on the patterned surface. Similarly, residence times for Cells 2 and 3 of Observation 1 were calculated (Cell 2: 77.44% and 22.56%, Cell 3: 57.27% and 42.73%, time on the plain and patterned surfaces, respectively). Following these steps, the residence time (%) was calculated for all identified cells and the average values were taken based on swimming depths and surface patterning. The individual cell velocity was determined from the distance travelled by *E. coli* cells divided by the associated residence time. An average cell velocity of three different cells was obtained from each observation at particular depths for a comparison of cell dynamics over surfaces (see details in Table 6.1).

Table 6.1 shows that the mean swimming velocities of cells on the plain surface were lower in all the cases than on the patterned surface. When the swimming depth was higher (~5 μm), the mean difference (8.25 μm s^{-1}) was comparatively lower than that (5.97 μm s^{-1}) of the surface-close swimming (~1 μm) in relation to the surface patterning. The lowest mean difference (5.71 μm s^{-1}) was observed in the case of cells over patterned surfaces at 1 μm depth compared with plain surfaces at 5 μm depth. The motility patterns were also less curved at a greater distance (~5 μm) above the surface (general observation). For example, a comparison of the motility pattern in Observations 2 and 3 (Cell 1) clearly indicated that at surface-close swimming, *E. coli* showed a circular trajectory (Figure 6.9A), while at a greater distance (~5 μm) less curved trajectories were observed regardless of the surface pattern (Figure 6.9B).

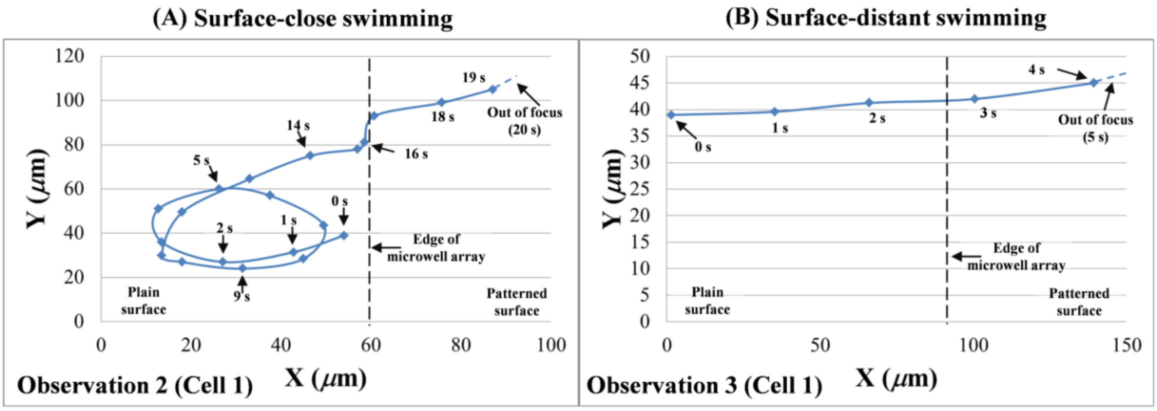

Figure 6.9: Individual swimming trajectories and residence time of *E. coli* over plain and patterned surfaces at different swimming depths: (A) Observation 2, at a close distance from the surface (~ 1 µm); (B) Observation 3, at a greater distance from the surface (~ 5 µm).

Table 6.1 also shows that the residence time was generally higher on the plain surface than on the patterned surface. Cells remained on plain surfaces for a longer time period than on patterned surfaces (62.52% and 37.48% of the total observed time on plain and patterned surfaces respectively, at ~1 µm swimming depth). Figure 6.9 shows an example of motility and cell residence time for an individual cell over surfaces. In Observation 2 (Cell 1) the individual cell remained on a plain surface for 16 s compared with 2 s on a patterned surface (Figure 6.9A). The lower residence time on patterned surfaces indicated that bacteria were out of focus more frequently at some points due to moving to the higher fluid strata.

The mean swimming velocities (as shown in Table 6.1) of cells were further analysed statistically to find out if any significant difference existed among them. The 2-way ANOVA analysis ($p = 0.05$) followed by Tukey's multiple comparisons test showed that the cell velocities were significantly different over a plain surface compared with a patterned surface ($p < 0.05$) at a distance of 1 µm from the bottom surface (Figure 6.10A). On the other hand, the cell velocities showed no significant difference at a higher swimming depth (5 µm) in relation to the bottom surface patterns (ie plain *vs* patterned). This result indicated that the surface pattern can influence the cell dynamics only at a closer distance. Multiple comparisons also showed that cell velocities over the plain surface at a distance of 1 µm were significantly different from cell velocities over the plain ($p < 0.01$) and patterned ($p < 0.0001$) surfaces at a distance of 5 μm. This result was consistent with the conventional law of fluid dynamics that fluid velocity increases at a greater distance from the bottom solid boundaries. However, cell velocities over a patterned surface at a distance of 1 μm were not significantly different from cell velocities over a plain surface at a distance of 5 μm. Physically, this means that cells immediately over a patterned surface attained swimming velocities similar to their higher depth swimming.

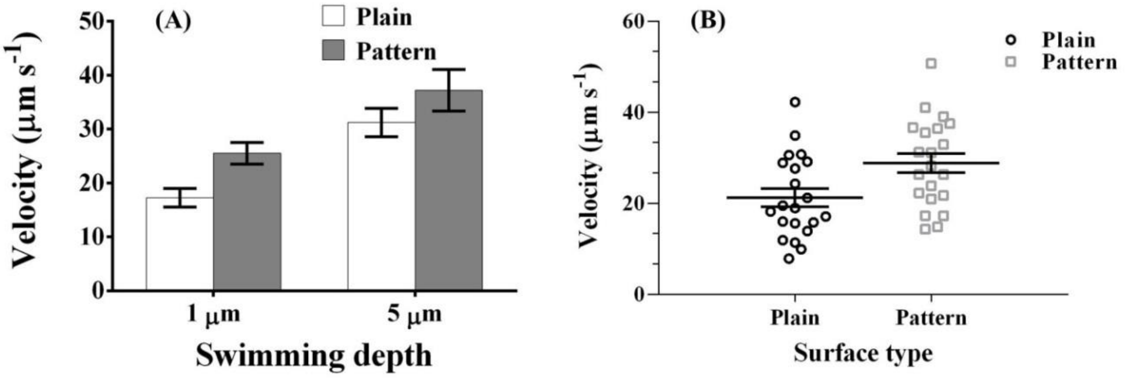

Figure 6.10: Comparison of mean swimming velocities of *E. coli* cells on plain and patterned surfaces. (A) Comparison of different surface patterns and swimming depths, analysed by 2-way ANOVA followed by Tukey's multiple comparisons tests. (B) Comparison of different surface patterns only (swimming depths were pooled), analysed by paired t-test. Refer to text for statistical results. Each datum point represents mean velocities ± SEM.

Another comparison of cell velocity was conducted using parametric t-tests (paired), where all observations were taken into account without considering the swimming depth separately ($n = 21$, values were normally distributed). The test result showed that the cell velocities were significantly different over plain compared with patterned surfaces ($p < 0.0001$). The mean cell velocities were 21.25 (SD: 9.15, SEM: 1.99) μm s^{-1} and 28.84 (SD: 9.77, SEM: 2.13) μm s^{-1} on plain and patterned surfaces, respectively (Figure 6.10B).

From all these results it was clear that the swimming speed of *E. coli* decreased closer to the surface and increased with an increase in swimming depth. The results also showed that cell velocity over a plain surface could increase in close proximity to the surface while crossing over the pattern due to the presence of a particular type of surface patterning (eg microwells, as used in this study).

6.5 Discussion

From the experimental results it is evident that the dynamic stability of *E. coli* shows dependency on surface patterning. Furthermore, the swimming depth (distance from the boundary wall) determines the degree of interaction between microorganisms and solid boundaries. Generally, the surface selection preference of *E. coli* is based on its ambient microfluidic environment. Studies by Rosehahn and Sendra (2012) and Heydt et al. (2012) showed that microorganisms (algal spores) need to reduce their swimming speed for surface selection and temporary settlement. However, in the case of a patterned surface with a microwell feature, *E. coli* cells attained higher velocities and periodic microfluidic disturbances while crossing over the microwell array.

In a viscous dominated zone, convection is almost negligible and hence a motile rod-shaped bacterium rotates its body (including the flagellar bundle) continuously for locomotion. Bacterial locomotion in viscous liquid has been described extensively (Ramia et al. 1993; Lauga et al. 2006; Berke et al. 2008; Lauga and Powers 2009; Guasto et al. 2012). From simulations of bacterial motility near a plain surface, it is clear that fluid particles around submerged bodies (*E. coli*) are driven by viscous forces only. In the case of a patterned surface, kinematic components are more active in the surrounding fluid domain. These components include vorticity (from angular velocity), linear strain rate (due to acceleration/deceleration of the fluid particle) and shear strain rate (due to angular deformation of the fluid particle). The near-surface boundary effect on the velocity field was compared through CFD simulations for a rod-shaped bacterium swimming at a distance 2 μm (from body centre) on plain and patterned surfaces in both static and dynamic flow conditions (Figure 6.11). These four cases are further delineated by vector field (Figure 6.12A–D) and graph (Figure 6.12E). The velocity vectors varied rapidly around the body of the bacterium modelled, and developed recirculation zones inside the microwells for both static and dynamic conditions (Figure 6.12B and D). In the case of a plain surface, the velocity vectors were parallel to the locomotion of the bacterium (Figure 6.12A and C).

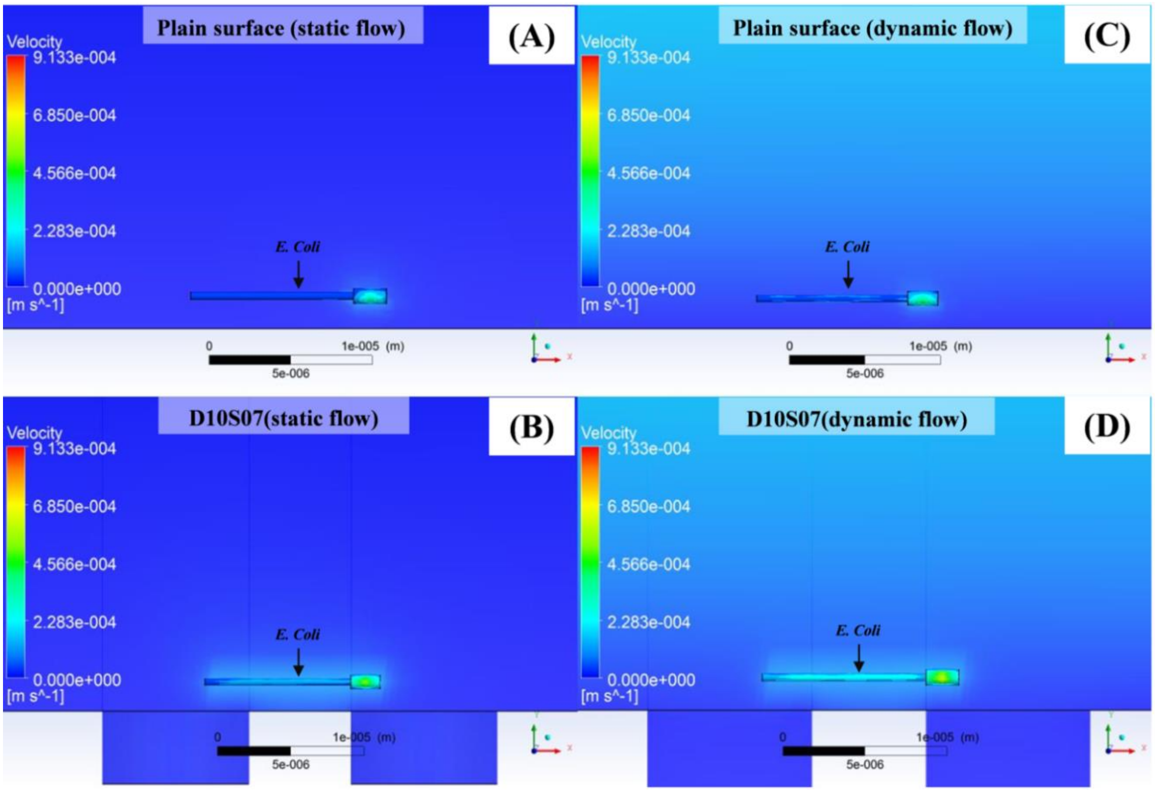

Figure 6.11: CFD simulation of velocity field around a moving rod-shaped bacterium: (A) over a plain surface in a static flow condition; (B) over D10S07 microwells in a static flow condition; (C) over a plain surface in a dynamic flow condition; (D) over D10S07 microwells in a dynamic flow condition. Flow direction from left to right (C–D).

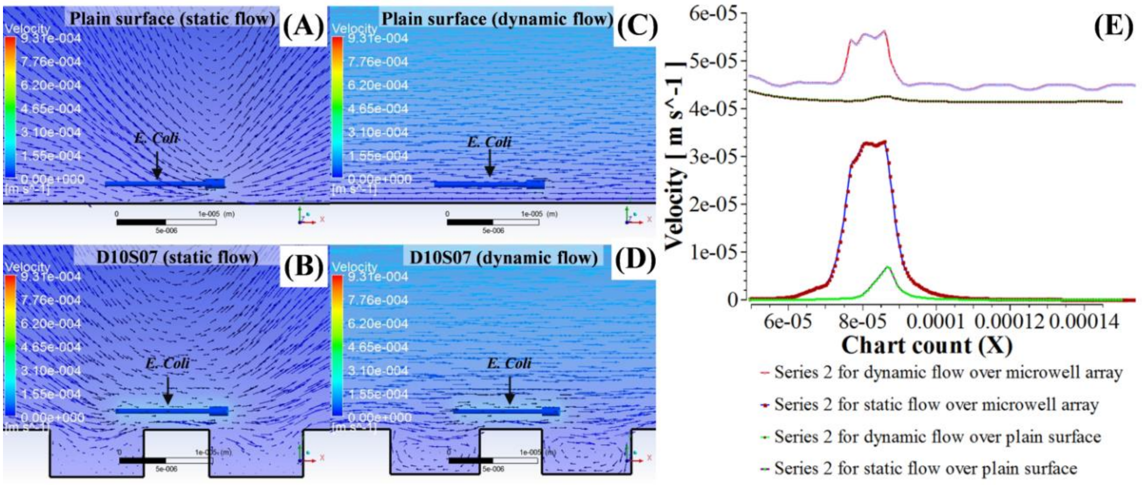

Figure 6.12: CFD simulation of velocity vectors around a moving rod-shaped bacterium: (A) over a plain surface in a static flow condition; (B) over D10S07 microwells in a static flow condition; (C) over a plain surface in a dynamic flow condition (D) over D10S07 microwells in a dynamic flow condition. Flow direction from left to right (C–D). (E) Local velocities for the above four cases (values taken at a distance of 1 μm below from the cell body centre).

The local velocity magnitudes at 1 μm below the cell body centre were also plotted (Figure 6.12E) to compare the differences between plain and patterned surfaces for both static and dynamic conditions. The magnitude of local velocity was always higher (maximum 55 μm s^{-1}) for a patterned surface in dynamic flow conditions. The lowest velocity field (~10 μm s^{-1}) was experienced by the modelled bacterium in the case of static flow conditions on a plain surface, which seemed a favourable flow field for the cell to control its motility.

Strain rates were also shown for the above four cases in Figure 6.13A–D and in the graph (Figure 6.13E). The bacterium modelled experienced the highest strain rates (maximum 20 s^{-1}) (Figure 6.13D) from the fluid particles in the case of patterned surfaces under dynamic flow conditions. On the other hand, for a plain surface under static flow conditions, the shear strain rate was below the critical limit (< 10 s^{-1}) of self-propulsion (Hill et al. 2007) (Figure 6.13A). This result further emphasised the notion that the dynamics of fluid particles on a plain surface were not adequate to alter the self-propelled trajectory of a motile rod-shaped bacterium such as *E. coli*. In other cases of static and dynamic flow conditions on patterned surfaces, the shear strain rate exceeded the critical limit of 10 s^{-1} (Figure 6.13B and D).

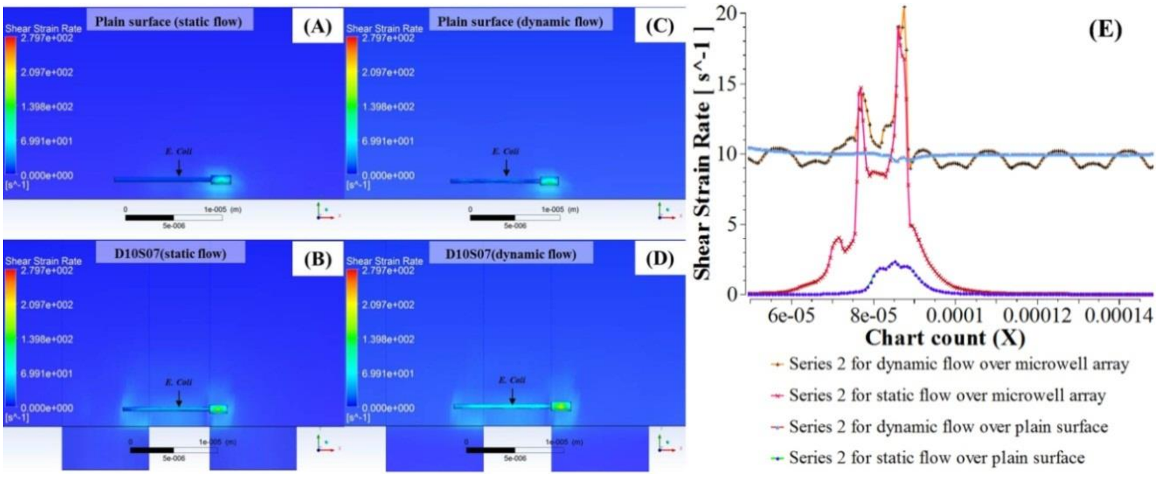

Figure 6.13: CFD simulation of shear strain rates around a moving rod-shaped bacterium: (A) over a plain surface in a static flow condition; (B) over D10S07 microwells in a static flow condition; (C) over a plain surface in a dynamic flow condition; (D) over D10S07 microwells in a dynamic flow condition. Flow direction from left to right (C–D). (E) Shear strain for the above four cases (values taken at a distance of 1 μm below the cell body centre).

The velocity field around rod-shaped bacterial cells showed lower convection very close to the plain surface (Figure 6.14A). The damping effect of fluid viscosity, which is more pronounced near a solid boundary, restrains fluid particles and microorganisms from higher convections. On the other hand, when the bacterial cells were swimming at higher elevations (5 and 15 μm as shown in Figure 6.14B and C), the fluid particles around the cells attained higher velocities. The developed velocity fields around the bacteria were less affected by the surface boundaries. At higher elevations, the local velocity around cells increased and the bacteria moved rapidly. In the case of a patterned surface, bacteria experienced higher convection even in close proximity to the boundary as shown in Figure 6.14D. They were subjected to a rapid change of their swimming depths and moved to upper strata. This phenomenon was also evident from the experiment where *E. coli* was moving to higher positions over the patterned surface and moving out of focus quickly (see also Figure 6.9). Generally, the fluctuating swimming depths due to the presence of a patterned surface make motile rod-shaped bacteria dynamically unstable. In this situation, even in a nearly static flow condition (eg wall shear stress < 0.01 Pa, as used in this study), the bacteria lost their control over self-propulsion and were thus washed away. Velocity streamlines over a patterned surface showed more perturbations of fluid particles in comparison to a plain surface (Figure 6.15). This microfluidic disturbance might affect the trajectories of a bacterium and could cause deflection (ie changing swimming depths rapidly) over the patterned surface.

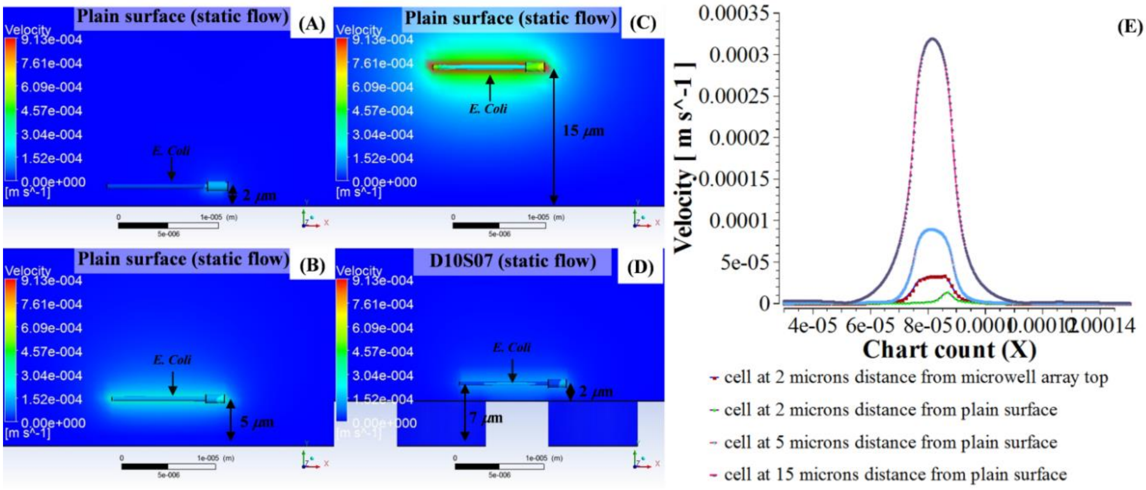

Figure 6.14: CFD simulation of velocity field around a rod-shaped bacterium at different depths of swimming: (A) over a plain surface at 2 µm distance; (B) over a plain surface at 5 µm distance; (C) over a plain surface at 15 µm distance; (D) over D10S07 microwells at 2 µm distance; (E) local velocities for (A–D) cases (values taken at a distance of 1 µm from the body centre of the bacterium).

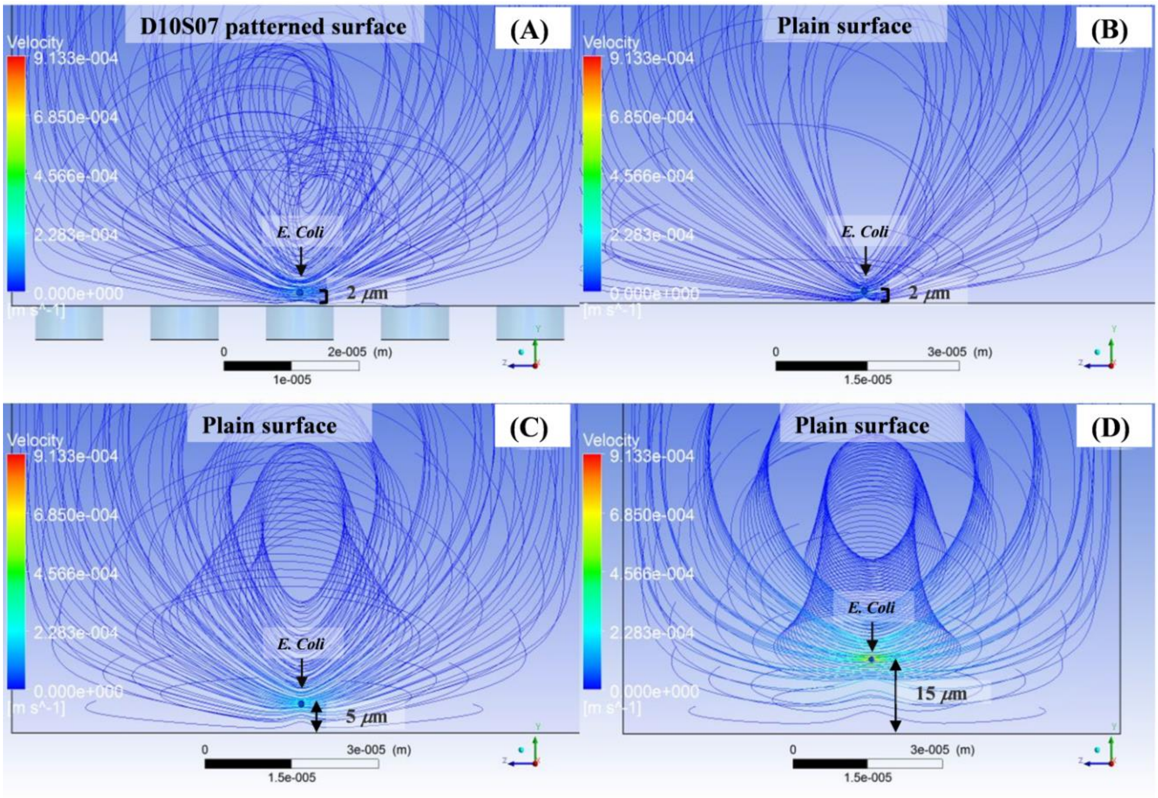

Figure 6.15: CFD simulated streamlines of the velocity fields around a rod-shaped bacterium at different depths of swimming (showing the front view of the domain): (A) over D10S07 microwells at 2 µm distance; (B) over a plain surface at 2 µm distance; (C) over a plain surface at 5 µm distance; (D) over a plain surface at 15 µm distance.

6.5.1 Effect of microwell array platform edge

The microwell array used in this study developed an elevated platform (5 µm) on the base planar surface (glass slide). Hence, a question is whether the resulting platform edge would influence the cell dynamics differently from a flush edge microwell array. CFD simulations of the microchannel for these two cases (ie platform edge and flush edge, as shown in Figure 6.16A and B) showed that fluid particles attained an instantaneous velocity fluctuation at the beginning of the platform edge which dampened immediately after crossing the entry length (~0.3 µm) (Figure 6.16C). As the flow condition was laminar and the entry length was too small, it was evident that the *E. coli* trajectories were mostly unaffected by the platform edge. However, experiments using holographic particle image velocimetry (HPIV), which allows recording of three-dimensional information of a flow (Heydt et al. 2007, 2009, 2012; Weiße et al. 2012), might assess the edge effect on motile microorganisms more precisely. In this study, as the bacterial cell velocities were determined separately for the plain and pattern surface regions, it was possible to exclude the platform edge effect from these cell velocity estimates. Regarding the effect from the top wall, it can be stated that the bottom wall of the microchannel remained unaffected, being a considerable distant apart (~100 μm).

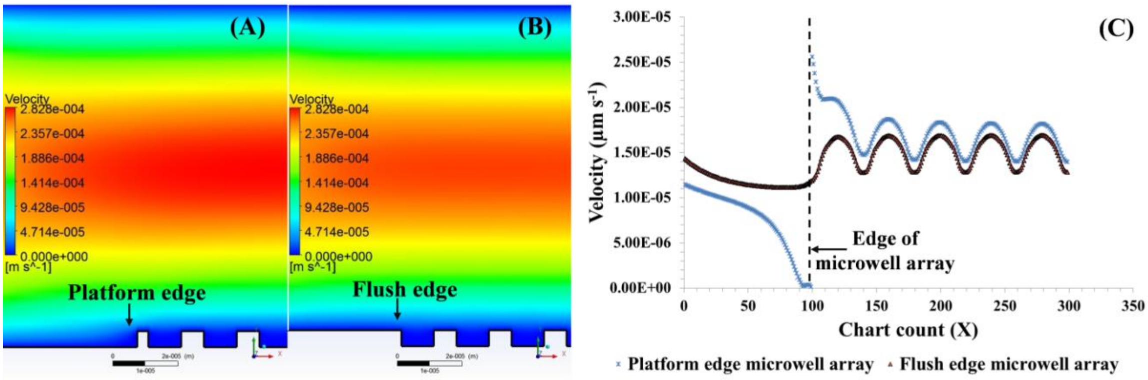

Figure 6.16: CFD simulations of the flow field inside a microchannel: (A) velocity field with platform edge microwell array; (B) velocity field with flush edge microwell array; (C) comparison of velocity fluctuations over microwell arrays. An instantaneous velocity fluctuation was observed at the beginning of the platform edge which dampened immediately after crossing the entry length.

6.5.2 Microwells *vs* micropillars

From the experimental results it was evident that bacterial cells attained higher convections over the microwell array. The question that arises is how increasing surface roughness could increase the local velocities of the cells. Various studies (Friedmann 2010a; Weiße et al. 2011) have shown that an alteration in surface topography could increase/ decrease the local convection based on the resulting roughness geometry and thus could be successfully applied in drag reduction. Friedmann et al. (2010a) showed that riblet-like structures could impede the cross flow and redirect it into the longitudinal direction. Through this redirecting, very slow rotating spirals are formed in the riblet valleys and the particles above the riblets flow away with the stream with higher velocity. The particles in the riblet valleys rotate slowly inside while new particles come and slip over them. Similarly, in this study the depression zones of microwells developed recirculation regions (see Figure 6.12B and D), which conceivably created effective velocity slip of the fluid particles over them. On the other hand, surface roughness (eg micropillars) which creates a direct obstacle to the longitudinal flow can decrease the streamwise local convection compared to the flat wall case. Weiße et al. (2011) studied the effect of micropillars on the assembly of artificial actin networks using digital in-line holographic microscopy (DIHM). They found that the pillar field (62,500 pillars: 5 µm in diameter, 15 µm in height and 20 µm spacing) caused the deceleration of fluid particles which eventually reduced the velocity of tracer particles in the pillar region compared to the flat wall. A comparison of flow fields over micropillars, microwells and plain surface was conducted by CFD simulation (Figure 6.17), which showed that the fluid particles at a 1 µm distance from microwells attained higher convection than on a plain surface. Micropillars, on the other hand, reduced particle velocities compared to microwells and plain surface. The increased local velocity over microwells was believed to increase the bacterial cell velocities as found in the experiment.

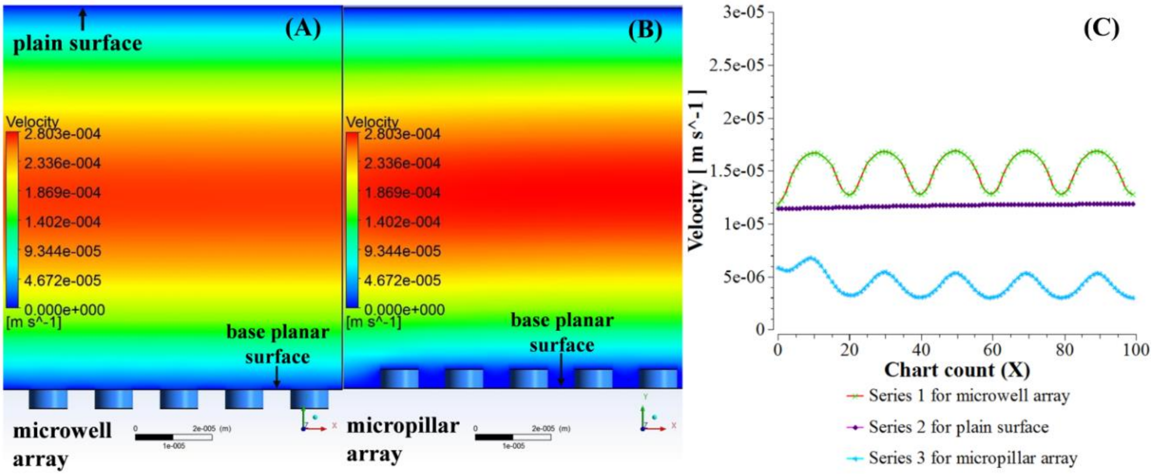

Figure 6.17: CFD simulations of the flow field inside a microchannel: (A) velocity field with micropillar array; (B) velocity field with microwell array; (C) comparison of velocity profile over micropillars, microwells and plain surface at 1 µm distance from the base planar surface.

The development of effective velocity slip with microstructures (recirculating fluid particles inside the depressed regions) can be an important design consideration for fabricating synthetic AF surfaces. The entrapping of air bubbles (plastrons) inside the grooves of the microstructure, for example, also causes effective velocity slip of fluid particles over them (see details in Chapter 2). Other design considerations for AF surfaces could be its ability to change the swimming depths of microorganisms and to develop high shear bounded isolated areas (see details in Chapter 5). Microstructures capable of keeping microorganisms away from the surface, moving them to higher convection zones and giving no shelter against fluctuating microfluidic forces could be considered effective for AF surfaces.

6.6 Conclusion

This study demonstrated that the dynamic stability of *E. coli* cells depends on the nature of the nearby surface boundaries, swimming depths and ambient fluid flow conditions. Microorganisms over patterned surfaces experience a complex microhydrodynamic environment, which includes differential strain rates, fluctuating velocity distribution and recirculation, and associated force distribution on submerged bodies according to the structural pattern of the boundary. Numerical simulations of a motile rod-shaped bacterium showed that the swimming behaviour could be altered by changing the surface microtopography. As the dynamic stability of a swimming microorganism is considered essential for its surface selection preference, the individual settlement process could be restrained immediately when the swimming dynamics getting disrupted. However, the characterisation of the swimming pattern of microorganisms over microtopographies is believed to be more complex than over plain surfaces in real-world scenarios, involving a number of interrelated parameters, including species morphology, the presence of other organisms, nutrient supply, surface chemistry, swimming depths and ambient fluid properties. This study explained only the hydromechanical development around an individual motile rod-shaped bacterium in a near-surface microfluidic environment due to the presence of microstructures. In relation to biofouling, it can be stated that the microtopographies can alter the dynamic stability of self-propelled microorganisms, which could in turn affect the subsequent stages of biofilm development. However, blocking or delaying the initial stage of biofilm development may not necessarily reduce or eliminate macrofouling, which typically develops later (Mieszkin et al. 2013). The present study was intended to highlight only the transitory AF mechanism of microtopographies in relation to the dynamics of *E. coli*, leaving apart numerous biotic and abiotic factors. In studying the dynamics of microorganisms on different surface patterns, the present approach of numerical simulation is convenient and simple. The dynamic responses of microorganisms in relation to surface patterns and the transitory AF efficiency of microtopographies can be explained comprehensively following the present approach of microfluidic investigation. The next chapter (Chapter 7) will present the conclusions, the overall outcome of this study, and some of the enclosed patterns suggested for future investigations targeting a better control on biofouling.

Chapter 7

7 Conclusions and future works

7.1 Conclusions

Novel antifouling (AF) technologies are being investigated and applied unremittingly to deter the settlement of fouling organisms on submerged surfaces. One such approach of developing AF surfaces is to create a deterrent surface with microtopographies on it which can inhibit the initial attachment of the settling microorganisms. Recently, these microstructure-based AF surfaces with their transitory AF capabilities against a wide range of organisms have drawn intense interest due to their non-toxic application. However, the random selection of surface patterns hinders the understanding of their transitory AF characteristics, including their further optimization potential. Mimicking only the shape geometries of natural AF surfaces without considering their integrated defence mechanism might not work as expected. New design considerations need to be followed to develop an effective AF surface to fit in real-world scenarios.

Recently used advanced imaging technologies and precise microfabrication techniques enhanced the understanding of the responses of microorganisms in relation to specific surface properties (eg topographic feature and geometries) and associated microfluidic environment (eg fluctuating stress-strain rates and hydrodynamic forces). The present study investigated the underlying mechanism of AF characteristics of microstructure-based surface patterns following a systematic approach of microfluidic analysis. The novel platform of investigation has provided a more rational view of surface engineering rather than any conventional approach such as random surface selection and testing. The findings of this study will help to improve the perceptions of the surface topographies, the relevant microhydrodynamics and the design optimization procedures for developing an effective AF surface.

7.2 Outcomes of this study

The main contribution of this study is to provide supporting evidences from the engineering perspective through the application of the microfluidic channel, numerical simulations, and overall, through the introduction of a novel methodology which enabled scientific proof of the claim that the near-surface microfluidic disturbances could inhibit the bacterial settlement on patterned surfaces. The advanced microfabrication technique and relevant numerical simulations made it possible to better understand the role of hydrodynamic aspects which are being considered the key factors responsible for the transitory AF characteristics shown by various patterned surfaces. This study also provided useful guidelines for developing synthetic microstructure-based AF surfaces. The outcomes from this study can be outlined as following:

1. Differential strain rates and the distribution patterns of wall shear stress developed on microtopographies affect the settlement procedures of microorganisms. The swimming activities and the surface selection procedure by an individual microorganism could also be restrained by the sharp fluctuations of strain rates along the entire path of its progression.

2. Feature dimensions (eg spacing and aspect ratio) of a patterned surface need to be considered in relation to the body size of the target species.

3. The development of non-bounded high shear stress around protruding portions of the microstructures, such as pillars and ridges, might not be very effective in developing deterrent effects for settling microorganisms. An enclosed pattern (eg circular, rectangular or hexagonal wells) which can develop high shear bounded isolated areas, could be a more effective AF pattern in a flowing fluid environment.

4. An important design consideration of synthetic AF surface can be its ability to create effective velocity slip over grooves of microstructures (ie recirculating fluid particles inside the depressed regions). Enclosed pattern surfaces can develop effective velocity slips in flowing fluid conditions by producing such recirculating zones and thus also can affect the natural swimming velocity of microorganisms substantially.

5. Microstructures capable of keeping microorganisms away from the surface, moving them to higher convection zones (ie changing their swimming depths) and giving no shelter against fluctuating microfluidic forces can be considered effective AF surfaces.

Based on the experimental results and numerical simulations, it is evident that the settlement of microorganisms on surfaces depends on microfluidic conditions associated to the geometrical features of that surface. From this study, it is also clear that the microfluidic conditions are the determinant factors for settlement in those particular cases (eg flowing flow conditions). Hence, this study emphasized that the geometrical features of any patterned surface need to be evaluated in relation to resultant microfluidic conditions (ie based on fluid environment that develops due to fluid-surface interaction) while selecting the surface for biofouling control.

7.3 Suggestions for future works

The microfluidic investigation presented in this study introduced the advantages of enclosed surface patterns over irregular/ protruded microstructures. Based on the wall shear distribution pattern over surfaces, it can be expected that the circular shape wells with hexagonal orientation is more AF effective than the wells with rectangular orientation (Figure 7.1), though the diameter and spacing of wells are same. It is noticeable in Figure 7.1 that the areas of the low wall shear regions (~ 0.5 Pa) get reduced substantially in the case of hexagonal orientation in comparison to the rectangular one.

This reduction in low wall shear areas can make the surface appear more unfavourable to microorganisms for their settlement.

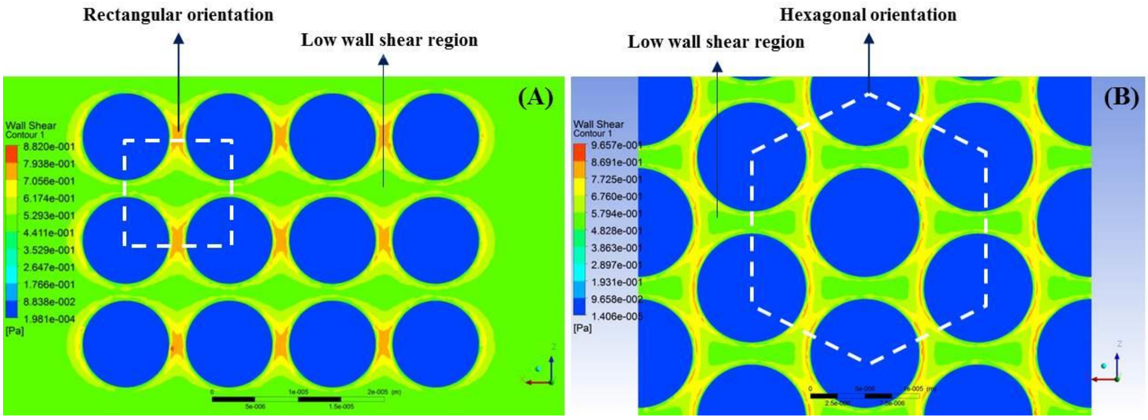

Figure 7.1: Different orientations with similar shape feature: (A) circular shape with rectangular orientation; (B) with hexagonal orientation. Low wall shear regions of hexagonal orientation get reduced in comparison to the rectangular orientation.

Similarly, a comparison of wall shear distribution on different shape geometries shows that the fish-scale like shape pattern can produce a compact orientation of depression zones and can also reduce the low shear regions substantially (Figure 7.2).

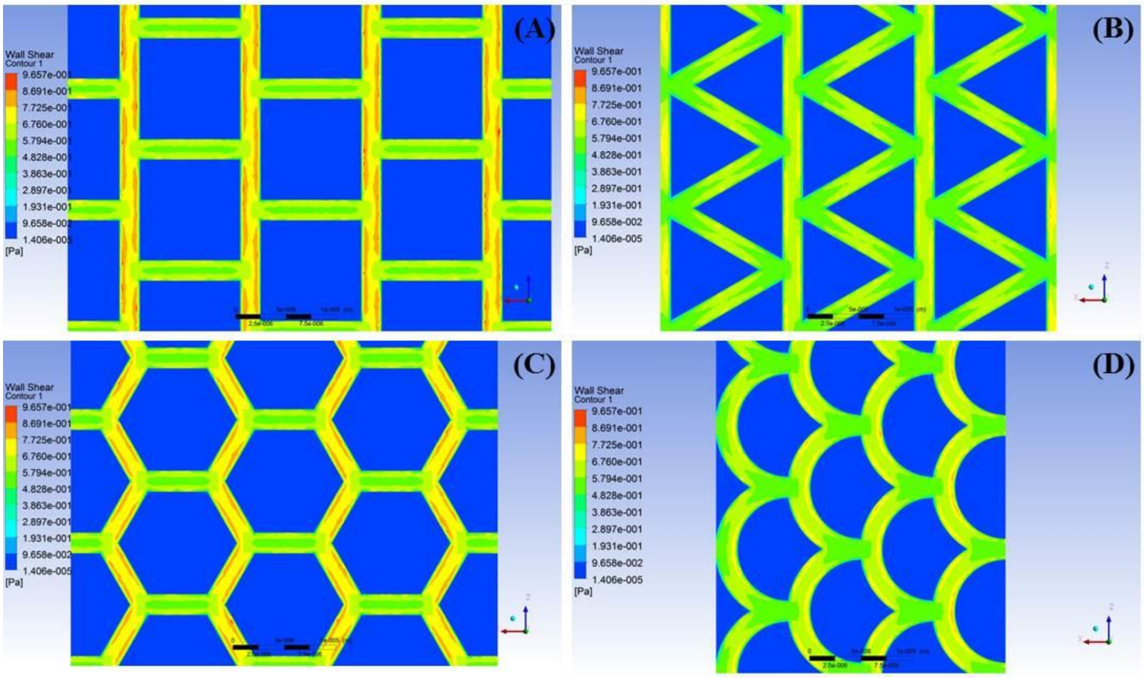

Figure 7.2: Wall shear distribution on different shape features: (A) square; (B) triangular; (C) hexagonal and (D) fish-scale like shape. All the shape features are with the same spacing between feature edges.

All the shape features described above show different wall shear distributions in terms of magnitude and orientations. These enclosed shape patterns are effective in developing non-uniform shear distribution which is not concentrated at some points (eg protruded portions of pillars). The shape patterns also develop high wall shear regions (ie capable of segregating microcolonies developed by microorganisms), and thus reduce low shear regions effectively. However, all the described AF properties of these shape patterns have been anticipated based on CFD simulations only, and are yet to go through experimental procedures to prove their actual AF efficacy. An investigation on all these shape patterns concurrently under the same fluid flow environment could be worthwhile to relate different shape geometries with their AF capabilities. The current microfluidic approach, including the microchannel based design set-up, can be followed in the suggested investigation. Figure 7.3 presents a 3D view of all these shape patterns (as described above) for a clear view of the protrusion and depression regions within the shape features.

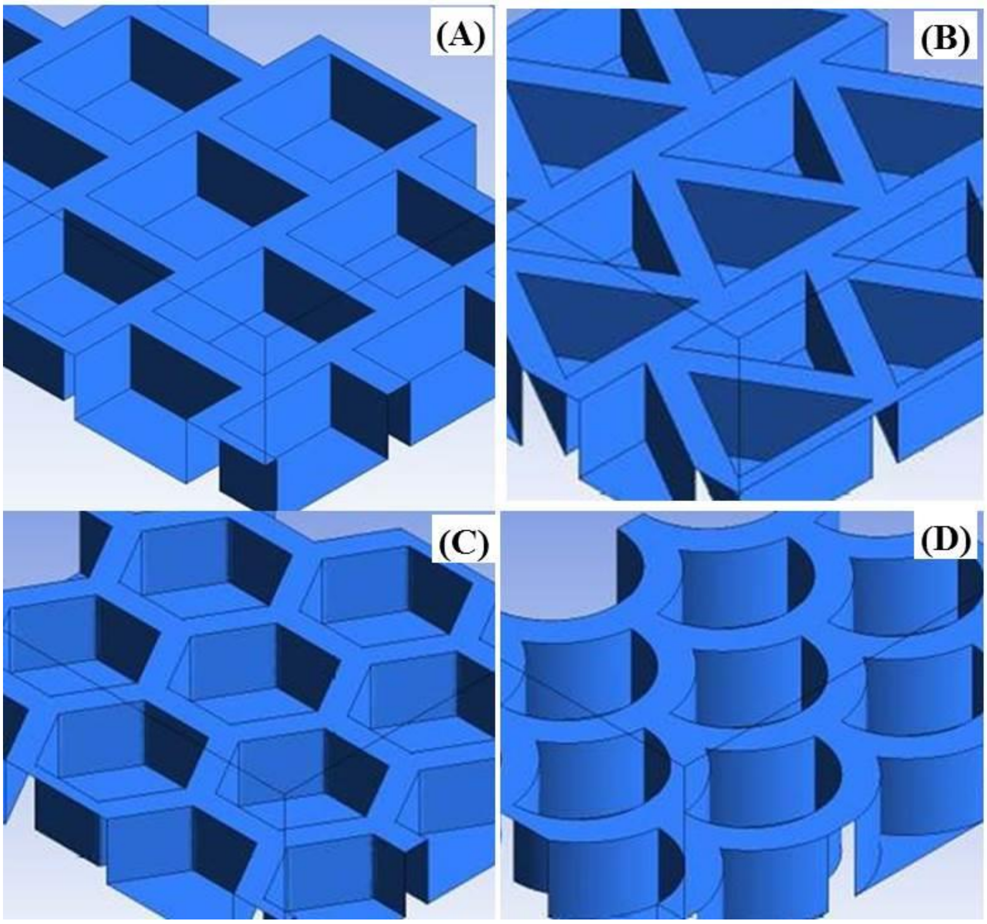

Figure 7.3: 3D view of the suggested shape patterns to be investigated in future: (A) square; (B) triangular; (C) hexagonal and (D) fish-scale like shape. All the shape features are at the same depths and spacing between feature edges.

References

AMBIO 2010. Advanced nanostructured surfaces for the control of biofouling. Final Activity Report of the AMBIO Integrated Project. Project No. NMP4-CT-2005-011827. University of Birmingham. UK.

Andersson M, Berntsson K, Jonsson P, Gatenholm P. 1999. Microtextured surfaces: towards macrofouling resistant coatings. Biofouling 14:167–178.

ANSYS CFX documentation 2011. ANSYS CFX-Solver Theory Guide. ANSYS Inc., Canonsburg, PA, USA.

Avron JE. O. Kenneth O. Oakmin DH. 2005. Pushmepullyou: An efficient micro-swimmer. New J. Phys. 7: 234–238.

Azis PKA, Tisan IA, Sasikumar N. 2001. Biofouling potential and environmental factors of seawater at a desalination plant intake. Desalination 135:69-82.

Baier RE 1981. Early events of micro-biofouling of all heat transfer equipment. In: Somerscales EFC, Knudsen JG. Fouling of heat transfer equipment. Washington: Hemisphere Publish Corp. p. 293-304.

Barnes WL, Dereux A, Ebbensen TW. 2003. Surface plasmon subwavelength optics. Nature: 424, p. 824.

Barth TJ, Jesperson DC. 1989. The design and application of Upwind schemes on unstructured meshes. AIAA Paper 89-0366.

Bechert DW, Bruse M, Hage W, Meyer R. 2000a. Fluid Mechanics of biological surfaces and their technological application. Naturwissenschaften- The Science of Nature 87:157-171.

Bechert DW, Bruse M, Hage W. 2000b. Experiments with three dimensional riblets as an idealized model of shark skin. Springer-Verlag 28:403-412.

Berg HC. 2004. *E. coli* in motion. New York (NY): Springer.

Berke A, Turner L, Berg H, Lauga E. 2008. Hydrodynamic attraction of swimming microorganisms by surfaces. Phys. Rev. Lett. 101:1-4.

Bers AV, Wahl M. 2004. The influence of natural surface microtographies on fouling. Biofouling 20:43-51.

Bhatti MS , Shah RK. 1987. Turbulent and transition flow convective heat transfer in ducts. In handbook of single-phase convetive heat transfer, Wiley Interscience.

Bhushan B, Jung YC. 2011. Natural and biomimetic artificial surfaces for superhydrophobicity, self-cleaning, low adhesion and drag reduction. Progress in Materials Science 56:1-108.

Bol M, Mohle RB, Haesner M, Neu TR. 2009. 3D Finite element model of biofilm detachment using real biofilm structures from CLSM data. Biotechnology and Bioengineering 103:177-186.

Callow JA, Callow ME. 2011. Trends in the development of environmentally friendly fouling-resistant marine coatings. Nature communications 2:244.

Callow ME, Jennings AR, Brennan AB, Seegert CE, Gibson A, Wilson L, Feinberg A, Baney R, Callow JA. 2002. Microtopographic cues for settlement of zoospores of the green fouling alga *Enteromorpha*. Biofouling 18:237–245.

Campbell D, Beckman K, Calderon C, Doolan P, Ottosen R, Ellis A, Lisensky G. 1999. Replication and Compression of Bulk and Surface W Structures with Polydimethylsiloxane Elastomer. J Chem Educ. 75:537-541.

Carl C, Poole AJ, Sexton BA, Glenn FL, Vucko MJ, Williams MR, Whalan S, Nys RD. 2012. Enhancing the settlement and attachment strength of pediveligers of *Mytilus galloprovincialis* by changing surface wettability and microtopography, Biofouling 28:175-186.

Carlborg CF, Wijngaart WVD. 2011. Sustained superhydrophobic friction reduction at high liquid pressure and large flows. Langmuir 27:487-493.

Carman M, Estes T, Feinberg A, Schumacher J, Wilkerson W, Wilson L, Callow M, Callow J, Brennan A. 2006. Engineered antifouling microtopographies – correlating wettability with cell attachment. Biofouling 22:11–21.

Çengel YA, Cimbala JM. 2010. Fluid mechanics fundamentals and applications. 2nd ed. New York (NY): McGraw-Hill.

Champ MA. 2003. Economic and environmental impacts on port and harbors from the convention to ban harmful marine anti-fouling systems. Mar Pollut Bull 46:935–940.

Characklis WG. 1981. Fouling biofilm development: a process analysis. Biotechnol. Bioengng 23: 1923-1960.

Chen H, Rosengarten G, Li M, Nordon RE. 2012. Design of microdevices for long-term live cell imaging. J Micromech Microeng. 22:1–11.

Chung KK, Schumacher JF, Sampson EM, Burne RA, Antonelli PJ, Brennan AB. 2007. Impact of engineered surface microtopography on biofilm formation of *Staphylococcus aureus*. Biointerphases. 2:89–94.

Cisneros LH, Cortez R, Dombrowski C, Goldstein RE, Kessler JO. 2007. Fluid dynamics of self-propelled micro-organisms, from individuals to concentrated populations. Exp Fluids. 43:737–753.

Clare AS, Rittschof D, Gerhart DJ, Maki JS. 1992. Molecular approaches to non-toxic antifouling. Invertebr Reprod Dev. 22:67–76.

Cooper SP, Finlay JA, Cone G, Callow ME, Callow JA, Brennan AB. 2011. Engineered antifouling microtopographies: kinetic analysis of the attachment of zoospores of the green alga *Ulva* to silicone elastomers. Biofouling 27: 881-892.

Cosson J, Huitorel P, Gagnon C. 2003. How spermatozoa come to be confined to surfaces. Cell Motility and the Cytoskeleton. 54:56–63.

Crimaldi JP, Koseff JR, Monismith SG. 2007. Structure of mass and momentum fields over a model aggregation of benthic filter feeders. Biogeosciences 4:269–282.

Crowdy DG, Lee S, Samson O, Hosoi AE, Lauga E. 2011. A two dimensional model of low Reynolds number swimmers beneath a free surface. J. Fluid Mech. 681: 24–47.

Darnton NC, Turner L, Rojevsky S, Berg HC. 2010. Dynamics of bacterial swarming. Biophys J. 98:2082–2090.

Darwish MS, Moukalled F. 2003. TVD schemes for unstructured grids. International Journal of Heat and Mass Transfer. 46: 599–611.

Derek C, Tretheway, Carl DM. 2004. A generating mechanism for apparent fluid slip in hydrophobic microchannels. Phys Fluids. 16:1509–1515.

Dobretsov S, Abed RMM, Teplitski M. 2013. Mini-review: inhibition of biofouling by marine microorganisms. Biofouling. 29:423–441.

Dobretsov SV, Dahms HU, Qian PY. 2006. Inhibition of biofouling by marine microorganisms and their metabolites. Biofouling. 22:43–54.

Drescher K, Lptos KC, Tuval I, Ishikawa T, Pedley TJ, Goldstein RE. 2009. Dancing *Volvox*: hydrodynamic bound states of swimming algae. Phys. Rev. Lett. 102:1-4.

Epstein N. 1981. Fouling in heat exchangers. In: Somerscales EFC, Knudsen JG, editors. Fouling of heat transfer equipment. Washington: Hemisphere Publish Corp. p. 701–34.

Evans AA, Lauga E. 2010. Propulsion by passive filaments and active flagella near boundaries. Physical Review E. 82:1-12.

Finlay JA, Callow ME, Schultz MP, Swain GW. 2002. Adhesion strength of setteled spores of the green alga *Enteromorpha*. Biofouling 18:251-256.

Fisher PJ, Petrini O. 1992. Fungal saprobes and pathogens as endophytes of rice (Oryza sativa L.). New Phytol 120:137–143.

Fitridge I, Dempster T, Guenther J, de Nys R . 2012. The impact and control of biofouling in marine aquaculture: a review. Biofouling. 28:649-669.

Flemming HC, Ridgway H. 2009. Biofilm control: Conventional and alternative approaches. Marine and Industrial Biofouling 4:103-117.

Friedmann E, Portl J, Richter T. 2010a. A study of shark skin and its drag reducing mechanism. In: Advances in Mathematical Fluid Mechanics. Rannacher R, Sequeira A. (eds.). Springer- Verlag Berlin Heidelberg. p. 271-285.

Friedmann E. 2010b. The optimal shape of riblets in the viscous sublayer. J Math Fluid Mech. 12:243–265.

Gary Amy. 2007. Fundamental understanding of organic matter fouling of membranes. Desalination 231: 44–51.

Goldstein DB, Tuan TC. 1998. Secondary flow induced by riblets. J Fluid Mech 363:115-151.

Gonzalez Barrios AF, Zuo R, Hashimoto Y, Yang L, Bentley WE, Wood TK. 2006. Autoinducer 2 controls biofilm formation in *Escherichia coli* through a novel motility quorumsensing regulator (MqsR, B3022). J Bacteriol. 188:305–316.

Gorgi K. 2008. Photolithographic and Replication Techniques for Nanofabrication and Photonics. PhD thesis. School of Electrical and Computer Engineering. RMIT University.

Granhag LM, Finlay JA, Jonsson PR, Callow JA, Callow ME. 2004. Roughness-dependent removal of settled spores of the green alga *Ulva* (syn. *Enteromorpha*) exposed to hydrodynamic forces from a water jet. Biofouling 20:117-122.

Granhag ML, Larsson AI, Jonsson PR. 2007. Algal spore settlement and germling removal as a function of flow speed. Mar Ecol Prog Ser 344: 63–69.

Granville PS. 1987. Three indirect methods for the drag characterization of arbitrarily rough surfaces on flat plates. J Ship Res 31:70–77.

Grigson CWB. 1992. Drag losses of new ships caused by hull finish. J Ship Res 36:182–196.

Guasto JS, Rusconi R, Stocker R. 2012. Fluid mechanics of planktonic microorganisms. Annu Rev Fluid Mech. 44:373–400.

Hadfield MG. 2011. Biofilms and marine invertebrate larvae: what bacteria produce that larvae use to choose settlement sites? Annu Rev Mar Sci. 3:453–470.

Halder P, Nasabi M, Jayasuriya N, Shimeta J, Deighton M, Bhattacharya S, Mitchell A, Bhuiyan MA. 2014. An assessment of the dynamic stability of microorganisms on patterned surfaces in relation to biofouling control. Biofouling. 30:695-707.

Halder P, Nasabi M, Lopez FJT, Jayasuriya N, Bhattacharya S, Deighton M, Mitchell A, and Bhuiyan MA. 2013. A novel approach to determine the efficacy of patterned surfaces for biofouling control in relation to its microfluidic environment. Biofouling. 29:697-713.

Haslbeck EG, Bohlander G. 1992. Microbial biofilm effects on drag – lab and field. Proceedings SNAME Ship Production Symposium. Paper No. 3A-1. p. 7. Jersey City (NJ): Society of Naval Architects and Marine Engineers.

Heydt M, Divos P, Grunze M, Rosenhahn A. 2009. Analysis of holographic microscopy data to quantitatively investigate three-dimensional settlement dynamics of algal zoospores in the vicinity of surfaces. Eur Phys J E. 30:141–148.

Heydt M, Pettit ME, Cao X, Callow ME, Callow JA, Grunze M, Rosenhahn A. 2012. Settlement behavior of zoospores of *Ulva linza* during surface selection studied by digital holographic microscopy. Biointerphases. 7:1–7.

Heydt M, Rosenhahn A, Grunze M, Pettitt M, Callow ME. 2007. Digital in-line holography as a three-dimensional tool to study motile marine organisms during their exploration of surfaces. J Adhesion. 83:417–430.

Hill J, Kalkanci O, McMurry JL, Koser H. 2007. Hydrodynamic surface interactions enable *Escherichia Coli* to seek efficient routes to swim upstream. Physical Review Letters 98:068101(1-4).

Horn H, Reiff H, Morgenroth E. 2003. Simulation of growth and detachment in biofilm systems under defined hydrodynamic conditions. Biotechnology and Bioengineering 81:607-617.

Huang H, Kamm RD, Lee RT. 2004. Cell mechanics and mechanotransduction: pathways, probes, and physiology. Am J Physiol Cell Physiol 287:C1-C11.

Hwang HJ, Simon Song S. 2008. The effects of grooves on the flow rate in a microchannel. Biochip J. 2:123–126.

Ibrahim HA. 2012. Fouling in Heat Exchangers. In: MATLAB - A Fundamental Tool for Scientific Computing and Engineering Applications. Prof. Vasilios Katsikis (Ed.). Book chapter 3. p. 57-96. InTech. Croatia.

Janet SN, Ronald JB, Dan FL, Robert FM, Peter HB, David CW.1981. Effect of manual brush cleaning on biomass and community structure of microfouling film formed on aluminum and titanium surfaces exposed to rapidly flowing seawater. Applied and Environmental Microbiology. 41: 1442-1453.

Kalele SA, Tiwari NR, Gosavi SW, Kulkarni SK. 2007. Plasmon-assisted photonics at the nanoscale, Journal of Nanophotonics. 1: 012501

Kays WM, Crawford ME 1993. Convective heat and mass transfer, 3rd ed. New York: McGraw-Hill.

Kempf G. 1937. On the effect of roughness on the resistance of ships. Trans INA 79:109–119.

Kirisits MJ, Margolis JJ, Purevdorj-Gage BL, Vaughan B, Chopp DL, Stoodley P, Parsek MR. 2007. Influence of the hydrodynamic environment on quorum sensing in *Pseudomonas aeruginosa* biofilms. J Bacteriol. 189:8357–8360.

Koch DL, Subramanian G. 2011. Collective hydrodynamics of swimming microorganisms: living fluids. Annu Rev Fluid Mech. 43:637–659.

Koehl MAR. 2007. Mini review: Hydrodynamics of larval settlement into fouling communities. Biofouling 23:357-368.

Köhler J, Hansen PD, Wahl M. 1999. Colonization patterns at the substratum-water interface: how does surface microtopography influence recruitment patterns of sessile organisms? Biofouling 14:237–248.

Kundu PK, Cohen IM. 2008. Fluid mechanics. 4th ed. New York: Elsevier Academic Press. USA.

Larsson AI, Mattsson-Thorngren L, Granhag ML, Berglin M. 2010. Fouling-release of barnacles from a boat hull with comparison to laboratory data of attachment strength. Journal of Experimental Marine Biology and Ecology. 392: 107–114

Lauga E, DiLuzio WR, Whitesides GM, Stone HA. 2006. Swimming in circles: motion of bacteria near solid boundaries. Biophys J 90:400–412.

Lauga E, Powers TR. 2009. The hydrodynamics of swimming microorganisms. Rep. Prog. Phys. 72:1-36.

Lauga E. 2007. Floppy swimming: Viscous locomotion of actuated elastica. Physical Review E. 75: (041916:1-16).

Lee JH, Kaplan JB, Lee WY. 2008. Microfluidic devices for studying growth and detachment of *Staphylococcus epidermidis* biofilms. Biomed Microdevices 10:489–498.

Lee S-J, Kim SW, Choa Y-H, Shin W-S, Lee SE, Kim C-S, Hong SJ, Chung BH, Kim JJ, Yoon MS. 2004. A comparative multicentre study on the incidence of catheter-associated urinary tract infection between nitrofurazone-coated and silicone catheters. International Journal of Antimicrobial Agents. 24S: S65–S69.

Leer-Andersen M, Larsson L. 2003. An experimental/ numerical approach for evaluating skin friction on full-scale ships with surface roughness. J Mar Sci Technol 8:26–36.

Lewthwaite JC, Molland AF, Thomas KW. 1985. An investigation into the variation of ship skin frictional resistance with fouling. Trans RINA 127:269–284.

Li J, Attila C, Wang L, Wood TK, Valdes JJ, Bentley WE. 2007. Quorum sensing in *Escherichia coli* is signaled by AI-2/LsrR: effects on small RNA and biofilm architecture. J Bacteriol. 189:6011–6020.

Long CJ, Finlay JA, Callow ME, Callow JA, Brennan AB. 2010a. Engineered antifouling microtopographies: mapping preferential and inhibitory microenvironments for zoospore attachment. Biofouling 26:941–952.

Long CJ, Schumacher JF, Robinson PAC, Finlay JA, Callow ME, Callow JA, Brennan AB. 2010b. A model that predicts the attachment behavior of *Ulva linza* zoospores on surface topography. Biofouling 26:411–419.

Long DA. 2002. The Raman effect: A Unified treatment of the theory of Raman scattering by molecules, John Wiley & Sons, LTD

Macosko C, Larson R. 1994. Rheology: principles, measurements, and applications. New York (NY): VCH.

Marcos F, Powers TR, Stocker R. 2012. Bacterial rheotaxis. PNAS. 109:4780–4785.

Marmur A. 2006a. Super-hydrophobicity fundamentals: implications to biofouling prevention. Biofouling. 22: 107-115.

Marmur A. 2006b. Underwater superhydrophobicity: Theoretical feasibility. Langmuir 22:1400-1402.

Medhurst JS. 1989. The systematic measurement and correlation of the frictional resistance and topography of ship hull coatings, with particular reference to ablative antifoulings. PhD thesis.University of Newcastleupon- Tyne. UK.

MERUS - The water conditioner company. Heat exchanger fouling and cleaning service, viewed 28 June 2014, http://www.merusonline.com/in-industry/he-fouling-cleaning

Mieszkin S, Callow M, Callow JA. 2013. Interactions between microbial biofilms and marine fouling algae: a mini review. Biofouling. 29:1097–1113.

Najafi A, Golestanian R. 2004. Simple swimmer at low Reynolds number: three linked spheres. Phys. Rev. E. 69:062901.

Niu C, Robbins CM, Pittman KJ, Osborn JL, Stubblefield BA, Simmons RB, Gilbert ES. 2013. LuxS influences *Escherichia coli* biofilm formation through autoinducer-2-dependent and autoinducer-2-independent modalities. FEMS Microbiol Ecol. 83:778-791.

Or Y, Zhang S, Murray RM. 2011. Dynamics and stability of low-Reynolds-number swimming near a wall. SIAM J. Applied dynamical systems. 10:1013-1041.

Ou J, Perot B, Rothstein JP. 2004. Laminar drag reduction in microchannels using ultrahydrophobic surfaces. Phys Fluids. 16:4635–4643.

Ou J, Rothstein JP. 2005. Direct velocity measurements of the flow past drag-reducing ultrahydrophobic surfaces. Phys Fluids. 17:103606 1–10.

Pankratz T. 2008. An Overview of Seawater Intake Facilities for Seawater Desalination. Alden Desalination Intake Solutions Workshop, Holder, Massachusetts. USA.

Patankar NA. 2004. Mimicking the lotus effect: influence of double roughness and slender pillars. Langmuir 20:8209-8213.

Petronis S, Berntsson K, Gold J. 2000. Design and microstructuring of PDMS surfaces for improved marine biofouling resistance. J Biomater Sci Polymer Edn 11:1051-1072.

Picioreanu C, van Loosdrecht MCM, Heijnen JJ. 2001. Two-dimensional model of biofilm detachment caused by internal stress from liquid flow. Biotechnol Bioeng 72:205–218.

Picioreanu C, Vrouwenvelder JS, van Loosdrecht MCM. 2009. Three-dimensional modeling of biofouling and fluid dynamics in feed spacer channels of membrane devices. Journal of Membrane Science 345: 340–354.

Picologlou BF, Zelver N, Characklis WG. 1980. Biofilm growth and hydraulic performance. ASCE J Hydraulics Div. 106:733–746.

Poetes R, Holtzmann K, Franze K, Steiner U. 2010. Metastable underwater superhydrophobicity. PRL. 105: 166104 (p. 1-4).

Purcell EM. 1977. Life at low Reynolds numbers. Am. J. Phys. 45: 3–11.

Qian PY, Lau SCK, Dahms HU, Dobretsov S, Harder T. 2007. Marine biofilms as mediators of colonization by marine macroorganisms: implications for antifouling and aquaculture. Mar Biotechnol. 9:399–410.

Qian PY, Rittschof D, Sreedhar B, Chia FS. 1999. Macrofouling in unidirectional flow:miniature pipes as experimental models for studying the effects of hydrodynamics on invertebrate larval settlement. Marine Ecology Progress Series 191:141-151.

Railkin AI. 2004. Marine biofouling: colonization processes and defenses. Boca Raton (FL):CRC Press.

Ramia M, Tullock DL, Phan-Thien N. 1993. The role of hydrodynamic interaction in the locomotion of microorganism. Biophys J. 65:755–778.

Reddy ST, Chung KK, McDaniel CJ, Darouiche RO, Landman J, Brennan AB. 2011. Micropatterned surfaces for reducing the risk of catheter-associated urinary tract infection: an in vitro study on the effect of sharklet micropatterned surfaces to inhibit bacterial colonization and migration of uropathogenic *Escherichia coli*. Journal of Endourology. 25:1547-1552

Redfield AC, Ketchum BH. 1952. Ship resistance, in Marine Fouling and Its Prevention. Redfield AC and Ketchum BH. Eds. US Naval Institute. Annapolis, MD, 21.

Reznichenko OG. 1978. Classification and spatial characteristic of fouling biotopes. Biol. Morya. 4, 3.

Rittschof D. 2010. Research on environmentally benign antifouling coatings. In: Durr S, Thomason JC, editors. Biofouling. Oxford: Wiley-Blackwell; p. 396–409.

Rosenhahn A, Schilp S, Kreuzer HJ. 2010. The role of ‘inert’ surface chemistry in marine biofouling prevention. Phys Chem Chem Phys. 12:4275–4286.

Rosenhahn A, Sendra GH. 2012. Surface sensing and settlement strategies of marine biofouling organisms. Biointerphases. 7:1–13.

Samson O. 2010. Low Reynolds Number Swimming in Complex Environments. PhD thesis. Department of Mathematics. Imperial College. London. UK.

Scardino AJ, de Nys R. 2011. Mini review: biomimetic models and bioinspired surfaces for fouling control. Biofouling 27:73–86.

Scardino AJ, Guenther J, de Nys R. 2008. Attachment point theory revisited: the fouling response to a microtextured matrix. Biofouling 24:45–53.

Scardino AJ, Harvey E, de Nys R. 2006. Testing attachment point theory: diatom attachment on microtextured polyimide biomimics. Biofouling 22:55–60.

Schultz MP, Bendick JA, Holm ER, Hertel WM. 2011. Economic impact of biofouling on a naval surface ship. Biofouling. 27:87-98.

Schultz MP, Finlay JA, Callow ME, Callow JA. 2000. A turbulent channel flow apparatus for the determination of the adhesion strength of microfouling organisms. Biofouling 15:243-251.

Schultz MP, Swain GW. 1999. The effect of biofilms on turbulent boundary layers. ASME J Fluids Eng 121:733–746.

Schultz MP, Swain GW. 2000. The influence of biofilms on skin friction drag. Biofouling 15:129–139.

Schultz MP. 2004. Frictional resistance of antifouling coating systems. ASME J Fluids Eng 126:1039–1047.

Schultz MP. 2007. Effects of coating roughness and biofouling on ship resistance and powering. Biofouling 23:331–341.

Schumacher JF, Aldred N, Callow ME, Finlay JA, Callow JA, Clare AS, Brennan AB. 2007a. Species-specific engineered antifouling topographies: correlations between the settlement of algal zoospores and barnacle cyprids. Biofouling 23:307–317.

Schumacher JF, Carman ML, Estes TG, Feinberg AW, Wilson LH, Callow ME, Callow JA, Finlay JA, Brennan AB. 2007b. Engineered antifouling microtopographies – effect of feature size, geometry, and roughness on settlement of zoospores of the green alga *Ulva*. Biofouling 23:55–62.

Schumacher JF, Long CJ, Callow ME, Finlay JA, Callow JA, Brennan AB. 2008. Engineered nanoforce gradients for inhibition of settlement (attachment) of swimming algal spores. Langmuir 24:4931-4937.

Schumacher JF. 2007c. Control of marine biofouling and medical biofilm formation with Engineered topography. PhD thesis. University of Florida. USA.

Shapere A, Wilczek F. 1989. Geometry of self-propulsion at low Reynolds numbers. J. Fluid Mech. 189: 557–585.

Somerscales EFC. 1981. Introduction and summary: the fouling of heat transfer equipment. In: Somerscales EFC, Knudsen JG. Fouling of heat transfer equipment. Washington: Hemisphere Publish Corp. p. 1–27.

Starostin IV, Permitin YuE. 1963. Species composition and quantitative dynamics of macrofouling in seawater piping of metal works on the Sea of Azov, Tr. Inst. Okeanol. Akad. Nauk SSSR, 70, 124.

Stone HA. Samuel ADT. 1996. Propulsion of microorganisms by surface distortions. Phys. Rev. Lett. 77: 41024104.

Stoodley LH,Costerton JA, Stoodley P. 2004. Bacterial biofilms: from the natural environment to infectious diseases. Nat. Rev. Microbiol. 2: 95–108.

Stoodley P, Cargo R, Rupp CJ, Wilson S, Klapper I. 2002. Biofilm material properties as related to shear-induced deformation and detachment phenomena. J Ind Microbiol Biotechnol 29:361–367.

Stoodley P, Jacobsen A, Dunsmore BC, Purevdorj B, Wilson S, Lappin-Scott HM, Costerton JW. 2001a. The influence of fluid shear and AlCl3 on the material properties of *Pseudomonas aeruginosa* PA01 and Desulfovibrio sp. EX265 biofilms. Water Sci Technol 43:113–120.

Stoodley P, Lewandowski Z, Boyle JD, Lappin-Scott HM. 1998. Oscillation characteristics of biofilm streamers in turbulent flowing water as related to drag and pressure drop. Biotechnol Bioeng 57:536–544.

Stoodley P, Lewandowski Z, Boyle JD, Lappin-Scott HM. 1999. Structural deformation of bacterial biofilms caused by short-term fluctuations in fluid shear: An in situ investigation of biofilm rheology. Biotechnol Bioeng 65: 83–92.

Stoodley P, Wilson S, Hall-Stoodley L, Boyle JD, Lappin- Scott HM, Costerton JW. 2001b. Growth and detachment of cell clusters from mature mixed species biofilms. Appl Environ Microbiol 67:5608–5613.

Swain G. 1998. Biofouling control: a critical component of drag reduction. Proceedings of the International Symposium on Seawater Drag Reduction. Newport (RI). p.155–161.

Sweat LH, Johnson KB. 2013. The effects of fine-scale substratum roughness on diatom community structure in estuarine biofilms. Biofouling. 29:879–890.

Taherzadeh D, Picioreanu C, Küttler U, Simone A, Wall WA, Horn H. 2010. Computational study of the drag and oscillatory movement of biofilm streamers in fast flows. Biotechnol Bioeng 105:600–610.

Thomason JC, Davenport J, Rogerson A. 1994. Antifouling performance of the embryo and eggcase of the dogfish *Scyliorhinus canicula*. J Mar Biol Assoc UK. 74:823–836.

Tovar-Lopez FJ, Rosengarten G, Westein E, Khoshmanesh K, Jackson SP, Mitchell A, Nesbitt WS. 2010. A microfluidics device to monitor platelet aggregation dynamics in response to strain rate micro-gradients in flowing blood. Lab Chip. 10:291–302.

Townsin RL, Byrne D, Svensen TE, Milne A. 1981. Estimating the technical and economic penalties of hull and propeller roughness. Trans SNAME 89:295–318.

Truong VK, Webb HK, Fadeeva E, Chichkov BN, Wu AHF, Lamb R, Wang JY, Crawford RJ, Ivanova EP. 2012. Air-directed attachment of coccoid bacteria to the surface of superhydrophobic lotus-like titanium, Biofouling. 28: 539-550.

Versteeg HK, Malalasekera W. 2007. An Introduction to Computational Fluid Dynamics: The Finite Volume Method (2nd Ed.). Pearson Education Limited. UK.

Vigeant MA, Ford RM, Wagner M, Tamm LK. 2002. Reversible and irreversible adhesion of motile *Escherichia coli* cells analyzed by total internal reflection aqueous fluorescence microscopy. Appl. Environ. Microbiol. 68: 2794-2801.

Vladkova T. 2009. Surface modification approach to control biofouling. Marine and Industrial Biofouling 4:135-163.

Vucko MJ, Poole AJ, Sexton BA, Glenn FL, Whalan S, deNys R. 2013. Combining a photocatalyst with microtopography to develop effective antifouling materials. Biofouling. 29: 751–762.

Wahl M, Lafargue F. 1990. Marine epibiosis II. Reduced fouling on Polysyncraton lacazei (Didemnidae, Tunicata) and proposal of an antifouling potential index. Oecologia. 82:275–282.

Wahl M. 1989. Marine Epibiosis I. Fouling and antifouling. Some basic aspects. Mar Ecol Prog Ser 58: 175 – 189.

Wahl M. 1997. Living attached: Aufwuchs, fouling, epibiosis. In: Thompson M (ed) Fouling organisms of the Indian ocean: Biology and control technology. Oxford and IBH Publishing Company, New Dehli, p. 31 – 83.

Watanabe S, Nagamatsu N, Yokoo K, Kawakami Y. 1969. The augmentation in frictional resistance due to slime. J Kansai Soc Naval Architects 131:45–51.

Water Research Foundation 2011. Assessing Seawater Intake Systems for Desalination Plants, funded by the Water Research Foundation (Foundation), WateReuse Research Foundation (WateReuse), U.S. Bureau of Reclamation (Reclamation), and California Department of Water Resources (DWR). USA.

Weiße S, Heddergott N, Heydt M, Pflasterer D, Maier T. 2012. A quantitative 3d motility analysis of *Trypanosoma brucei* by use of digital in-line holographic microscopy. PLOS ONE. 7:e37296. 1–13.

Weiße S, Heydt M, Maier T, Schulz S, Spatz JP, Grunze M, Haraszti T, Rosehahn A. 2011. Flow conditions in the vicinity of microstructured interfaces studied by holography and implications for the assembly of artificial actin networks. PCCP. 13:13395–13402.

Willey JM, Sherwood LM, Woolverton CJ. 2008. Prescott, Harley, and Klein's microbiology. 7th ed. New York (NY):McGraw-Hill.

Wu AH, Nakanishi K, Cho K, Lamb R. 2013. Diatom attachment inhibition: limiting surface accessibility through air entrapment. Biointerphases. 8:5 1–10.

Xavier KB, Miller ST, Lu W, Kim JH, Rabinowitz J, Pelczer I, Semmelhack MF, Bassler BL. 2007. Phosphorylation and processing of the quorum-sensing molecule autoinducer-2 in enteric bacteria. ACS Chem Biol. 2:128–136.

Yan Y, Dong Y, Yan W. An ecological study of bouy fouling in Chzhan'zsyan Harbor, Redat Haiyang Trop. Oceanol., 13(2), 68, 1994.

Yebra DM, Kiil S, Dam-Johansen K. 2004. Antifouling technology–past, present and future steps toward efficient and environmentally friendly antifouling coatings. Prog Org Coat;50:75–104.

Zhang W, Sileika TS, Chen C, Liu Y, Lee J, Packman AI. 2011. A novel planar flow cell for studies of biofilm heterogeneity and flow-biofilm interactions. Biotechnol Bioeng 108:2571–2582.

Zheng C. 2005. Micro-nanofabrication: Technologies and applications. Higher education press, Springer-Verlag. Beijing.

Zilman G, Novak J, Benayahu Y. 2008. How do larvae attach to a solid in a laminar flow? Marine Biology. 154:1-26.

Index